Depth and Orbital Tuning: a New Chronology of Glaciation and Nonlinear Orbital Climate Change.

by

Peter Huybers

Submitted to the Department of Earth, Atmospheric, and Planetary Sciences
in partial fulfillment of the requirements for the degree of

Master of Science in Climate Physics and Chemistry

at the

MASSACHUSETTS INSTITUTE OF TECHNOLOGY

May 2002

Author .....
Department of Earth, Atmospheric, and Planetary Sciences
May 18, 2002

Certified by .....
Carl Wunsch
Director, Program in Atmospheres, Oceans, and Climate
Thesis Supervisor

Accepted by .....
Ronald Prinn
Head, Department of Earth Atmospheric and Planetary Sciences

Depth and Orbital Tuning: a New Chronology of Glaciation and Nonlinear Orbital Climate Change.

by

Peter Huybers

Submitted to the Department of Earth, Atmospheric, and Planetary Sciences
on May 18, 2002, in partial fulfillment of the
requirements for the degree of
Master of Science in Climate Physics and Chemistry

Abstract

It is suggested that orbital tuning casts a false light upon the chronology of glaciation and the understanding of the climatic response to orbital variations. By developing a new age-model, independent of orbital assumptions, a significant non-linear response to orbital forcing becomes evident in the $\delta^{18}O$ record. The new age-model also indicates glacial terminations two through eight are 8,000 years older than the orbitally based estimates. A simple obliquity threshold model is presented which reproduces the timing, amplitude, and observed non-linearities of the $\delta^{18}O$ record; and supports the plausibility of the new age-model and the inferred non-linear climatic response.

Thesis Supervisor: Carl Wunsch
Title: Director, Program in Atmospheres, Oceans, and Climate

Acknowledgments

I thank Carl Wunsch for being both an advisor and mentor. I also thank Ed Boyle, Bill Curry, Jerry McManus, Delia Oppo, and Maureen Raymo for making much of the data available to me and for invaluable discussion and comments. This work was supported by the National Defense Science and Engineering Graduate Fellowship Program.

Contents

Introduction

Much of the process of inference concerning past climate relies heavily upon the assignment of ages to measurements and events recorded in deep-sea and ice cores. Sediment and ice accumulation are analogous to strip-chart recorders, marking the record of the past climate state in a large variety of physical variables. These records tend to be noisy and blurred by bioturbation and a variety of diffusive processes [e.g. *Pestiaux and Berger*, 1984]. The major difficulty, however, is that these strip-chart recorders run at irregular rates, stretching and squeezing the apparent time scale, and so distorting the signals being sought if depth in the core is taken to be linearly related to time. It is not an exaggeration to say that understanding and removing these age-depth (or 'age-model') errors is one of the most important of all problems facing the paleoclimate community, as the accuracy of such models is crucial to understanding both the nature of climate variability and underlies any serious hope of understanding cause and effect.

Orbital-tuning assumes a constant phase relationship between paleo-climatic measurements and an orbital forcing based on Milankovitch theory [*Milankovitch*, 1941], and is the currently favored method by which Pleistocene age is estimated [e.g. *Imbrie* 1984, *Martinson* 1987, *Bassinot* 1994, and *Kent* 1999]. The presence of eccentricity-like amplitude modulation in the precession band of orbitally-tuned $\delta^{18}O$ records seems to be the clinching argument for orbital-tuning [e.g. *Imbrie*, 1984 and *Shackleton*, 1995]. But contrary to the assertion that orbital-tuning does not affect amplitude modulation [*Paillard*, 2001], the precession parameter is shown to undergo strong frequency modulation during times of low eccentricity, which when narrow-pass-band filtered, produces eccentricity-like amplitude modulation. Since the precession band accounts for only a small part of the total $\delta^{18}O$ variance [*Wunsch*, 2002], the narrow-pass-band filtering is necessary, and orbital tuning assures the presence of eccentricity-like amplitude modulation. This non-verification of orbital age-models is emphasized by showing orbitally-tuned noise meets the criteria [*Bruggerman*, 1992] for an accurately tuned $\delta^{18}O$ record. Tuning is accomplished here by a new objective algorithm termed *XCM* which seeks a maximum cross-correlation between two records. Having shown that post-orbital-tuning analysis of a record cannot verify an age-model, a Monte Carlo test is introduced which instead estimates the expected skill of an orbital-tuning procedure. XCM demonstrates some skill in correcting systematic age-model errors in linear age-depth relationships (e.g. an under-estimated mean

sediment accumulation rate), but no skill in making detailed age-model corrections (e.g. correcting for random fluctuations in accumulation rate).

An alternative to orbital-tuning is to estimate age using mean sediment accumulation rates [*Shaw*, 1964], and is termed *depth-tuning*. The literature has numerous examples of depth-tuning [e.g. *Shackleton and Opdyke* 1972, *Hays* et al 1976, *Williams* 1988, *Martinson* et al 1987, and *Raymo*, 1997], but in each case the authors ultimately deem an orbitally-tuned age-model as more accurate. This uniform preference for orbital age-models reflects a confidence in the Milankovitch theory, but this theory has has recently come under question [e.g. *Winograd* 1992, *Muller and MacDonald* 1997, and *Henderson and Slowey* 2000, *Elkibi* 2001, *Gallup* 2002, and *Wunsch, 2002*]. Compared to previous depth-tuned age-models this study benefits from a significantly greater number of $\delta^{18}O$ records (26 vs. 11 as the previous largest [*Raymo*, 1997]) and an analysis of sediment compaction with a correction for it attendant effects. Relative to orbital age-models, the depth-tuned age-model indicates terminations two through eight are each eight KY older, a conclusion supported by the available radiometric constraints on termination ages [e.g. *Karner and Marra* 1998, *Esat* et al 1999, *Henderson and Slowey* 2000, and *Gallup* 2002]. The development of a stochastic sediment accumulation model allows for a Monte Carlo test of the depth-tuning procedure and provides uncertainty estimates for the depth-tuned age-model. The depth-tuned age-model has an average estimated uncertainty of 8.5KY for any individual date and it is unlikely that the systematic offset between orbital and depth-tuned ages is a result of sediment accumulation rate variations. Also, an empirical orthogonal functions (EOF) analysis of accumulation rates demonstrates basin-wide spatial patterns which are themselves of climatic significance.

Spectral analysis of the $\delta^{18}O$ record, using the new depth-tuned age-model, indicates that significant energy is concentrated at

$$f(n) = \frac{1}{41} + \frac{n}{100} \qquad n = \{-2, -1, 0, 1\}$$

and at the 1/100KY frequency band where 1/41KY represents the obliquity band. For the leading EOF of the 26 $\delta^{18}O$ record, each spectral peak at $f(n)$ is above of the 95% confidence level and together they account for more than 60% of the total variance. These same frequency bands display significant auto-bicoherency which strongly indicates a non-linear coupling between the 1/41KY obliquity variations and the quasi-1/100KY oscillation. A Monte Carlo spectral simulation indicates only 23% of $\delta^{18}O$ variance is linearly attributable to obliquity and precession and, by inference,

the majority of the orbital response is non-linear. The new depth-tuned age-model is also used to re-estimate parameters for *Imbrie and Imbrie*'s [1980] ice-volume. The re-tuned ice-volume model indicates the presence of stronger obliquity forcing and a more rapid glacial melt response, and while the model reproduces the depth-tuned timing of glaciations, the amplitudes are incorrect.

The apparent non-linear coupling between obliquity and the 1/100KY cycle motivates the construction of a simple obliquity based threshold model of glaciation. The model has three adjustable parameters which set the accumulation rate, melt rate, and initial ice volume; it also successfully reproduces the depth-tuned timing of terminations, approximate amplitude of each termination, spectral peaks at $f(n)$ and 1/100KY, and the observed auto-bicoherence pattern. Relative to other simple climate models, this model achieves a high squared cross-correlation (0.63) with the $\delta^{18}O$ observations using few adjustable parameters. The fidelity with which this model reproduces the salient features of the $\delta^{18}O$ observations supports both the plausibility of the depth-tuned age-model and the inferences of non-linear climatic behavior.

Chapter 1

Orbitally-tuned Age-models

1.1 Simple Model of Sediment Accumulation

Orbital-tuning refers to the process of assigning an age to a record based on an assumed relationship with the earth's orbital variations. In marine sediment cores where records are initially measured against depth, orbital-tuning is, in effect, estimating sediment accumulation rates[1]. Beginning with the supposition that sediment accumulation is stochastic, the age-depth relationship can be modeled as a random walk process. Let d_t be the accumulated sediment (the "depth") in a core at time t. t is to be regarded as a discrete variable. Then per unit time, $\triangle t$, d_t increases at the mean sediment accumulation rate ($\bar{S}$) plus an anomaly (S'),

$$d_{t+1} = d_t + \triangle t\bar{S} + \triangle tS'_t.$$

Dividing by $\bar{S}$ converts the depth increment to a true time increment plus an anomaly,

$$t'_{n+1} = t'_n + \triangle t + \triangle t\frac{S'_t}{\bar{S}}. \tag{1.1}$$

If S' is a stochastic variable of zero mean, and variance σ^2, then Eq. (1.1) represents a random walk in the time variable. The simplest such model is one of uncorrelated increments, $< S'_t S'_{t'} >= 0$, $t \neq t'$. (We use the brackets, $< \cdot >$ to denote expected value.) Then, the variance of the difference between the apparent and true time grows linearly on average [Feller, 1966],

[1]Post-deposition processes and core recovery effects are considered in more detail later in this work

$$< (t'_n - n\triangle t)^2 >= n\triangle t \frac{\sigma^2}{\bar{S}^2}$$

Following *Moore and Thomson* (1991) and *Wunsch* (2000), we term the rate of growth the *jitter*,

$$J = \frac{\sigma^2}{\bar{S}^2} \tag{1.2}$$

By permitting S' to take on more interesting temporal covariances, one can generate very complex behavior in the statistics of t_n, but in the interests of simplicity, the discussion is initially confined to this basic case. The purpose of the paper is to investigate how to best infer t from measurements in t' and then to apply the results to the observed $\delta^{18}O$ record.

1.2 Orbital Parameters and Modulation

Following the demonstration by Hays et al. (1976) of the apparent presence of Milankovitch band spectral features in deep-sea cores, the plausible assumption has been made that such features are present in most climate records. Along with certain further simple assumptions, such as that of a fixed phase response to Milankovitch forcing throughout the core duration, tuning the records so as to sharpen and enhance the Milankovitch frequency bands has become the favored method to recover $t\,(t')$. We thus begin by reviewing some of the basic structure of the Milankovitch forcing.

The eccentricity, obliquity, and precessional earth orbital parameters along with the solar constant and the mean earth-sun distance are sufficient to calculate the solar radiation incident at the top of the earth's atmosphere for any given time and place. Apart from some weak secular terms, this insolation can be well approximated by a finite number of interacting periodic terms [e.g. *Berger and Loutre*, 1991]. These interactions involve only products of sinusoids, and we pause to recall the basic elements of amplitude (AM) and frequency modulation (FM).

1.2.1 Amplitude and Frequency Modulation

Consider a pure cosine, $\cos(2\pi t f_1)$, of "carrier "frequency f_1 multiplied by another cosine of frequency f_2. Then,

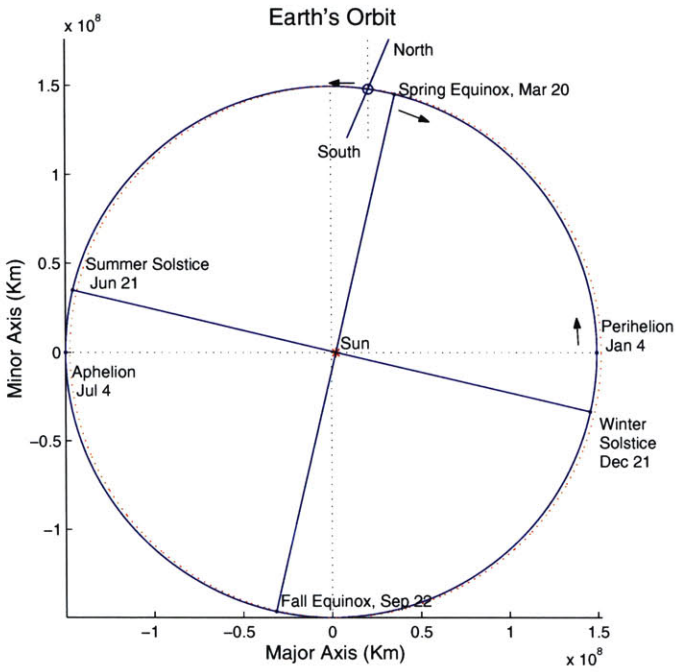

Figure 1-1: The current orbital configuration of the earth viewed looking downward on the North Pole. The solid line is earth's slightly eccentric orbital path (to scale), and the dotted line is a circle centered on the sun. Note that the earth is furthest from the sun during northern hemisphere summer. The earth and elliptic axis are both moving counter-clockwise, while the equinoxes and solstices are moving clockwise.

$$\mu(t) = \cos(2\pi t f_1)\cos(2\pi t f_2) = \cos(2\pi t(f_1 + f_2)) + \cos(2\pi t(f_1 - f_2)) \tag{1.3}$$

here the carrier frequency, f_1, is split into two new frequencies, $f_1 \pm f_2$, in the process known as amplitude modulation. A power spectrum of $p\,(t)$ would display peaks not at f_1, but at $(f_1 \pm f_2)$, that is, with two-sidebands.

If instead a cosine is "frequency modulated" by another cosine we have.

$$\begin{aligned}\mu(t) &= \cos(2\pi t f_1 + 2\pi\delta\cos(2\pi t f_2)) \\ &= \cos(2\pi t f_1)\cos(2\pi\delta\cos(2\pi t f_2)) + \sin(2\pi t f_1)\sin(2\pi\delta\cos(2\pi t f_2)).\end{aligned} \tag{1.4}$$

Using a simple identity [*Olver* 1962, Eqs 9.1.44-45] Eq. (1.4) is,

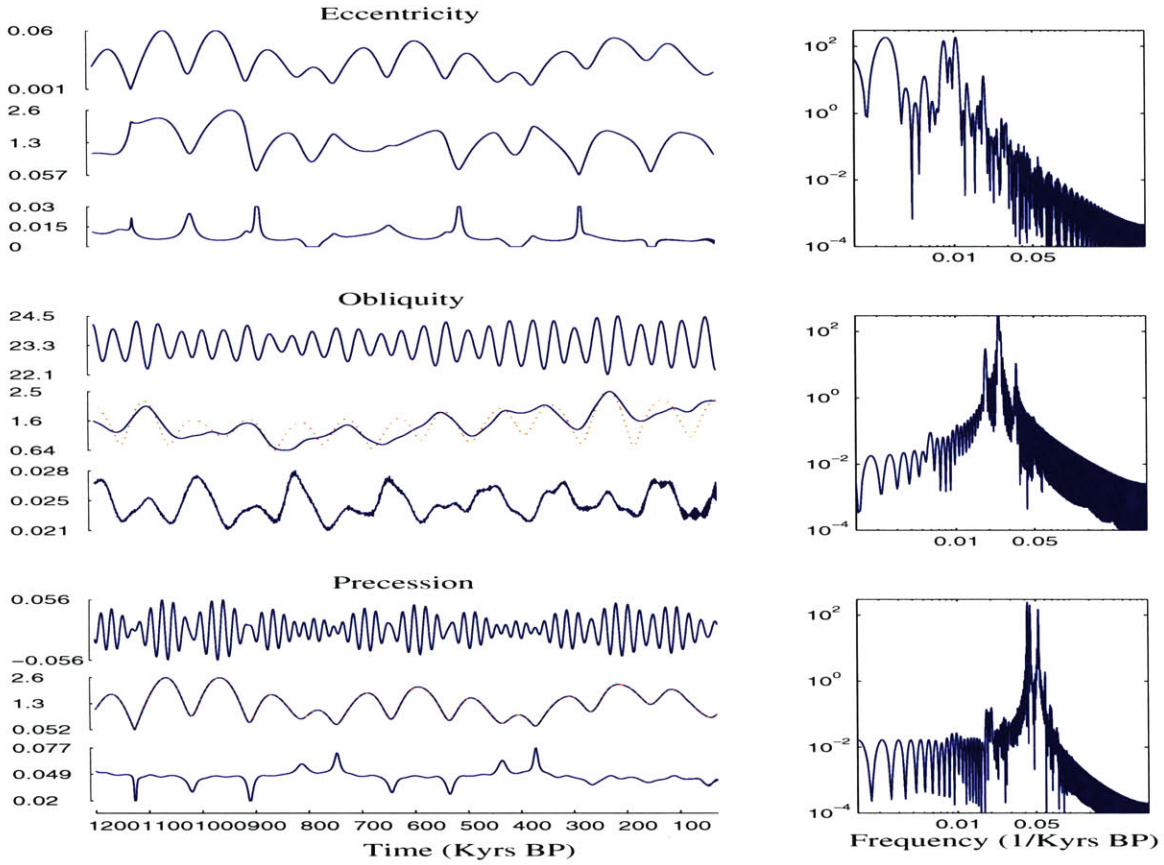

Figure 1-2: Each orbital parameter is shown along with its amplitude modulation (middle), frequency modulation (bottom), and power density spectrum (right). For obliquity the orbital inclination is plotted along with the AM (dotted middle). By definition the AM of the precession parameter is eccentricity. Note in the power density spectrums that each parameter is largely confined to a unique frequency band.

$$\begin{aligned}\mu(t) &= cos(2\pi t f_1)[J_o(2\pi\delta f_2) + 2\sum_{k=1}^{\infty} J_{2k}(2\pi\delta f_2)\cos(4\pi k t f_2)] \\ &\quad - \sin(2\pi t f_1)\sum_{k=0}^{\infty} -1^k J_{2k+1}(2\pi\delta f_1)\cos(2\pi(2k+1)t f_2) \qquad (1.5)\end{aligned}$$

where the J_p are Bessel functions. Now $m(t)$ has spectral peaks at $f_1 \pm nf_2$ for $n = [0, 1, 2...]$ with the relative amplitudes determined by the strength of the modulation term and the displacement from the carrier frequency. These modulation effects are apparent in the earth's orbital parameters.

1.2.2 Eccentricity

A diagram of earth's present orbital configuration is shown in Figure 1-1. The solid ellipse shows earth's current slightly eccentric orbit to scale, while the dashed line is a circle centered on the sun. Eccentricity is measured as

$$e = \sqrt{1 - \left(\frac{L_{\text{major}}}{L_{\text{minor}}}\right)^2} \tag{1.6}$$

where L represents the length of the major and minor orbital axis. Currently the eccentricity of the earth is .01672. This produces a 7% annual change in the insolation incident at the top of the atmosphere from 354 (aphelion) to $331\frac{Watts}{m^2}$ (perihelion). This difference is primarily due to the sun's displacement from the geometric center of the earth's orbit to one of the two foci of the orbital ellipse. Eccentricity is unique among the orbital parameters in that it affects the total insolation incident on the earth rather than only redistributing it.

Figure 1-2 shows the frequency modulation and amplitude modulation of each orbital parameter [see *Berger and Loutre*, 1991] along with its power density spectrum. Eccentricity, e, displays rapid transitions in frequency and amplitude at its local minima. While e is dominated by a few low-frequency terms, it also has a significant broadband component. Note however, that on these timescales, the orbital parameters are deterministic, and the frequency domain behavior of e is not that or red-noise process. This stochastic (broadband spectrum) behavior has to be included in any discussion of the effects of eccentricity on climate.

1.2.3 Obliquity

Obliquity measures the angle between earth's equatorial and orbital planes and is currently 23.5^o. The earth's equatorial plane precesses with a period of 25.8KY and the earth's orbital plane precesses with a period of 70KY. Obliquity measures the difference between these two planes which results in a primary insolation frequency of $1/25.8 - 1/70 = 1/41$KY [see *Muller and MacDonald*, 2000]. Apart from the 7% change in insolation due to eccentricity and timed by precession, obliquity accounts for the magnitude of the seasonal insolation variations.

Obliquity AM (ranging from 2.4^o to 0.7^o) is primarily caused by variations in the inclination of the orbital plane which, measured relative to the invariant plane [2],

[2]The invariant plane is the plane perpendicular to the total angular momentum vector of the

has a red noise spectrum dominated by a 1/100KY peak. *Muller and MacDonald*, [1997] have proposed that the periodic alignment of the earth's orbital plane with a galactic plane of dust could provide a physical link to the quasi-100KY glacial oscillation. Obliquity FM has a red noise spectrum dominated by two peaks at 1/170 and 1/100KY [see *Liu and Chao*, 1998]. *Liu* [1998] propose that variations in the time integrated insolation forcing due to FM accounts for the 100KY glacial oscillation. The result of these AM and FM modulations on the spectrum of obliquity is evident in the minor side-lobes flanking the central 1/41KY peak.

1.2.4 Precession

The earth precesses because of the torque exerted on its equatorial bulge by the moon and sun. This precession is nearly periodic at 25.8KY. In Milankovitch theory, however, one is interested in the climatic effect of precession which is to shift the phase of the longitude of perihelion relative to the seasonal cycle. Measuring the degree of alignment of the line of apsides with the spring equinox, and scaling by the degree of eccentricity provides a measure of the precessional influence on seasonal insolation changes. The climatic precession parameter is accordingly defined as

$$p(t) = e(t)\sin(w(t))$$

where $e(t)$ is the eccentricity, and $w(t)$ is the angle between perihelion and the spring equinox. Climatic precession does not affect yearly mean insolation, and a model with seasonal sensitivity to insolation forcing is necessary to elicit a precessional response [see *Rubincam*, 1994]. Precession is elicited in Milankovitch theory by relating the glacial configuration to northern hemisphere summer insolation.

Over the last 800KY the mean frequency of the precession parameter, $d\bar{w}/dt$, has been 1/20.4KY with lows in instantaneous frequency reaching 1/50KY and highs of 1/13KY. These dramatic excursions from the mean frequency are due to rapid changes in the longitude of perihelion which can be understood by considering a perturbation, $F = R\hat{r} + N\hat{h} + T\hat{h} \times \hat{r}$, applied impulsively to the earth. The relevant vector components of F are $\hat{r}$ pointing from the sun to the earth and $\hat{h}$ perpendicular to the orbital plane, and the resultant change in the longitude of perihelion is [e.g.

---

planets.

Danby, Eq. 11.5.11, 1992]

$$dw = \frac{\sqrt{1-e^2}}{nae}\left\{-Rdt\cos v + Tdt\sin v\frac{2+e\cos v}{1+e\cos v}\right\} \tag{1.7}$$

where n is earth's average orbital angular velocity, v is the angle between perihelion and the earth, and a is earth's mean distance from the sun. The equation is valid over at least the last 5Ma as eccentricity is always greater than zero. Only those components of the impulse in the orbital plane (R and T) act to change w. Clearly the longitude of perihelion is more susceptible to perturbations when e is small and, accordingly, Figure 1-2 shows the largest excursion in dw/dt, or frequency, when eccentricity is near zero. These large variations in the frequency of precession are important for understanding why precessional amplitude modulation does not indicate an accurately orbitally-tuned age-model. Major causes of these perturbations to earth's orbit are Jupiter since it is massive, and Venus because it is close [*Muller and MacDonald*, 2000]. The time average mean of dw/dt over the last 800KY is 1/25.8-1/20.4=1/98KY, where perihelion tends to move in the opposite direction of the spring equinox.

Figure 1-3 shows the time series and power density spectra of the non-AM signal, $p(t)/e(t)$, and that the characteristic triplet of precessional peaks is generated by FM alone. From Eq 1.3, one expects multiplication by $e(t)$ to result in a splitting of the triplet of precessional carrier frequencies into a multitude of side-lobes. A peculiar relationship between the AM and FM of precession, however, suppresses these side-lobes as evidenced in the PSD of $p(t)$. To gain insight into this filtering effect note that the triplet of eccentricity frequencies equals the differences of the triplet of precessional frequencies.

$$\begin{aligned}
f_{p1} &= \tfrac{1}{23.7} \\
f_{p2} &= \tfrac{1}{22.4} \\
f_{p3} &= \tfrac{1}{19.0} \\
f_{e1} &= \tfrac{1}{404} &&= f_{p2} - f_{p1} \\
f_{e2} &= \tfrac{1}{124} &&= f_{p3} - f_{p2} \\
f_{e3} &= \tfrac{1}{98.7} &&= f_{p3} - f_{p1}
\end{aligned}$$

where the subscripts p and e refer to the precessional and eccentricity frequencies. Considering only the dominant triplets, the precession parameter may be written as

$$p(t) \sim [\sin(2\pi t(f_{p2} - f_{p1}) + \phi_{e1}) + \sin(2\pi t(f_{p2} - f_{p1}) + \phi_{e2}) + \sin(2\pi t(f_{p2} - f_{p1}) + \phi_{e3})] \times [\sin(2\pi t f_{p1} + \phi_{p1}) + \sin(2\pi t f_{p2} + \phi_{p2}) + \sin(2\pi t f_{p3} + \phi_{p3})] \quad (1.8)$$

The ensuing sum and difference frequencies from these multiple AM relationships produce side-lobes coincident with the original precessional triplet of frequencies. For example $f_{p1} \pm (f_{p2} - f_{p1})$ produces side-lobes at f_{p2} and $f_{p2} - 2f_{p1}$. Evidently the frequency and amplitude modulation are arranged to cancel one another out, and this effect is observed regardless of which period between zero and five Ma BP is chosen. The suppression of energy outside of the main triplet of precessional frequencies is tantamount to narrow band-pass filtering. Indeed, when comparing the PSD of $p(t)$ with a boxcar pass-band filtered version of $p(t)/e(t)$ (bottom of Figure 1-3) it appears the interaction of the FM and AM better suppress the energy outside of the precessional triplet than the boxcar filter itself. It is not surprising, then, that a narrow band-passed precession-like FM signal exhibits amplitude modulation similar to eccentricity.

An alternative description of the generation of precession-like AM is that, as indicated by Eq 1.7, during minima in eccentricity there are large excursions in precessional frequency. Pass-band filtering diminishes the energy at these excursional frequencies, which translates into a decreased amplitude during periods of low eccentricity. As such, any pass-band filter can generate a precession like AM signal from a precession-like FM signal. In the next section it is shown that orbital-tuning can transform noise into a precession-like FM signal, and after pass-band filtering over the precessional triplet, the tuned noise displays precession-like AM.

1.3 Orbitally-Tuned Noise

The last section described insolation as a frequency and amplitude modulated set of carriers. If climate linearly responds to insolation variations, one would expect the modulation structure of the forcing to be at least qualitatively mimicked in the response. A multitude of methods have been used to orbitally-tune paleo-climatic records to the assumed linear insolation response. The criteria used to assess the accuracy of an orbitally-tuned timescale are outlined by *Imbrie et al* [1984] , *Bruggerman* [1992] , and *Shackleton et al* [1995]. Generally these criteria are that geochronological data should be respected within their estimated accuracies, sedimentation rates

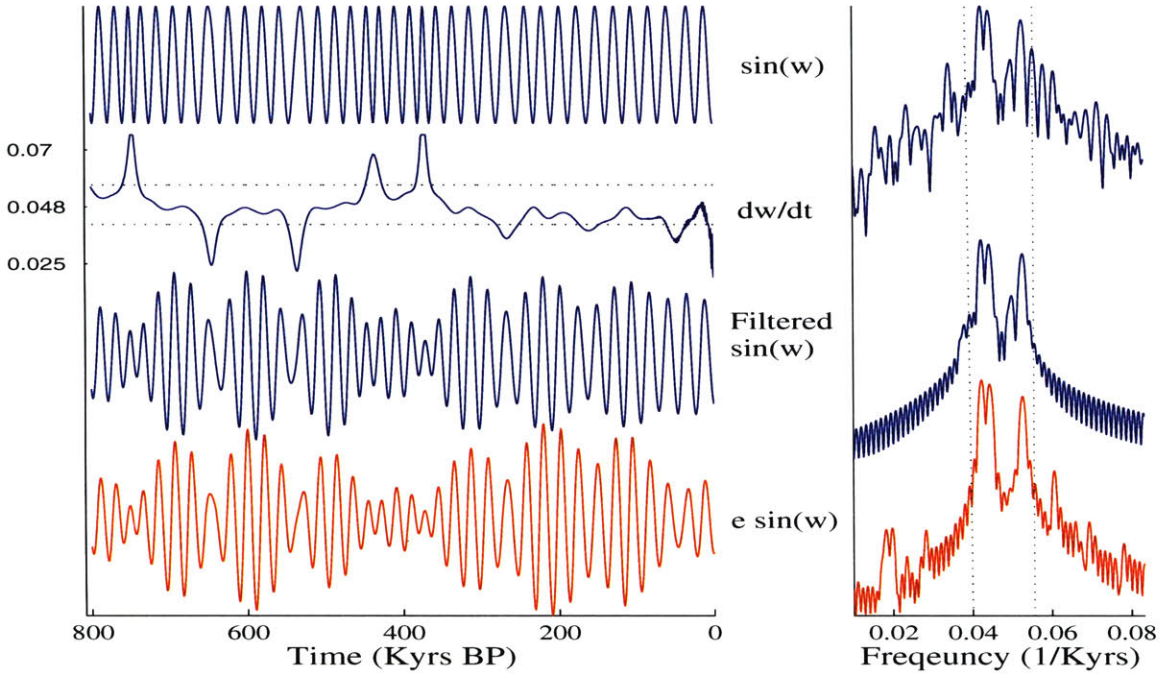

Figure 1-3: The precession parameter divided by eccentricity and its associated PSD, (top $\sin w$). The instantaneous frequency estimate (dw/dt in 1/KY) is shown along with the cut-off frequencies of a pass-band filter (horizontal dotted black lines and vertical in the PSD). Applying this pass-band filter results in an amplitude modulated signal (Filtered $\sin w$) which is very similar to the precession parameter ($e \sin w$). Note that large frequency excursions in w occur when eccentricity is small, and extend beyond the cut-off frequencies. The AM of the filtered FM signal, then, corresponds to the eccentricity AM precession parameter. Also note that the side-bands in the PSD of $e \sin w$ drop off more quickly than the filtered signal itself; eccentricity is effectively pass-band filtering $\sin w$.

remain plausible, variance should become concentrated at the Milankovitch frequencies with a high coherency between the orbital signal and the data, and what seems to be the clinching argument, similar amplitude modulation should appear in the Milankovitch-derived insolation and in the tuned result. *Imbrie* et al [1984] asserted that the "statistical evidence of a close relationship between the time-varying amplitudes of orbital forcing and the time-varying amplitudes of the isotopic response implies that orbital variations are the main external cause of the succession of late Pleistocene ice ages." More recently *Shackleton et al* [1995] concludes, "Probably the most important feature through which the orbital imprint may be unambiguously recognized in ancient geological records is the amplitude modulation of the preces-

sion component by the varying eccentricity of the Earth orbit." These assertions take on the air of accepted truths as *Paillard* [2001] states in comparing a band-passed SPECMAP record with precession, "It is remarkable that both time series have a quite similar modulation of their amplitude. This is probably one of the strongest arguments in favor of a simple causal relationship between the precessional forcing and the climatic response in this frequency band. Indeed, in contrast to other techniques, amplitude modulation is not affected by tuning."This section examines the degree to which apparent consistency of amplitude modulation can in fact be assumed to demonstrate accuracy in a tuned age-model.

Tuning of core data against insolation curves has been done in a number of different ways, ranging from subjective methods [*Imbrie* et al, 1984] to more objective methods [*Martinson* et al, 1987]. Here, a simple and repeatable algorithm is used for objective tuning, but which is readily demonstrated to transform a pure noise process into one with an apparent orbitally dominated signal. In common with most such methods [e.g. *Martinson*, 1982 and *Bruggerman*, 1992], the algorithm can be used to enhance the orbital features of a record. The procedure used here is to maximize the cross-correlation between two records and is termed XCM (cross-correlation maximizer) [3]. XCM begins with a noise process, to be defined-below, $\eta(t')$, and an orbitally-based target record, $\tau(t)$. For convenience, both are assumed to have zero time–mean. A spurious assumption is made that adjustments to t' which increase the cross-correlation between $\eta(t')$ and $\tau(t)$ indicates an improved age-model. The adjustments to t' take the form of a time adjustment function, μ, such that ideally $t' + \mu(t') = t$. At the end of the optimization, r^2 typically increases from near zero to about 0.25. See Appendix A for a detailed explanation of the XCM routine.

1.3.1 White Noise

A typical realization of XCM tuning is presented in Figure 1-4. Pure white noise, $\eta(t')$, is tuned to the precession parameter [*Berger and Loutre*, 1992], $\tau(t) = p$, over a 800KY period. Consistent with the results of *Neeman* [1993], a squared cross-correlation of 0.19 is achieved, a concentration of variance at the triplet of precessional peaks occurs, a coherency in the precession band of greater than 0.9 is achieved (0.65 is the approximate 95% level of no significance), and both AM and FM similar to the precession

[3]This algorithm (written for MATLAB) is available at http//web.mit.edu/phuybers.

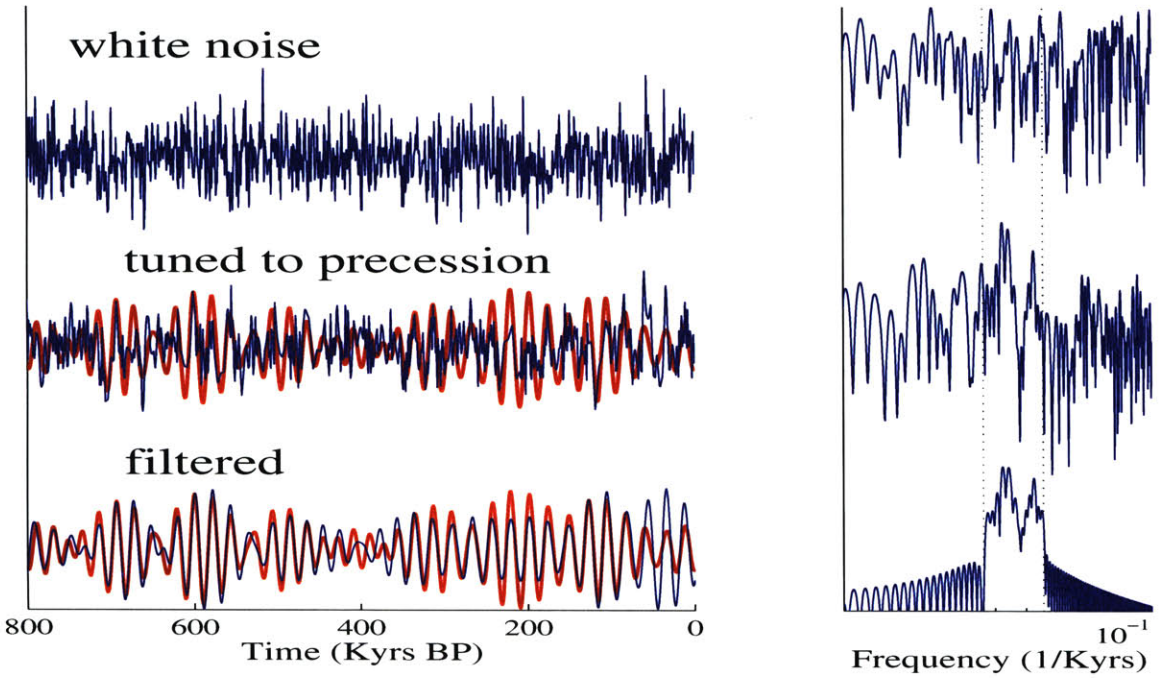

Figure 1-4: By tuning white noise to the precession parameter, the squared cross-correlation was increased from zero to 0.19. On the left are time series of (top) white noise, (middle) white noise tuned to precession (thin) and superimposed on the precession parameter (thick), and (bottom) tuned noise pass-band filtered over the precession band (thin) and again superimposed on the precession parameter (thick). The right shows the power density spectra (PSD) associated with each modification of the noise.

parameter has appeared—completely spuriously. This result should not be a surprise; attempts to maximize the correlation between two records necessarily requires the amplitudes of variations to be brought into alignment, and imposes common frequency modulations. The combination of these imposed amplitude and frequency modulations, when pass band filtered, produces a visual amplitude modulation in the two series.

In the tuning done in this paper the sediment accumulation rates are constrained to remain within plausible levels of variation by requiring a record to never be squeezed or stretched by more than a factor of five. Considering the difficulty of determining geochronological dates in the interval between termination two (approximately $130KYBP$) and the Brunhes-Matuyama (B-M) boundary (approximately $780KYBP$), it seems unlikely the available geochronological constraints would conflict with this tuned age-model.

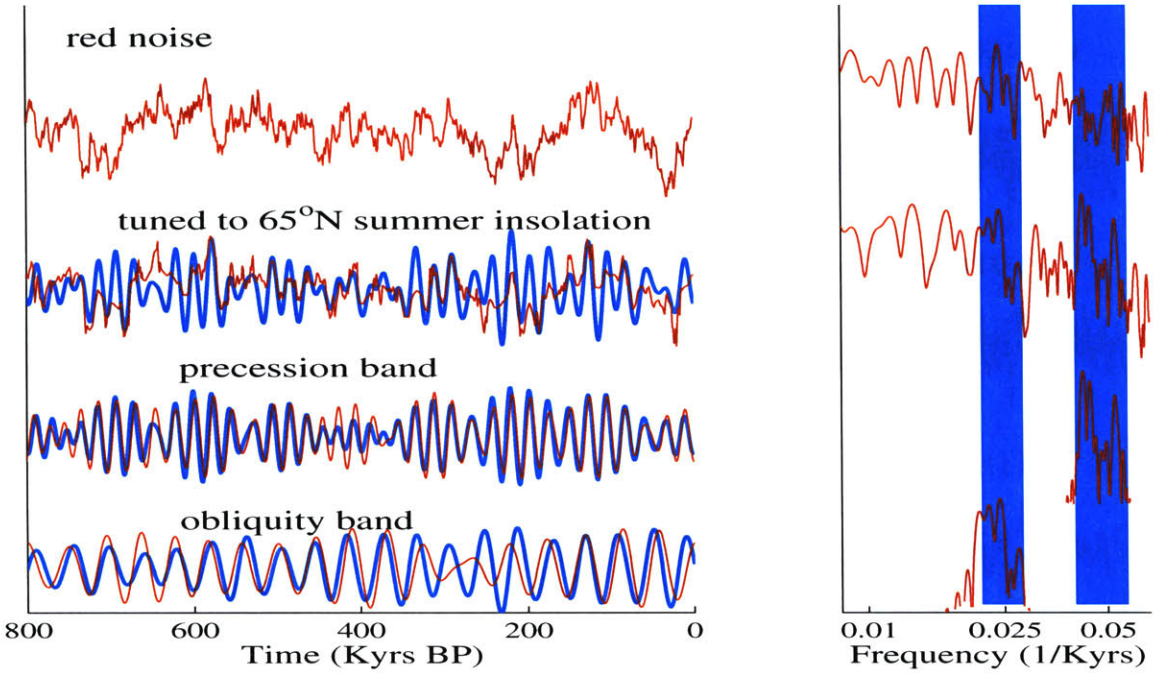

Figure 1-5: Red noise orbitally-tuned to summer insolation at 65^o North. In this case the squared cross-correlation was increased from zero to 0.31. The band-passed filtered record is shown for the precessional and obliquity bands superimposed on the respective orbital parameters. The associated PSD are shown to the right.

1.3.2 Red Noise

Figure 1-5 shows a second tuning realization where a $\eta(t')$ of red noise is tuned to a $T(t)$ of insolation at 65 North on July 15th [*Berger and Loutre*, 1992]. $\eta(t')$ is characterized by a power density spectrum,

$$\Phi(f) = \frac{1}{f^2 + \frac{1}{100^2}}$$

$\Phi(f)$ has a -2 power law relationship giving way to white noise at frequencies below 1/100KY. This spectral relationship approximates the background continuum observed in the $\delta^{18}O$ [see Section 2.3.1][4]. The variance in $T(t)$ is composed of 13% obliquity, 84% precession, and because the insolation is calculated for a fixed date, only .02% eccentricity. Orbital-tuning increases the squared cross-correlation from zero to 0.31. Again high coherencies and a concentration of variance are observed at

[4]For a discussion of the significance of power law relationships to the $\delta^{18}O$ record see *Shackleton and Imbrie* [1990].

the orbital frequencies. This indicates that regardless of the true nature of the $\delta^{18}O$ record, orbital-tuning will generate an orbital-like behavior.

1.4 Monte Carlo Test of Orbital-Tuning

This section seeks to statistically characterize the capacity of tuning to increase the accuracy of an age-model when an orbital signal is present. The method adopted is to generate a synthetic record composed of an orbital-like signal and noise, jitter the age-model of the record (this process is fully explained in Chapter 2), orbitally tune the jittered record to the original orbital-like signal, and assess the accuracy of the new age-model. While many orbitally-tuned records are reported with uncertainties, these seem to be based on subjective judgments [e.g. *Imbrie* et al, 1984]. The method presented here provides a more objective basis by which to estimate age-model accuracy.

The root mean square (rms) deviation of the age-model from the true-age is used to measure the accuracy,

$$\sigma_{rms}(m) = \left(\frac{1}{N} \sum_{i=0}^{N} (t_i - m)^2 \right)^{\frac{1}{2}}$$

where N is the number of data points, t_i is the true age of the $i-th$ data point, and m is the modeled age. Successful tuning is defined as,

$$\frac{\sigma_{rms}(t' + \mu(t'))}{\sigma_{rms}(t')} < 1, \tag{1.9}$$

that is, the rms deviation of the tuned age-model $(t' + \mu(t'))$ from true time is less than the un-tuned age-model t'. The algorithm introduced in the preceding section is used to make a piecewise estimate of $\mu(t')$. Increasing squared cross-correlation from Eq A apparently satisfies the outlined spectral criteria for a successful tuning. This exercise is an attempt to see to what extent and under what conditions increasing cross-correlation indicates a more accurate age-model, i.e.

$$r^2 \sim \frac{1}{\sigma_r ms(t' + \mu(t'))}$$

1.4.1 Number of Adjustable Age Control Points

Define an age control point (ACP) as a depth (d_k) whose associated age can be adjusted backward and forward in time $(t_k = t'_k + \mu_k(t'))$. An ACP represents a

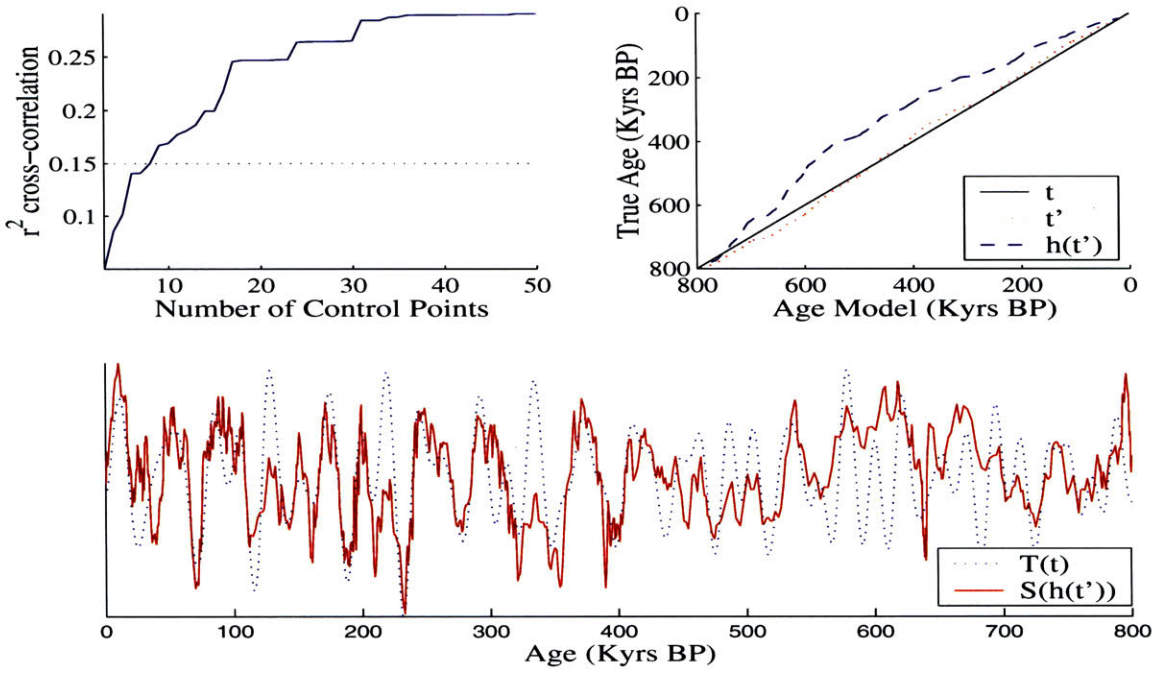

Figure 1-6: $\psi(t')$ is correlated to $\tau(t)$ with an increasing number of age control points (ACPs) to generate a piecewise approximation of $\mu(t')$. In truth the squared cross-correlation between $\psi(t)$ and $\tau(t)$) is 0.15, but with more than 10 degrees of freedom in the age-model the records become over-correlated (top left). The tuned signal with 30 ACPs, $\psi(t' + \mu(t')_{30})$, and the target record, $\tau(t)$, are shown at the bottom. Note that while the tuned age-model yields a strong correlation, it is in fact significantly wrong.

degree of freedom in the age-model, but since sediment accumulation is assumed to be a monotonic process, ACPs are constrained to never reverse order. Between ACPs, time is linearly interpolated with depth; thus ACPs are points in time where the slope of $(\mu(t'))$ may change. In order to recover the true time from a jittered record, assuming accumulation rates vary at all timescales, it would be necessary to assign an ACP to every measurement. But such a large number of degrees freedom coupled with the presence of noise, makes it likely that spurious features would then be correlated. Figure 1-6 shows a signal

$$\psi(t) = \sqrt{.85}\eta(t) + \sqrt{.15}(\theta(t) + p(t))$$

comprised of red noise $\eta(t)$, obliquity $\theta(t)$, and precession $p(t)$. $\psi(t)$ is jittered to $\psi(t')$ and correlated to $\tau(t) = \theta(t) + p(t)$ with three to 50 ACPs using XCM. The true squared cross-correlation is 0.15, but with greater than ten ACPs the signal becomes

over-correlated. In this case, the age-model algorithm converges on an age-model $t' + \mu(t')$ that is worse than the original linear age-depth estimate, t'.

Because the jittered signal is aliased over the entire frequency range, the signal-to-noise ratio cannot be reliably increased. The tendency for tuning to correlate noise can be mitigated by reducing the degrees of freedom available to the age transfer function, $\mu(t')$, and thus a small number of ACPs are used in the following examples. $\mu(t')$ represents a a linear piecewise adjustment to t'. It should be noted that since bioturbational effects, phase lags, and non-linear responses are excluded, these examples discuss tuning under ideal circumstances.

1.4.2 Brunhes-Matuyama Age

One of the well-known successes of orbital-tuning was *Johnson*'s [1982] and later *Shackleton's* [1990] prediction of the revised radiometric date of the Brunhes-Matuyama magnetic reversal (B-M). To test XCM's ability to to detect a mistiming of the Brunhes-Matuyama magnetic reversal (B-M) an orbital-like signal is generated,

$$\psi(t) = \sqrt{1-v}\,\eta(t) + \sqrt{\frac{v}{2}}\theta(t) + \sqrt{\frac{v}{2}}p(t)$$

where $\eta(t)$ is red noise obeying the power law relationship of Eq 2.2, θ is obliquity, and p is the precession parameter; each of which are normalized to zero-mean and unit variance processes. The quantity v represents the percent orbital variance, and the signal-to-noise ratio can be expressed as $\frac{v}{1-v}$. The age-model is then subjected to a jitter and compressed by a factor $t'_2 = at'$, $a = 710/780$, which mimics assigning a date of 710KY BP to the B-M rather than the currently accepted date of 780KY BP [see *Shackleton* et al , 1990 and *Tauxe* et al 1996]. In the absence of jitter, this shrinking of true time distorts the Fourier transform in a way derivable from the "scaling theorem", [Bracewell, 2000] such that frequency w maps into frequency $w' = w/a$. The obliquity peak is shifted from a frequency of $w = 1/41$KY to $w' = 1/37$KY. For tuning purposes, $t' = t = 0$ is fixed correctly at the present true time origin, and a single ACP is assigned at the incorrect date of t' =710KY BP. The issue is whether tuning can produce the correct adjustment slope, $\mu(t') = (780/710)\,t'$.

Realizations of $\psi(t')$ are generated over the grid defined by $J = [0.025, 0.05...0.5]$ and $v = [0.01, 0.02, ...1]$ and tuned to $\tau(t)$ using XCM. Orbital-tuning results which put the B-M more than 100KY away from 710KY BP are discarded as being inconsistent with geological data. The cross-correlation between $\psi(t')$ and $\tau(t)$ is initially

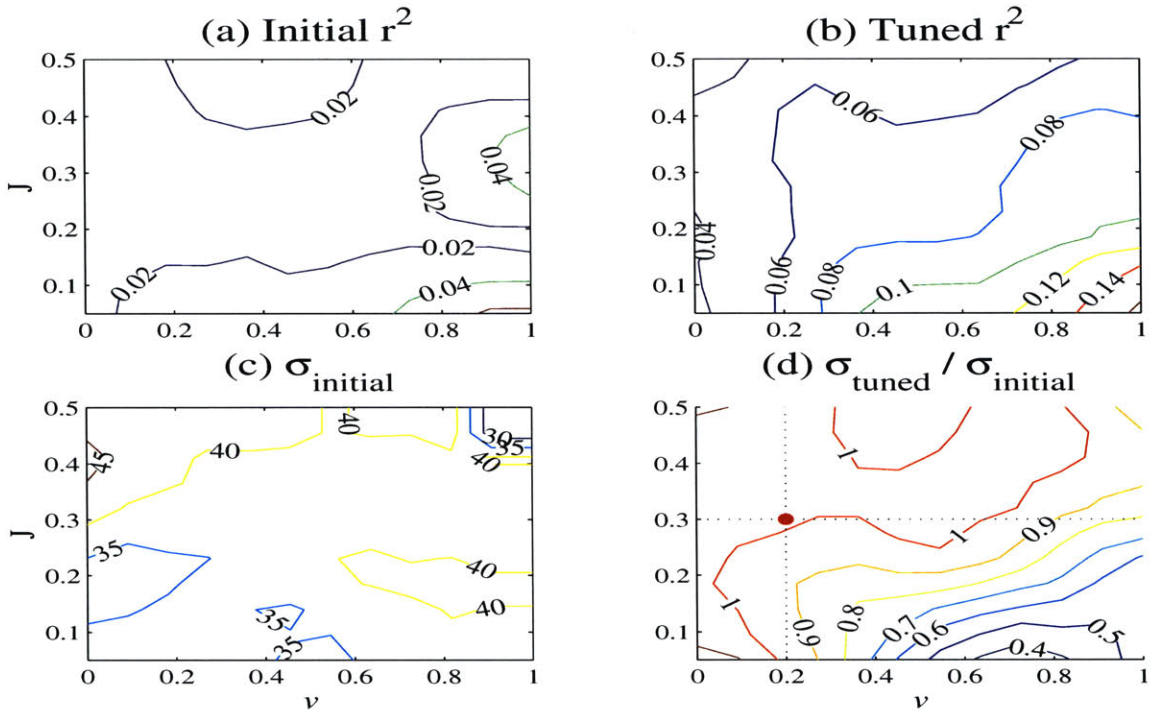

Figure 1-7: Orbitally-tuning the Brunhes Matuyama Magnetic Reversal Date. The contour plots are given as: (a) The initial squared cross-correlation between the jittered signal, $\psi(t')$, and the target curve, $\tau(t)$. (b) The tuned squared cross-correlation value. (c) The initial root mean square age-model error, σ_{rms}. (d) The ratio of initial to final rms age error, $\sigma(t' + \mu(t'))_{rms}/\sigma(t')_{rms}$. The y-ordinate indicates the degree of jitter, J, and the x-ordinate gives the percent orbital variance, v. The red dot indicates the best estimate of the orbital variance and jitter typical of ocean sediment core $\delta^{18}O$ records.

near zero everywhere and the initial rms age error is on the order of 40KY (ref Figure 1-7a and c). Since only one ACP is permitted, tuning with XCM increases the squared cross-correlation by only 0.04 to 0.1. In regions with J less than 0.3 and v greater than 0.1 the tuning decreased the rms deviation from true age (i.e. an at least partially correct adjustment slope) and the tuning is considered skillful (ref Eq 1.9). In chapter two the degree of jitter for $\delta^{18}O$ records is estimated as 0.3 and in chapter three the fraction of $\delta^{18}O$ variance linearly related to obliquity and precession is estimated as 0.2. This puts the $\delta^{18}O$ record just outside the region where tuning shows skill. A $\delta^{18}O$ record with either slightly lower J or higher v could well lie within a region of greater skill, and there are indications ODP677 is such a record [see *Shackleton* et al, 1990]. The skill of XCM in tuning synthetic signals is thus consistent

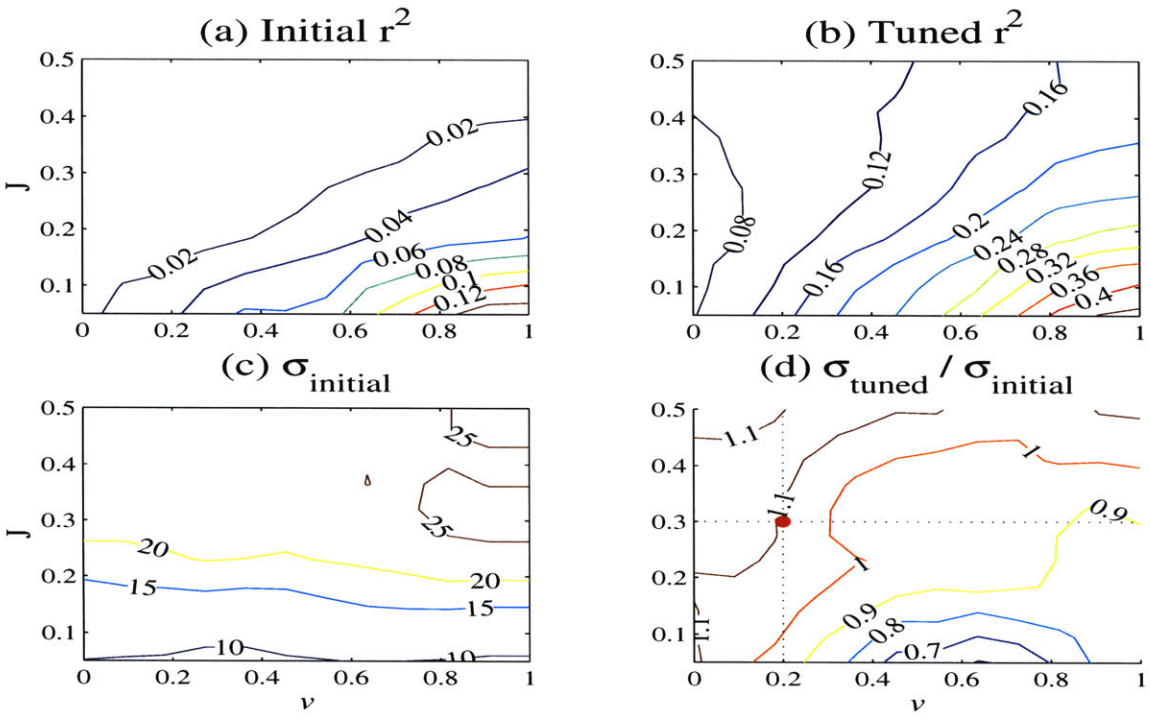

Figure 1-8: Same as Figure 1-7, but ACPs are located at 270 and 530KY BP, and the final age is anchored at 800KY BP. The dot indicates the estimated orbital variance and degree of jitter of the $\delta^{18}O$ records.

with *Johnson*'s [1982] and *Shackleton*'s [1990] prediction of a more accurate B-M age based on the results of orbital-tuning.

1.4.3 Detailed Age-model Corrections

The second set of examples fixes the start and end times of $\psi(t')$ to the true times of 0 and 800KY BP. Two ACPs are introduced at 270 and 530KY BP allowing for three linear segments in approximating $\mu(t')$. There are now only half as many data points per ACP, and there is no overall stretching or shrinking of $\psi(t)$. Figure 1-8 shows the results of tuning a jittered signal composed of obliquity and red noise to a target signal of obliquity,

$$\begin{aligned} \psi(t') &= \sqrt{1-v}\,\eta(t') + \sqrt{v}\theta(t') \\ \tau(t) &= \theta(t) \end{aligned}$$

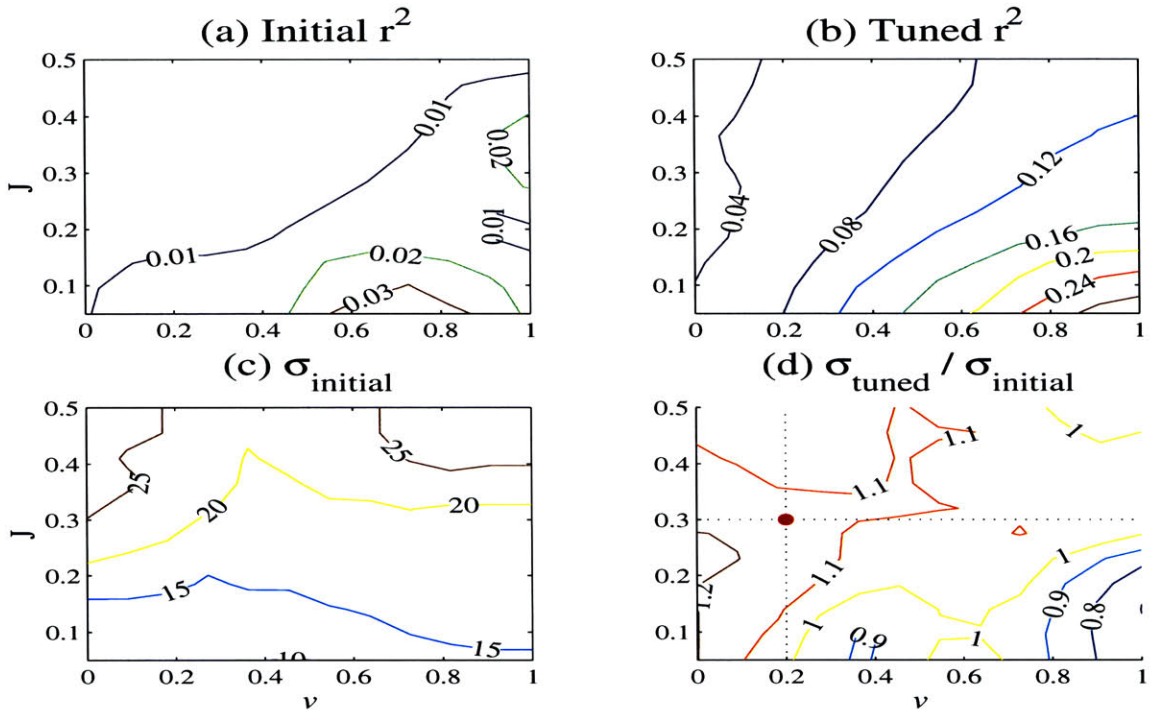

Figure 1-9: Same as Figure 1-8, but the orbital component of the signal, $\psi(t')$, and the target, $\tau(t)$, is precession.

Figure 1-9 shows a similar tuning result using red noise and precession

$$\begin{aligned} \psi(t') &= \sqrt{1-v}\,\eta(t') + \sqrt{v}p(t') \\ \tau(t) &= p(t) \end{aligned}$$

The initial σ_{rms} scales according to J and is equal for both obliquity and precession. The magnitude of the errors is about half the obliquity period while being a full precession cycle. The initial cross-correlation is uniformly small, and for the precession parameter is about half that of obliquity. This accords with higher frequencies being more susceptible to the effects of jitter. Tuning increases the obliquity cross-correlation more than precession, and for both scenarios the region of squared cross-correlation greater than 0.18 is coincident with the region where tuning shows skill ($\sigma_{\text{tuned}}/\sigma_{\text{initial}}$ less than one). Without the benefit of knowing the true age, however, it would be impossible to distinguish where the threshold for an improved age-model lies. For the obliquity simulation, tuning shows some skill with J less than 0.4 and v greater than 0.25, and for precession J less than 0.2 and v greater than 0.25. In chapters two and three it is estimated for the $\delta^{18}O$ records that $J = .3$

and that approximately 20% of $\delta^{18}O$ variance is linearly attributable to obliquity ($v_\theta = 0.13 \pm 0.07$) and precession ($v_p = 0.1 \pm 0.06$). This puts the $\delta^{18}O$ record outside the region where tuning shows skill (i.e. orbitally tuning the $\delta^{18}O$ records with XCM is expected to make the age-model less accurate). An individual $\delta^{18}O$ record with exceptionally low J or high v may be expected to yield a more accurate tuned age-model. Without an independent test for the accuracy of an age-model, however, it is impossible to judge if the tuning was successful.

The original intent of these orbital-tuning exercises was to find an algorithm capable of reliably generating more accurate age-models. A large variety of approaches were attempted, none of which demonstrated greater skill than the examples presented here. Experience with these tuning algorithms indicates that orbital-tuning is capable of correcting for systematic errors over long time scales such as an incorrect date on the B-M boundary. For more detailed corrections to an age-model, primarily a higher signal-to-noise ratio but also a lower accumulation rate jitter are required than what is estimated for the $\delta^{18}O$ record. There are three short-comings of the orbital-tuning approach. (1) There is no statistical test by which the accuracy of an orbitally-tuned record can be judged. (2) Monte Carlo simulations indicate orbital-tuning has poor skill in improving an age-model. (3) Perhaps most importantly, orbital-tuning a priori assumes a model of orbital climate change which it imposes upon the $\delta^{18}O$ record. Chapter two develops an alternative age-modeling technique which (1) has objective uncertainty estimates, (2) demonstrates skill in Monte Carlo tests, and (3) is devoid of all orbital assumptions.

Chapter 2

Depth-Tuned Age-models

An age-model based on a single linear age-depth relationship will be stretched or squeezed by each variation in sediment accumulation rate and, subject to certain simplifying assumptions, the variance in linear age from true age is expected to grow at a rate defined by the jitter ($J = \sigma^2/\bar{S}$, Eq 1.2). A procedure termed *depth-tuning* seeks to mitigate the effect of accumulation rate variations by incorporating multiple age-depth relationships into a single age-model. Procedures similar to depth-tuning have been used previously to develop age-models [e.g. *Hayes* 1976, *Williams* et al 1988, and *Raymo* 1997]. Each previous study, however, rejects the age-model implied by mean linear accumulation rates in favor of an orbitally-tuned model. This choice may reflect the influence of earlier radiometric dates for glacial termination two which accorded with the orbitally tuned age-models [e.g. *Broecker* et al, 1968; *Gallup* et al, 1994; and *Cheng* et al, 1996] and confidence in the Milankovitch theory [e.g. *Imbrie* et al, 1992]. Recently the Milankovitch theory has come under question [e.g. *Winograd* et al 1992, *Muller and MacDonald* 1997, *Elkibbi and Rial* 2001, and *Wunsch, 2002*] and radiometric ages for termination two which conflict with the orbital age-models have been reported [e.g. *Esat* et al 1999, *Henderson and Slowey* 2000, and *Gallup* 2002]. This present study uses significantly more isotopic records than previous studies and corrects for the effects of compaction. The resultant age-model accords with the recent radiometric constraints on termination ages. A statistical model of accumulation rates is developed to provide uncertainty estimates, and a Monte Carlo test with $\delta^{18}O$ -like signals indicates the $\delta^{18}O$ record can be accurately matched together. Finally, an empirical orthogonal functions (EOF) analysis of accumulation rates demonstrates basin-wide spatial patterns which are themselves of

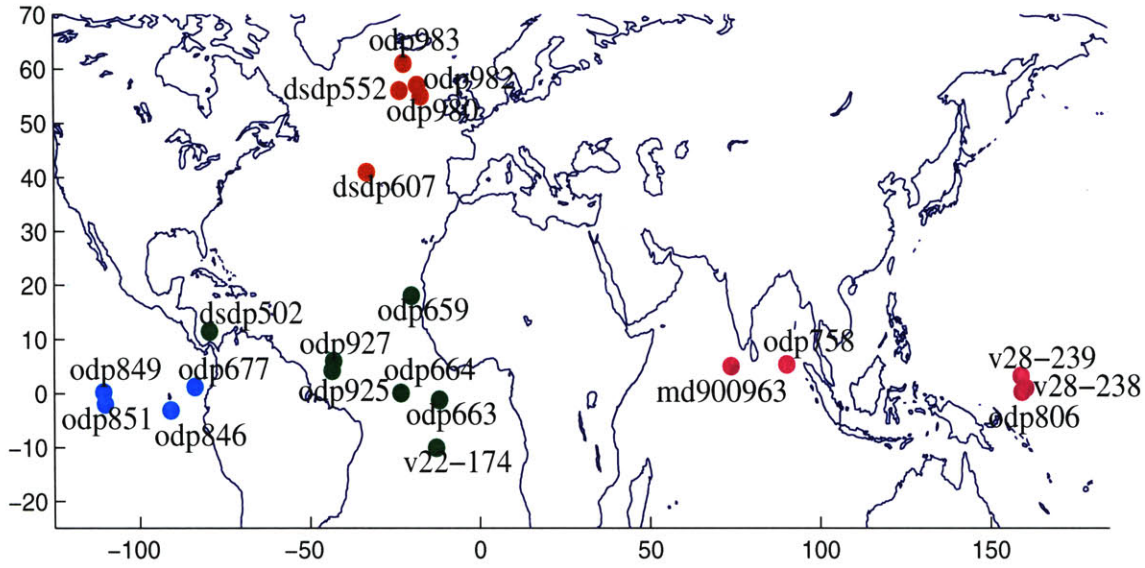

Figure 2-1: The locations of the records used in this study. Shading of dots indicate geographic groupings of cores.

climatic significance.

2.1 The $\delta^{18}O$ Records

An ensemble of 26 $\delta^{18}O$ records from 21 separate drill cores are used for this study whose location are shown in Figure 2-1. The core sites can be divided into four geographical regions; the North Atlantic, Indian Ocean and Western Equatorial Pacific, Equatorial Atlantic, and the Eastern Equatorial Pacific. The geographical distribution heavily favors the Northern Hemisphere and it would be useful to incorporate additional records, particularly in the Southern Hemisphere, as they become available. In five instances two separate $\delta^{18}O$ records based on benthic (bottom dwelling) and planktonic (surface dwelling) foraminifera species were measured within the same core. Table 2.1 lists the pertinent statistics and authors of each core. All $\delta^{18}O$ records which were available and extend through the Brunhes Matuyama magnetic reversal (B-M) were included in this study. Three of the records are from piston cores (V28-238, V28-239, and MD900963) while the remainder are Deep Sea Drilling Program (DSDP) or Ocean Drilling Program (ODP) sites which use a composite record spliced together from multiple holes drilled at each coring site. For ODP and DSDP sites the

Name	Reference	Species	$\bar{S}$	$\triangle t$	W. Dep	Lat	Lon
DSDP552M	*Shackleton and Hall*, 1984	B	1.9	6.4	2301	56N	23W
DSDP607M	*Ruddiman* et al, 1989	B	4.0	3.5	3427	41N	33W
ODP980	*Flower*, 1999	B	12.3	1.6	2169	55N	17W
ODP982	*Venz* et al, 1999	B,P	2.5	2.3,2.0	1134	57N	18W
ODP983	*Channell* el al, 1997	B	11.4	.9	1983	61N	22W
ODP677M	*Shackleton* et al, 1990	B,P	3.9	2.1,1.8	3461	1N	84W
ODP846M	*Mix* et al, 1995a	B	3.7	2.5	3461	3S	91W
ODP849M	*Mix* et al, 1995b	B	2.9	3.6	3296	0	111W
ODP851M	*Ravelo and Shackleton*, 1995	P	2.0	5.0	3760	2S	110W
DSDP502	*Prell*, 1982	P	1.9	6.5	3052	12N	79E
ODP659M	*Tiedemann* et al, 1994	B	3.1	3.9	3070	18N	21W
ODP663	*de Menocal* et al, unpublished	P	3.9	3.0	3706	1S	12W
ODP664M	*Raymo*, 1997	B	3.7	3.4	3806	0	23W
ODP925	*Bickert* et al, 1997	B	3.7	2.2	3041	4N	43W
ODP927	*Cullen* et al, 1997	B,P	4.5	3.2,2.2	3315	6N	43W
v22-174	*Thierstein* et al, 1977	P	1.8	5.3	2630	10S	13W
MD900963M	*Bassinot* et al, 1994	P	4.6	2.3	2446	5N	74E
ODP758M	*Chen* et al, 1995	B,P	1.6	6.5,6.7	2924	5N	90E
ODP806	*Berger* et al, 1994	B,P	2.0	4.8	2520	0	159E
V28-238M	*Shackleton and Opdyke*, 1976	P	1.5	5.5	3120	1N	160E
V28-239M	*Shackleton and Opdyke*, 1976	P	0.9	5.6	3490	3N	159E

Table 2.1: A list of the author and characteristics of each core. An 'M' appended to the name of a core indicates the B-M was identified via magnetic susceptibility measurements. From left to right there is $\delta^{18}O$ species B (benthic) and/or P planktonic, the mean sediment accumulation rate ($\bar{S}$, cm/KY), the mean interval between $\delta^{18}O$ measurements ($\triangle t, KY$), water depth (meters), and the latitude and longitude of each core site.

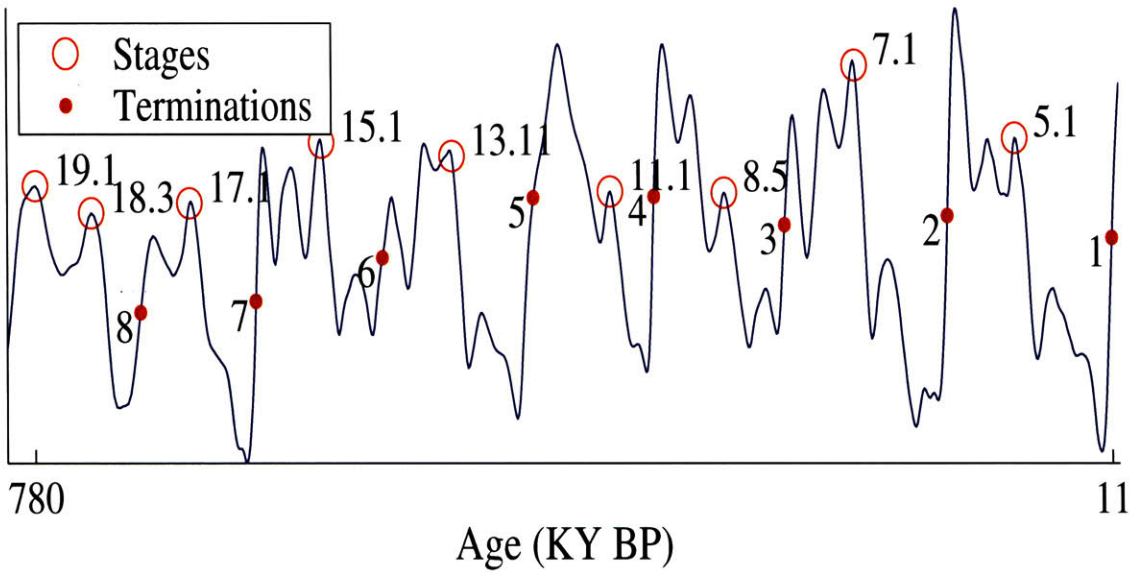

Figure 2-2: The SPECMAP $\delta^{18}O$ stack with the stages and termination mid-points used in this study indicated. The figure is oriented such that upward indicates lighter $\delta^{18}O$ (inter-glacial) and the x-axis is arbitrary between stage 19.1 and termination one.

composite depth scale or, if available, the revised composite depth scale was used.

2.2 Building a Depth-Tuned Age-Model

It is useful to define some vocabulary which will be used in developing the depth-tuned age-model. A $\delta^{18}O$ *event* is a feature in the $\delta^{18}O$ record which can be uniquely identified within each $\delta^{18}O$ record. Two types of events are referred to, *stages* and *terminations*. Stages are defined as local minima or maxima in the $\delta^{18}O$ record [*Prell* et al, 1986] where the numbering system suggested by *Imbrie* et al [1984] is used. All the stages referred to in this study have odd numbers after the decimal point, corresponding to low ice volume excursions in the $\delta^{18}O$ record. Terminations are defined as an abrupt shift from glacial to interglacial conditions [*Broecker*, 1984] where the depth of the midpoint between the local $\delta^{18}O$ minima and maxima is used. Figure 2-2 shows the eight termination mid-points and nine stages which are referred to in this study referenced to the SPECMAP $\delta^{18}O$ stack [*Imbrie* et al, 1984].

Depth-tuning is adapted from *Shaw*'s [1964] graphic correlation technique and proceeds in three parts. (1) The Brunhes Matuyama magnetic reversal (B-M) and

termination one are identified in each record and assigned radiometrically estimated ages. Only the portion of the record between the B-M and termination one is retained, between which ages are linearly interpolated with depth. (2) Under the assumption that $\delta^{18}O$ variations are global and synchronous, the records are correlated to one another to estimate simultaneous depths between the multiple records. (3) The age estimates (part 1) for the simultaneous depths (part 2) are averaged together to yield a mean age-depth relationship. Assuming variations in accumulation rate are uncorrelated, the mean age estimate is expected to be more accurate than simply taking age as linear with depth in a single core.

Uncertainties inherent in depth-tuning include the ability to uniquely identify and correlate $\delta^{18}O$ events given finite sampling resolution and the presence of noise. This possible ambiguity in event identification is addressed by correlating events both visually in section 2.2.2 and objectively in section 2.2.3, and then by a Monte Carlo test in section 2.3. Another uncertainty arises from possible asynchroneity between $\delta^{18}O$ events and is addressed in section 2.6.1. Finally, systematic distortions of the age-depth relationships due to changes in mean accumulation rate or core recovery artifacts could bias the resultant age-model, and these issues are also addressed in section 2.6.

2.2.1 Linear Age-Depth Model

To develop a linear age-depth relationship for each $\delta^{18}O$ record an age control points (ACP) is assigned at termination one (10.6 KY BP) and at the B-M magnetic reversal (780 KY BP). The depth of the B-M was reported in the literature as identifiable via magnetic stratigraphy in 12 of the 21 drill cores, and these cores are indicated by an "M" appended to the name in Table 2.1. For the $\delta^{18}O$ records associated with these 12 drill-cores the B-M invariably occurs within $\delta^{18}O$ stage 19.1. For core sites at which the B-M depth was not identifiable, the depth of stage 19.1 is instead used and an age of 780KY BP [see *Tauxe* et al, 1996] was assigned to both the B-M and stage 19.1. Between the two ACPs in each record age is linearly interpolated with depth. The resultant linear age-depth relationship is referred to as $E_j^{(2)}$ where 2 is the number of ACPs and j is the record number,

$$E_j^{(2)}(d_j) = \frac{t_2^{(2)} - t_1^{(2)}}{d_{j,2}^{(2)} - d_{j,1}^{(2)}} d_j + t_1^{(2)} \qquad d_{j,1}^{(2)} \leq d_j \leq d_{j,2}^{(2)} \tag{2.1}$$

$t_1^{(2)}$ and $d_{j,1}^{(2)}$ are the age and depth of ACP-1, $t_2^{(2)}$ and $d_{j,2}^{(2)}$ are the age and depth of ACP-2, and d_j is the depth of each $\delta^{18}O$ measurement from each record j. Though this notation is somewhat complicated, it can be used to explicitly represent how each age-model was constructed.

2.2.2 Visual Event Correlation

Pisias et al [1984] demonstrated that an ensemble of seven benthic $\delta^{18}O$ records could be consistently stratigraphically correlated over the last 300KY in two ways. The first method used visual identification of $\delta^{18}O$ events, and under the assumption that events are global and synchronous, correlates the corresponding depths within the ensemble of records. The second method uses Martinson's [1982] correlation algorithm to stretch and squeeze each of the $\delta^{18}O$ record to maximize cross-correlation between it and a chosen target $\delta^{18}O$ record. This yields a continuous depth transfer function relating each record to the target record. It is shown that both methods produce nearly identical stratigraphic correlations, and it was estimated that benthic $\delta^{18}O$ records can be correlated within a resolution of two to four KY. Here both visual event correlation and a cross-correlation maximization routine (XCM) are used to correlate the 26 $\delta^{18}O$ records between termination one and the B-M. In accordance with *Pisias* et al's conclusion, both the visual event and XCM correlation methods yield very similar results. Note, however, that *Pisias* et al sought a $\delta^{18}O$ stratigraphy and correlated records solely in the depth domain, while depth-tuning seeks an age-model and thus correlates records in the time domain.

The visual event correlation procedure is to (1) put the records onto the $E_j^{(2)}$ age-model, (2) identify common isotopic events in each record, (3) average the $E_j^{(2)}$ age of each event over all the records, and (4) constrain each event to occur at the average age for that event.

Seventeen events were visually identified in each core, the midpoint of the eight glacial terminations and stages 5.1, 7.1, 8.5, 11.1, 13.11, 15.1, 17.1, and 19.1. These events are spaced by roughly 50KY with terminations and stages sequentially alternating (see Figure 2-2). The end-points are termination one and stage 19.1 or, if available, the B-M magnetic reversal, and are fixed in age by independent radiometric dates. By linearly interpolating age with depth between the end-points, each record

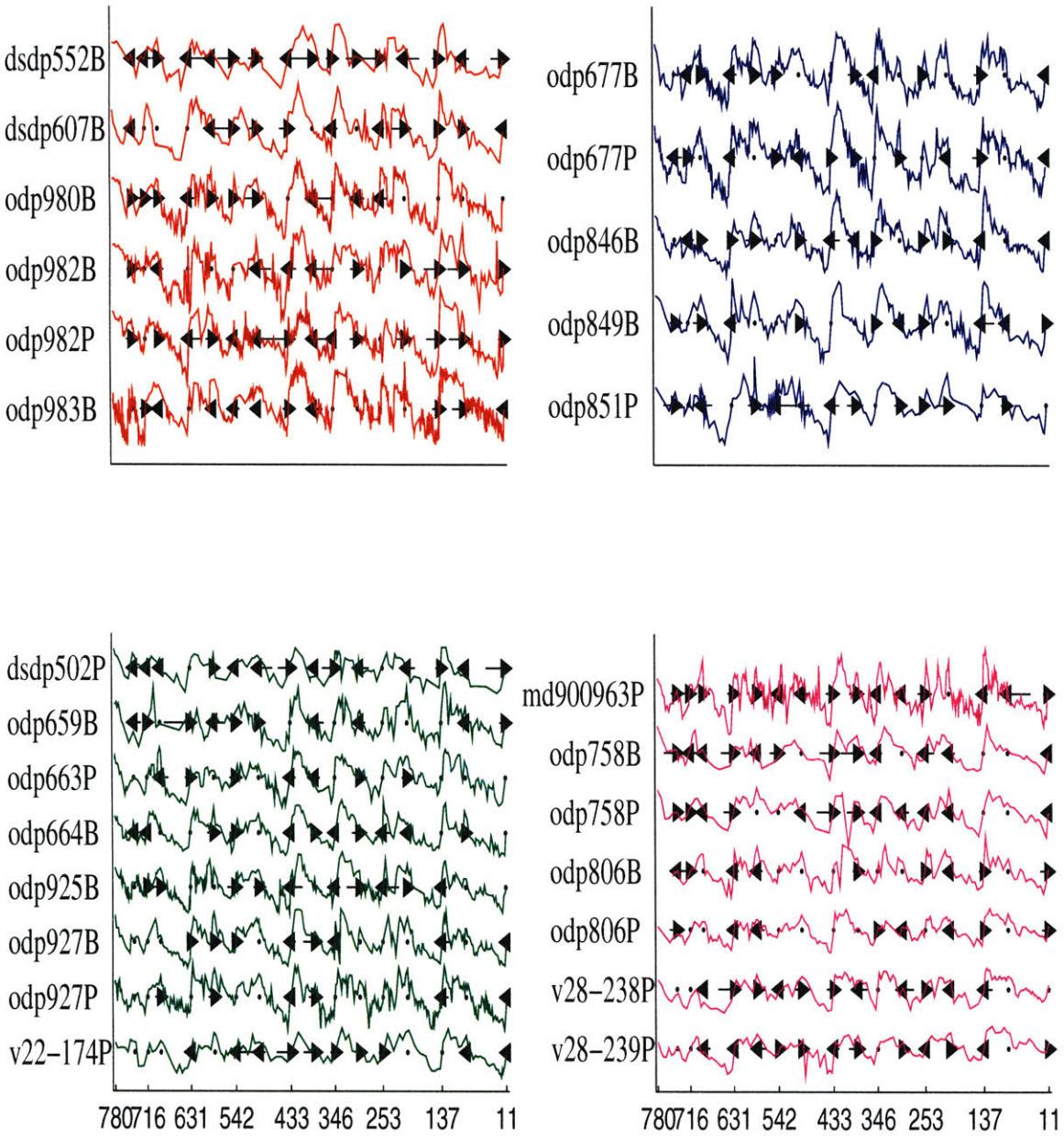

Figure 2-3: The $\delta^{18}O$ isotope records correlated for the $E^{(17)}$ age model. The x-axis is labeled with the $E^{(17)}$ age of each termination with time running from left to right. Arrows are located at each ACP indicating how the age model of the record was modified from a linear age-depth relationship between the preceding ACP and termination one. The letters B and P are appended to the name of each record to indicate it as benthic or planktonic.

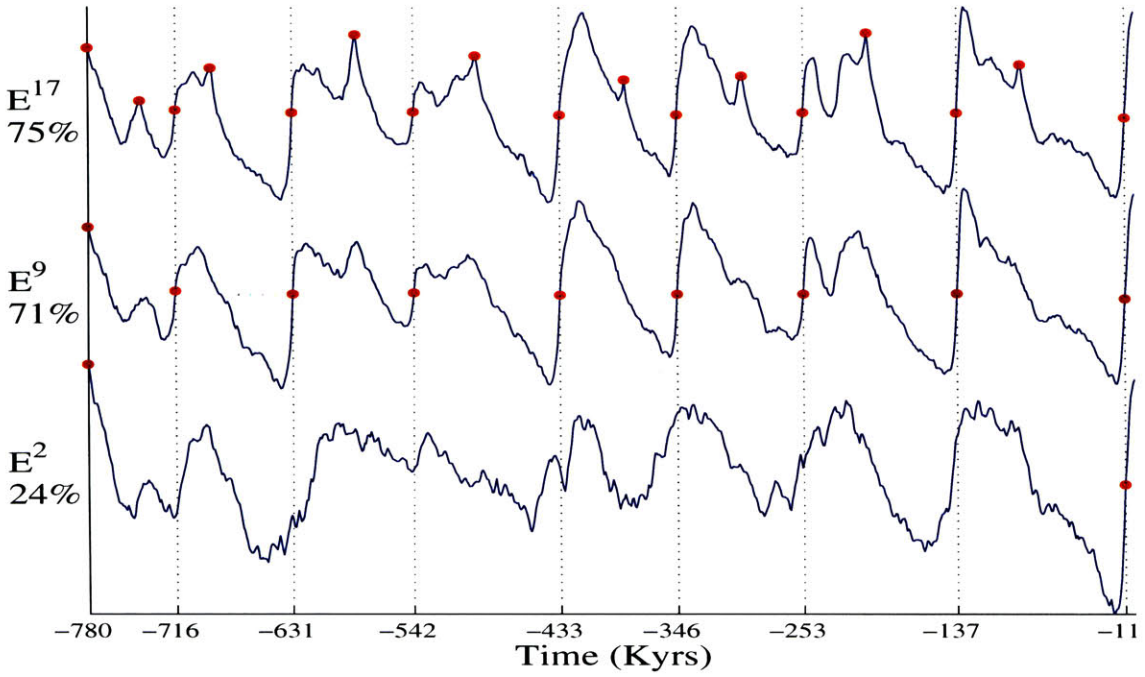

Figure 2-4: The leading EOF for the $E^{(2,9,17)}$ timescales.

provides an age estimate for the $\delta^{18}O$ events occurring between the end-points,

$$t_k^{(17)} = \sum_{j=1}^{26} g_j \frac{t_2^{(2)} - t_1^{(2)}}{d_{j,2}^{(2)} - d_{j,1}^{(2)}} d_{j,k}^{(17)} + t_1^{(2)} \qquad k = \{1, 2...17\}$$

The ratio of the time interval over the depth interval $(1/\bar{S})$ is the same as in Eq 2.1, but each record $(j = \{1, 2, 3...26\})$ is evaluated at the depths $(d_{j,k}^{(17)})$ of an approximately simultaneous $\delta^{18}O$ event. Each of the 21 core-sites are equally weighted in this average; thus the weighting coefficient is $g_j = 1/21$ except when two $\delta^{18}O$ records (benthic and planktonic) are from the same core and $g_j = 0.5/21$.

The depth-tune age-model is generated by constraining each record at $d_{j,k}$ to equal $t_k^{(17)}$, thus imposing 17 ACPs on each record

$$E_j^{(17)}(d_j) = \frac{t_k^{(17)} - t_{k-1}^{(17)}}{d_{j,k}^{(17)} - d_{j,k-1}^{(17)}} d_j + t_{k-1}^{(17)} \quad \begin{array}{l} j = \{1, 2, 3...26\} \\ k = \{1, 2, 3...17\} \\ d_{j,k-1}^{(17)} < d_j < d_{j,k}^{(17)} \end{array}$$

Ages between ACPs are linearly interpolated, yielding a piecewise linear age-model for each record, j, over depths d_j. These constraints can also be relaxed such that

only terminations and stage 19.1 are necessarily simultaneous, yielding the $E^{(9)}$ age-model. The terminations are the most conspicuous events in the $\delta^{18}O$ records and are the best radiometrically constrained features[1], and thus it is sensible to focus on the depth-tuned ages of the terminations. Table 2.2 indicates the age of each termination and stage 19.1 according to the $E_j^{(2)}$ age-model and the weighted average age of these terminations as calculated for $E_j^{(9)}$ (same as $t_k^{(17)}$ for $k = \{1, 3, 5...17\}$).

Figure 2-3 shows each record with an indication of the squeezing and stretching imposed in adjusting a record from the $E^{(2)}$ age-model to $E^{(17)}$. The records are grouped by geographical region. Note that there are no obvious systematic corrections according to geographical region or DSDP-ODP vs. V-MD cores. It is also apparent that the chosen set of events is identifiable in each $\delta^{18}O$ record. Figure 2-20 shows the leading empirical orthogonal function of the 26 isotopic records (EOF-1) pinned to the $E^{(2,9,17)}$ age-models. For EOF-1 of $E^{(2)}$, the discrepancy between termination times grows to such a large value that stage eleven is nearly wiped out and the squared cross-correlation is 0.24. Once each of the terminations are pinned ($E^{(9)}$), squared cross-correlation is 0.71, and increasing the number of ACPs to 17 only marginally increases the squared cross-correlation to 0.75. The EOF-1 for each age-model is almost identical to the mean of the ensemble of records.

2.2.3 Automated Record Correlation

The visual event correlation approach allows for the selection of individual events and yields an age for them, but involves a subjective judgment in deciding which events correspond to one another. The automated correlation procedure is to: (1) put all records on the linear age-depth model ($E^{(2)}$), (2) use XCM to correlate a base $\delta^{18}O$ record to each of the records, thus yielding 26 time adjustment function (including a zero adjustment for correlating the base function to itself), and (3) average the time adjustment functions to determine a mean age-depth relationship for the base record.

Take t'_j as the estimated time for record j according to $E_j^{(2)}$. By using XCM to correlate a base $\delta^{18}O$ record, $\psi_m(t'_m)$, to all available $\delta^{18}O$ records, $\psi_j(t'_j)$ with $j = \{1, 2...26\}$, 26 time transfer function are generated without the obligation of identifying $\delta^{18}O$ events in each core. Each correlation of $\psi_m(t'_m)$ to $\psi_j(t'_j)$ yields a

[1]The B-M boundary and Toba ash layer at 75 ± 5KY BP are notable exceptions. The B-M is included as a constraint, but the depth of the Toba ash layer has not yet been incorporated as an age control point.

site	Termination 1	2	3	4	5	6	7	8	S19.1	σ
DSPD552B	10.6	128	263	304	374	515	585	697	780	36
DSPD607B	10.6	139	221	328	425	503	598	708	780	19
ODP980BT	10.6	138	258	381	501	584	658	740	780	31
ODP982BT	10.6	102	180	257	387	539	627	725	780	31
ODP982PT	10.6	99	174	255	395	532	618	723	780	29
ODP983B	10.6	121	226	319	426	529	637	728	780	19
ODP677BT	10.6	155	260	350	429	540	615	704	780	23
ODP677PT	10.6	154	259	347	428	541	614	707	780	24
ODP846BT	10.6	149	262	355	440	559	626	700	780	25
ODP849BT	10.6	137	278	374	453	560	643	722	780	27
ODP851PT	10.6	127	216	290	363	488	629	735	780	32
DSPD502P	10.6	108	230	339	407	520	608	699	780	18
ODP659B	10.6	132	251	360	469	569	671	707	780	28
ODP663P	10.6	137	246	337	431	548	622	715	780	20
ODP664B	10.6	128	244	338	427	540	610	698	780	17
ODP925B	10.6	139	259	359	453	574	649	722	780	26
ODP927BT	10.6	144	282	377	446	562	636	713	780	29
ODP927PT	10.6	147	274	370	448	562	634	711	780	26
V22-174P	10.6	166	280	358	411	500	619	710	780	32
MD900963P	10.6	174	296	384	463	576	671	738	780	37
ODP758BT	10.6	178	303	419	485	566	647	717	780	37
ODP758PT	10.6	177	300	414	487	569	654	729	780	37
ODP806BT	10.6	117	232	320	400	510	612	703	780	14
ODP806PT	10.6	122	243	346	431	538	641	732	780	23
V28-238P	10.6	139	276	386	490	569	659	721	780	29
V28-239P	10.6	127	243	336	400	512	610	714	780	21
event tuning, $E^{(9)}$	11	137	253	346	433	542	631	716	780	
event σ	0	7	11	13	12	9	7	4	0	
record tuning, $R^{(63)}$	11	138	252	346	434	546	629	717	780	
record σ	0	7	11	13	12	10	7	4	0	
orbital-tuning	12	128	244	338	419	525	622	710	781	
orbital σ	4	2	3	4	5	12	4	12	6	

Table 2.2: Age of glacial terminations one through eight and stage 19.1 in KY BP for each record according to the $E^{(2)}$ age-model. The weighted mean of the $E^{(2)}$ termination ages yields the $E^{(9)}$ termination ages. The age of the terminations according to ODP677's benthic depth-tuned age-model, $R^{(63)}$, and the mean orbitally-tuned ages are also given. The orbital ages refer to all available orbital age-models up to and including those which postdate ODP677 (denoted by a T appended to the name). The orbital σ indicates the discrepancy between orbital age models. The σ of the age interval between terminations ($E^{(2)}$) is given in the right hand column.

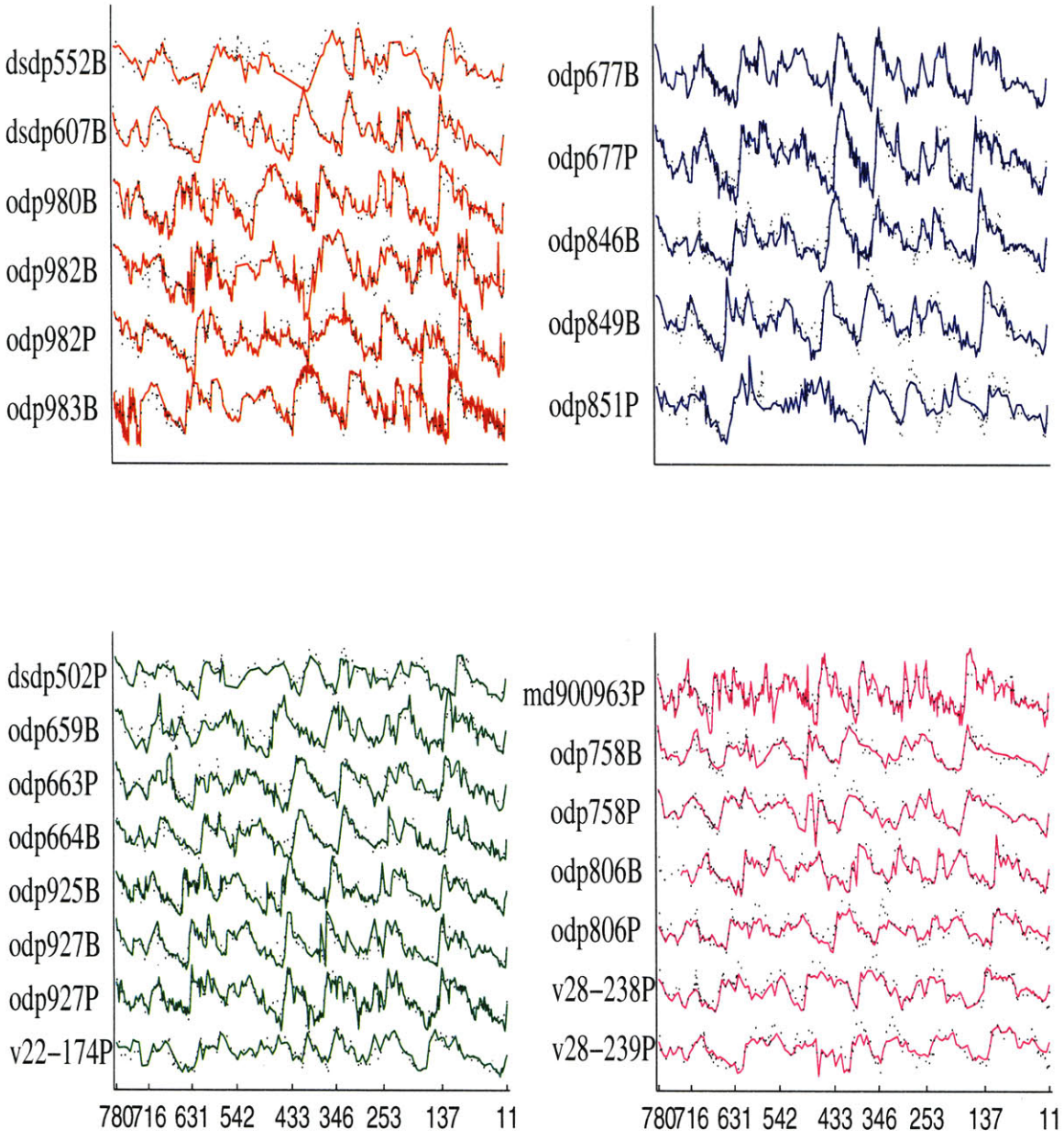

Figure 2-5: The benthic ODP677 record (dotted lines) matched to each $E^{(2)}$ age-model using XCM with 63 ACPs. This produces 26 age-model estimates for ODP677 which are averaged to yield the $R^{(63)}$ age-model.

new age adjustment estimate, $\psi(t'_m + \mu_j(t'_m))$. Insomuch as the $\delta^{18}O$ records are simultaneous and accurately correlated, $\psi(t'_m + \mu_j(t'_m))$ is an age-model for record m based on the age-depth relationship of record j, and when $j = m$ the adjustment function is zero. Taking the weighted average of each age adjustment term yields a mean age adjustment,

$$\bar{\mu}(t'_m) = \sum_{j=1}^{26} g_j \mu_j(t'_m)$$

where the weighting factor g_j is $1/22$, or if records are repeated in the same core, g_j is $0.5/22$. The record-tuned age-model for ψ_m is then $R^k_m = t'_m + \bar{\mu}(t'_m)$ where k indicates the number of ACPs used. XCM begins with one ACP (not including the end-points) and age control is sequentially increased by $2N + 1$ ACPs [i.e. 3,7,15,31,63,127]. The mean distance between ACPs is thus reduced by half for each iteration.

Figure 2-5 depicts the results of using XCM to correlate benthic ODP677 $\delta^{18}O$ with the ensemble of $\delta^{18}O$ records. Comparing this objectively estimated correlation with the visually correlated $\delta^{18}O$ records (see Figure 2-3) indicates both methods choose to correlated the same events. The mean squared cross-correlation achieved with 63 ACPs was 0.82, and the $R^{(63)}$ ages for each termination are listed in Table 2.2. Comparing the event tuned age-model, $E^{(9)}$, with the record tuned age-model, $R^{(63)}$, indicates both methods yield very similar results. All termination ages are within one KY except terminations six and seven which disagree by four and two KY respectively. Terminations six and seven, are typically less well-defined in the $\delta^{18}O$ records, making the correlations less reliable. Essentially both methods aim at the same result, the synchronization of isotopic events, and the age estimates are not independent of one another. However, the similarity between the subjective visual event correlation and objective XCM record correlation results indicates both correlation results are robust.

2.3 Monte Carlo Test of Depth-Tuning

In section 1.4 Monte Carlo tests were presented which indicated orbital tuning had little skill in recovering a more accurate age-model. It is appropriate to subject the depth-tuning process to a similar test. The test is conducted as follows: (1) generate two $\delta^{18}O$ like records composed of a common signal but disparate noise, (2) jitter the timescale of one record by degree J, (3) using XCM tune the jittered record to

the un-jittered record, and (4) estimate skill as the ratio of the tuned to the jittered time-scale rms errors.

2.3.1 Coherent and Incoherent $\delta^{18}O$ Energy

Synthetic $\delta^{18}O$ records are generated by conditioning noise to have a PSD similar to the $\delta^{18}O$ record. Figure 2-6 (top left) shows the smoothed mean PSD for the ensemble of 26 $\delta^{18}O$ records, $\bar{\Phi}_j(f)$, using the $E^{(17)}$ age model. While there is a bulge in energy near 1/100KY and to a lesser degree at other frequencies, the background continuum of the PSD is well approximated by

$$\bar{\Phi}_j(f) = \frac{1}{f^2 + \frac{1}{100^2}} \tag{2.2}$$

where the approximation has a -2 power law relationship giving way to white noise for frequencies less than 1/100KY, and thus is dominated by low frequency variations[2].

To simulate the $\delta^{18}O$ records it is useful to estimate the coherent and incoherent contributions to $\bar{\Phi}_j(f)$. Take $\Im_j$ as the Fourier transform of the unit variance zero mean record, j. Then the mean coherence between the ensemble of $\delta^{18}O$ records can be estimated as

$$\bar{C}(f) = \frac{1}{325} \sum_{j=1}^{25} \sum_{k=j+1}^{26} \frac{|\Im_j \Im_k|}{\sqrt{|\Im_j^2||\Im_k^2|}}$$

where the vertical bars indicate taking the magnitude of a complex function and 325 is the number of combination of j and k. $\bar{\Phi}(f)$ can now be broken into two components

$$\begin{aligned} \Phi^{(c)} &= \bar{\Phi}\bar{C}^2 \\ \Phi^{(i)} &= \bar{\Phi}(1 - \bar{C}^2) \end{aligned}$$

where $\Phi^{(c)}(f)$ is the coherent energy within the $\delta^{18}O$ ensemble and $\Phi_j^{(i)}(f)$ is the incoherent noise component. Figure 2-6 shows the PSD estimated for coherent and incoherent components which can respectively be approximated by,

$$\begin{aligned} \Phi^{(c)} &\sim \frac{1}{f^3 + \frac{1}{100^3}} \\ \Phi^{(i)} &\sim \frac{1}{f + \frac{1}{100}} \end{aligned}$$

[2]A power law of this form was proposed by *Hasselmann* [1976] in the context of rapid boundary layer heat fluxes driving slower ocean mixed layer temperature variations.

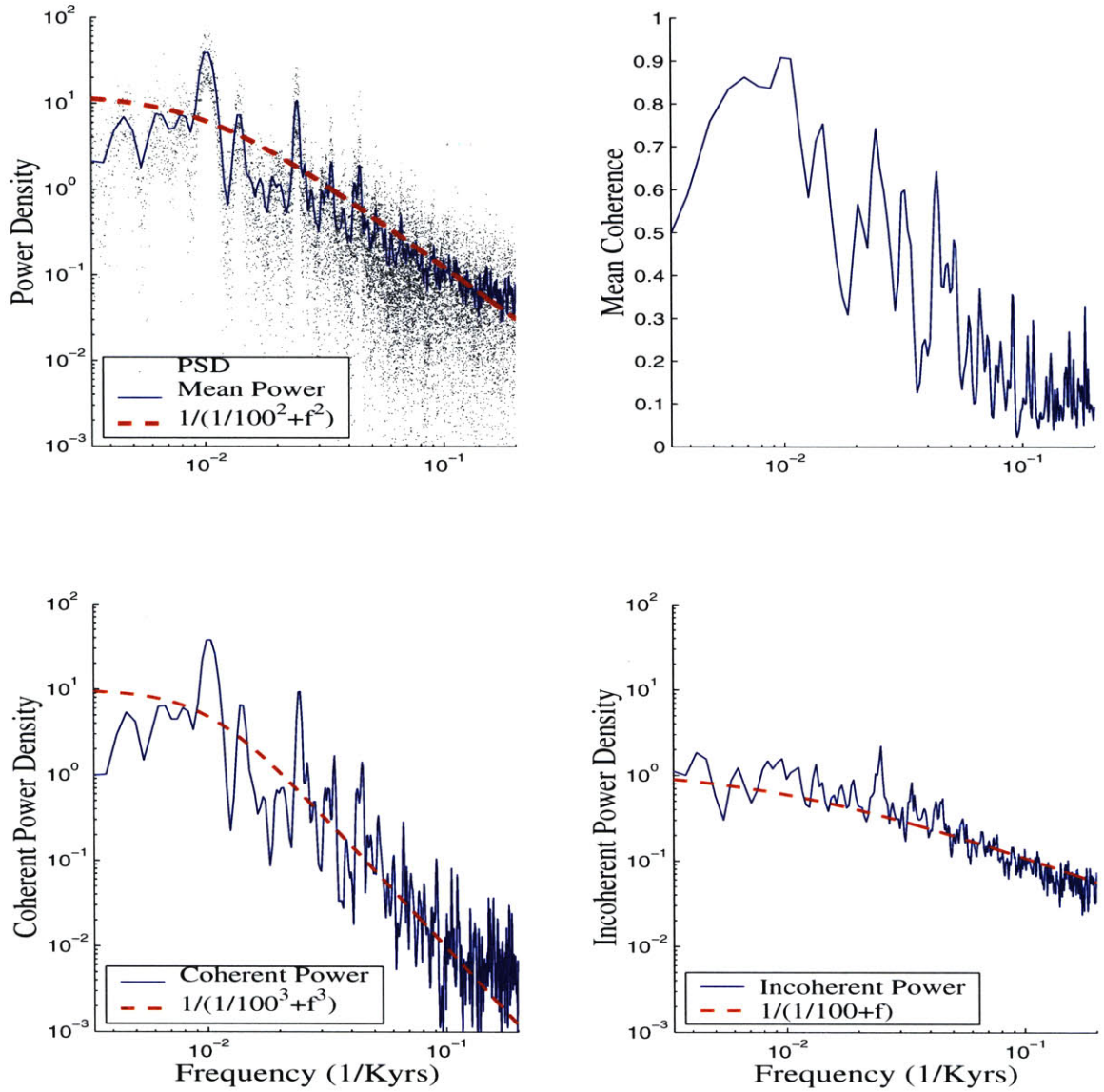

Figure 2-6: (top left) The power spectral density (PSD) estimate of all 26 records with the $E^{(17)}$ age-model. The mean PSD has a background spectrum with a -2 power law relationship for frequencies above 1/100KY. (top right) The mean coherence of the $\delta^{18}O$ records, $\bar{C}$. (bottom left) The coherent PSD with a -3 power law relationship, $\Phi^{(c)}(f)$. (bottom right) The incoherent PSD with a -1 power law relationship, $\Phi^{(i)}(f)$.

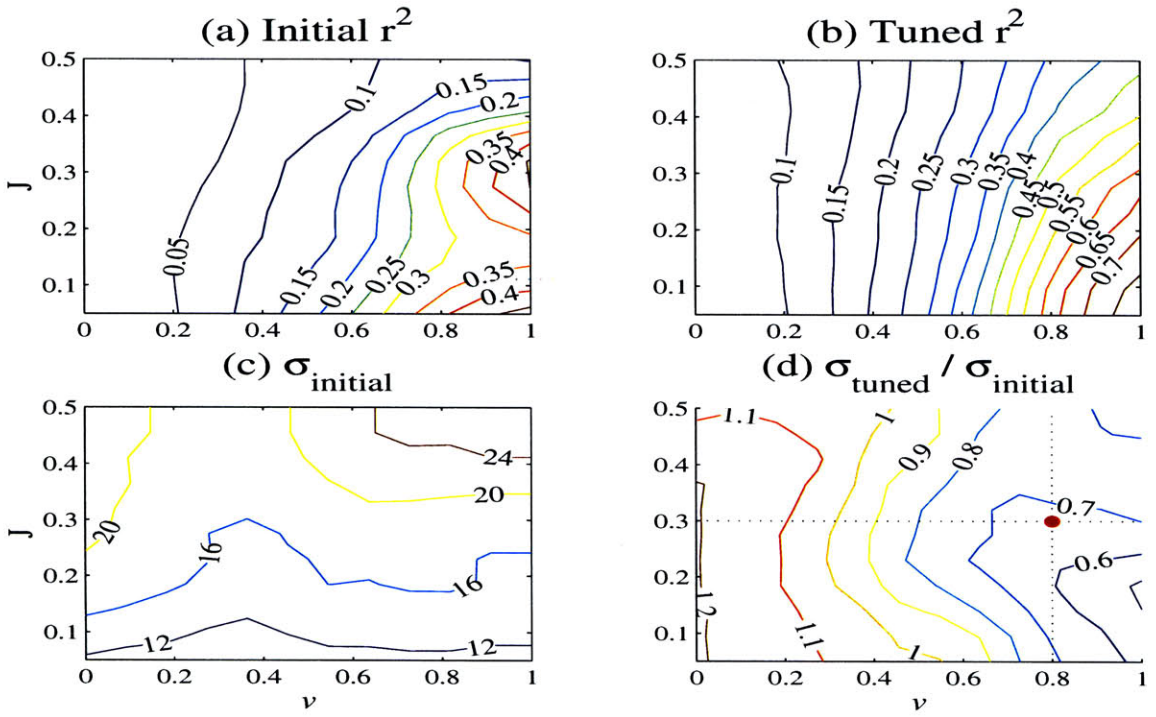

Figure 2-7: This mimics depth-tuning $\delta^{18}O$ records together. The plot is similar to Figure 1-8, showing (a) the initial r^2 between the records, (b) the tuned r^2, (c) initial rms age error, and (d) the ratio of tuned to initial rms age error ($\sigma_{tuned}/\sigma_{initial}$ less than one indicates skill). Note the significant increase in skill $\delta^{18}O$ record correlation displays over orbital-tuning. The dot indicates estimates of the common variance and jitter inherent to $\delta^{18}O$ records.

Apparently, for the $E^{(17)}$ age-model, the coherent energy is strongly dominated by the low frequencies while the incoherent component is only weakly red[3]. Results using the $E^{(9)}$ age-model yield very similar results, but it seems likely non-depth-tuning methods of $\delta^{18}O$ correlation could yield a somewhat different spectral composition of Φ.

2.3.2 Skill in Correlating $\delta^{18}O$ Records

To generate a pair of $\delta^{18}O$ like signals, noise with a PDS similar to the coherent and incoherent spectra are generated,

$$\begin{aligned} \psi^{(c)}(t) &= \Im^{-1}\{\eta^{(w)}\sqrt{\Phi^{(c)}(f)}\} \\ \psi_j^{(i)}(t) &= \Im^{-1}\{\eta_j^{(w)}\sqrt{\Phi^{(i)}(f)}\} \end{aligned}$$

$\Im^{-1}$ is the inverse Fourier transform and $\eta^{(w)}$ is complex white noise with a Gaussian magnitude distribution and uniform phase distribution. Both $\psi^{(c)}$ and $\psi^{(i)}$ are normalized to zero mean and unit variance, and these components are summed with a ratio of variances, v,

$$\psi_j(t) = \psi^{(c)}\sqrt{v} + \psi_j^{(i)}\sqrt{1-v} \qquad\qquad j = \{1,2\}$$

using two different realizations of the incoherent energy. The ratio of coherent signal to disparate noise variance is then $v/(1-v)$.

To simulate the $\delta^{18}O$ records age-depth relationship, noise is generated with a PDS similar to the sediment accumulation rates, S_j. In section 2.4 it is estimated the PDS of S_j is

$$\Phi^{(s)} \sim \frac{1}{1/60^2 + f^2}$$

In section 1.1 jitter is defined as $J = \sigma^2/\bar{S}^2$ where σ^2 is the variance of S. Thus a synthetic accumulation rate with a specified jitter (J) and PDS ($\Phi^{(s)}$) can be generated as,

$$S_j(t) = \Im^{-1}\{\eta_j^{(w)}\sqrt{J\Phi^{(s)}}\} + 1$$

where the sum of $\Phi^{(s)}$ is normalized to one. Summing the accumulation rate gives a depth profile, $d_j(t) = \sum S_j(t)$. If d(t) is linearly converted to age using an initial age, t_o, one has

$$t'_j = \frac{d_j(t)}{\bar{S}} + t_o$$

and the resultant age-model, t'_j, is jittered.

[3] A steep power law for the coherent energy indicates a climate system predominantly driven by low frequency forcing [see *Wunsch*, 2002]. This is in keeping with the simple glacial model presented in Chapter 3.

Having developed a method to generate jittered $\delta^{18}O$ like records, the skill of XCM in correlating two $\delta^{18}O$ records can be tested. Figure 2-7 shows the results of XCM correlating a jittered signal $\Psi_1(t')$ to $\Psi_2(t)$ over the range of $v = \{0.1, 0.2...1\}$ and $J = \{0.025, 0.05...0.5\}$. The results indicate that correlation is skillful over the entire range of J when v is greater than 0.4. There are two reasons why $\delta^{18}O$ records can be skillfully correlated to one another, but not skillfully correlated to an orbital signal. First, note that dv/dJ (the inverse slope of the contour lines in Figure 2-7) indicates the sensitivity of the initial r^2, tuned r^2, and $\sigma_{\text{tuned}}/\sigma_{\text{initial}}$ to the jitter. Apparently orbital-tuning has a much higher sensitivity to jitter (see Figures 1-8 and 1-9). Since low frequency signals are less susceptible to the effects of jitter [see *Thomson* and *Robinson*, 1996; *Wunsch*, 2000], the origin of the discrepancy in sensitivity can be inferred from the spectral distribution of the target signals. For orbital tuning the lowest target frequency is obliquity[4] (1/41KY), while for $\delta^{18}O$ correlation 80% of the coherent energy is concentrated at frequencies below that of obliquity. The second reason is that $\delta^{18}O$ records share approximately 80% of their variance in common (see next section), while only approximately 20% of $\delta^{18}O$ variance lies within the orbital bands.

The ability to skillfully correlate $\delta^{18}O$ records is a necessary precursor to building an age-model. A second process, however, with its own errors must be conducted to convert a depth correlation into time. These attendant uncertainties are discussed in section 2.6.

2.3.3 Estimate of the True Coherent $\delta^{18}O$ Energy

By Parseval's relationship [see *Bracewell*, 2000] the sum of the coherent energy divided by the total energy gives the fraction of variance shared in common between the ensemble of $\delta^{18}O$ records,

$$v = \frac{\sum \Phi^{(c)}(f)}{\sum \bar{\Phi}(f)} = 0.63$$

EOF-1 (see Figure 2-4, $E^{(17)}$ age-model) accounts for a similar fraction of the variance and is probably closely related to the coherent energy (also $E^{(17)}$) within the $\delta^{18}O$ ensemble. The $E^{(17)}$ age-model has ACPs spaced roughly every 50KY and it is likely

[4]The origins of the 100KY cycle are enigmatic, and any attempt to orbitally-tune to a 1/100KY signal involves questionable assumptions.

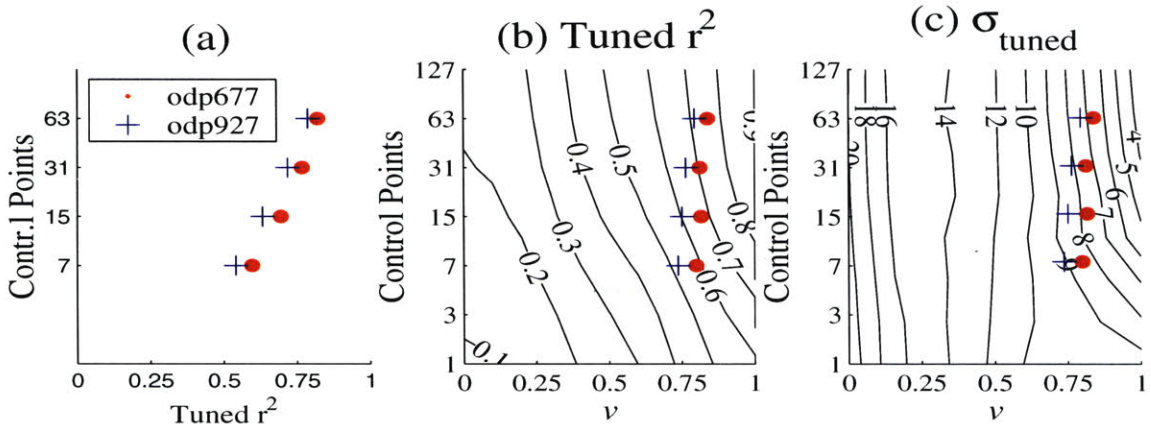

Figure 2-8: (a) The $\delta^{18}O$ records from ODP677 and ODP927 were correlated to every other record with between seven and 63 ACPs. The mean squared cross-correlation is plotted is plotted along the x-axis. (b) XCM is used to tune synthetic signals $\delta^{18}O$ signals over a range of true variance, v, and number of ACPs. The apparent squared cross-correlation is contoured and marks for the corresponding number of control points and observed variance are superimposed for ODP677 and ODP927. Apparently ODP677 and ODP927 truly share approximately 80% of their variance in common with the ensemble of $\delta^{18}O$ records. (c) The σ_{final} is plotted to give an indication of the accuracy of $\delta^{18}O$ record correlations. With 17 ACPs the average error in correlation between two records is approximately seven KY.

intervening $\delta^{18}O$ events are mis-correlated due to variation in accumulation rate. Assuming simultaneity between $\delta^{18}O$ events, a method is presented to estimate the true covariance between the $\delta^{18}O$ ensemble: (1) generate pairs of synthetic $\delta^{18}O$ like records with a true cross-correlation, v, (2) jitter the synthetic records and then use XCM to maximize their cross-correlation, (3) also use XCM to maximize the cross-correlation between the real $\delta^{18}O$ records, and (4) by matching the real and synthetic tuned cross-correlations, the corresponding true synthetic cross-correlation, v, can be inferred to apply for the real $\delta^{18}O$ records.

To begin, synthetic records $\psi_j(t)$ $j = \{1, 2\}$ are generated with v ranging from zero to one. To more closely mimic the observations, each ψ_j is resampled with measurement density varying from one and six KY, and then jittered with J equal to 0.3 (as estimated in section 2.6.2). The $\psi_j(t')$ signals are then tuned together with XCM using between seven and 63 ACPs. Figure 2-8(b) shows the relationship between the true shared variance (v), the number of ACPs, and the observed tuned squared cross-correlation (r^2). This provides an expected relationship between the

tuned and true cross-correlation values between records when a given number of ACPs are used with XCM.

Next, the ODP677 benthic $\delta^{18}O$ record is correlated to each of the real $\delta^{18}O$ records using XCM with a variable number of ACPs. The mean squared cross-correlation achieved between ODP677 and the ensemble of records for a given number of ACPs is shown in Figure 2-8(a) and shown interpolated onto the synthetic contour plot in Figure 2-8(b). Relative to the true synthetic cross-correlation, the interpolated location of ODP677 is nearly constant, indicating the expected and observed behaviors agree. This procedure is repeated with ODP927 planktonics, yielding similar results. By inference the true variance associated with the synthetic records is applicable to the real $\delta^{18}O$ records, and it is estimated that approximately 80% of the variance in the real $\delta^{18}O$ records is truly shared in common.

Uncertainties in this estimate arise from the assumption that $\delta^{18}O$ events are synchronous, likely leading to an over-estimate of the common variance. Conversely, bioturbational processes and sampling error (processes not included for in the synthetic $\delta^{18}O$ records) probably decrease the observed common variance. But irrespective of these uncertainties, it is clear $\delta^{18}O$ records share the majority of their variance in common and thus according to the Monte Carlo tests from the previous section, can be skillfully correlated.

Figure 2-8(c) shows the age error associated with the correlations of the synthetic signals. It is interesting to note how uncertainty is apparently a much stronger function of v than the number of ACPs. For the estimated common variance of 80%, the real $\delta^{18}O$ are expected to be accurately correlated to within a mean uncertainty of nine KY using seven ACPs and to within six KY using 63 ACPs. *Pisias* et al [1984] estimate a correlation uncertainty of two to four KY, but their estimates are based only on real $\delta^{18}O$ records and thus could not objectively measure age errors.

2.4 Temporal Correlation of Sediment Accumulation

An ensemble of depth-tuned $\delta^{18}O$ records allows for the characterization of both temporal and spatial patterns in accumulation rates. This analysis is of interest in its own right, because global variations in sediment accumulation over the last 800KY are climatic indicators, but seem to not have been previously analyzed. The spatial

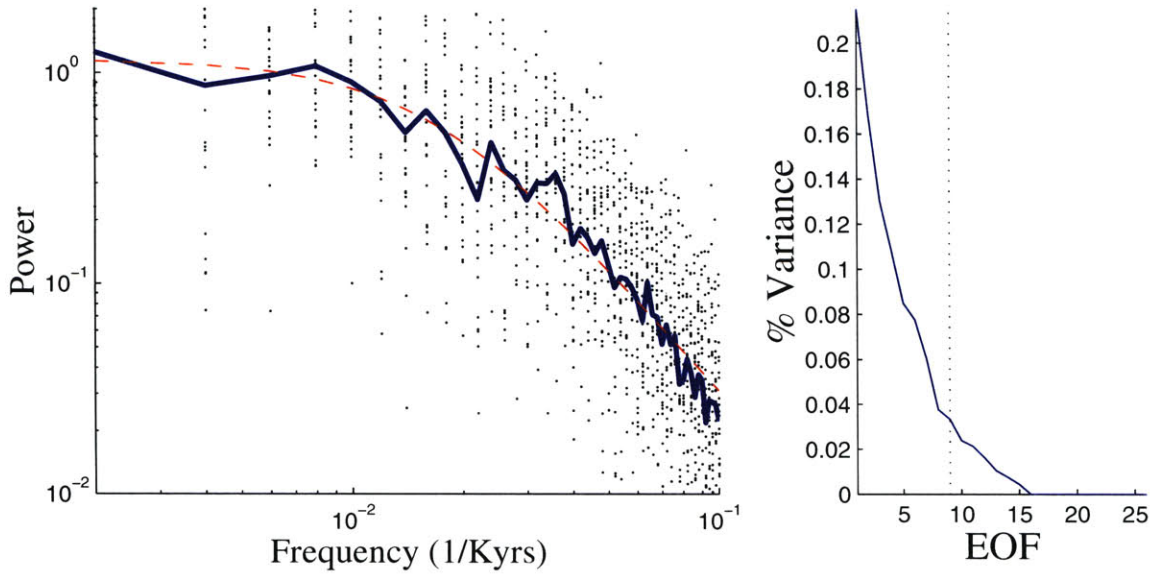

Figure 2-9: The left plot shows the power density spectrum of the anomalies in sediment accumulation rate, S', for each core (dots). S' is calculated from $R^{(127)}$ associated with each record. The mean PSD (solid line) compares well to the Power law relationship given by Eq 2.3 (dashed line). The right plot shows the percent variance explained by each EOF associated with the S' of each record as calculated from the $E^{(17)}$ age-model. The first nine EOFs (vertical dotted line) explain greater than 90% of the variance.

and temporal correlation in sediment accumulation are also of direct import to the accuracy of depth-tuned age-models. The results of this section and the next are used to develop a stochastic model of sediment accumulation which provides uncertainty estimates for the depth-tuned age-model.

2.4.1 Accumulation Rate Anomalies

Considering that sediment accumulation is itself a climate variable dependent on such factors as bioproductivity, ocean alkalinity, ocean currents, and terrigenous discharge, it seems likely that sediment accumulation rate anomalies, S', would be spatially and temporally correlated. A power density spectrum of S' for each core is shown in Figure 2-9. All records are constrained by a $R^{(127)}$ age-model where a large number of ACPs are used to extend the spectral estimate to higher frequencies (127 ACPs gives a mean sampling density of six KY and an associated Nyquist frequency of

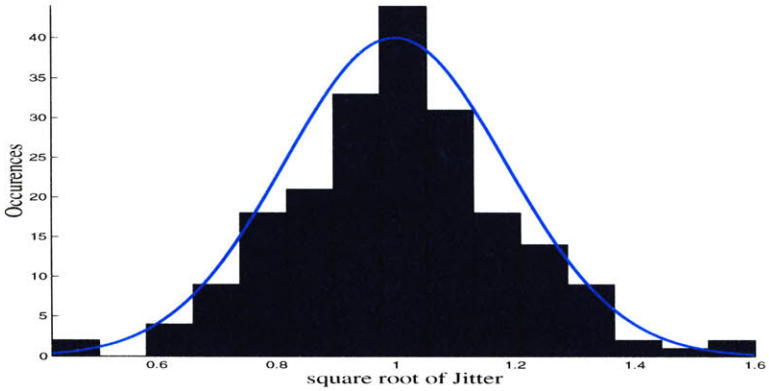

Figure 2-10: Histogram of the $S'/\bar{S} = \sqrt{J}$ inferred from the L17 time scale. The light blue line is a Gaussian distribution with a mean of one and a standard deviation of 0.17.

1/12KY) The observed power density relationship is well approximated by

$$\Phi^{(s)}(f) = \frac{1}{f^2 + \frac{1}{60^2}} \tag{2.3}$$

Compared with Eq 2.2, $P^{(s)}(f)$ transitions to white noise behavior at a higher frequency. All synthetic depth profiles used in this study are generated with a spectral behavior defined by Eq 2.3. It should be noted that S' only gives information about the deviations from mean global accumulation rates as monitored at these 26 core sites. If global accumulation rates vary though time, S may have a different autocorrelation relationship than estimated here. This is taken up in more detail next.

2.4.2 Mean Accumulation Rate

To gain insight into how mean accumulation rates vary through time, it is necessary to adopt an age-model derived independently of accumulation rates. The Devils Hole record [see *Winograd et al*, 1992] has just such and age-model and probably represents the best dated isotopic record in existence [see *Broecker*, 1992]. Devils Hole is an aquifer in Nevada (about 325Km from the S. California coast) from which a calcite vein was extracted, radiometrically dated, and measured for $\delta^{18}O$ variations. Figure 2-11 shows that variations in Devils Hole $\delta^{18}O$ bear a strong resemblance to variation in marine $\delta^{18}O$. But it is problematic to assign an absolute age to marine $\delta^{18}O$ based on the Devils Hole $\delta^{18}O$ record. Devils Hole is anti-correlated with marine $\delta^{18}O$ records and *Herbert* et al [2001] argue that Devils Hole $\delta^{18}O$ is consistent with

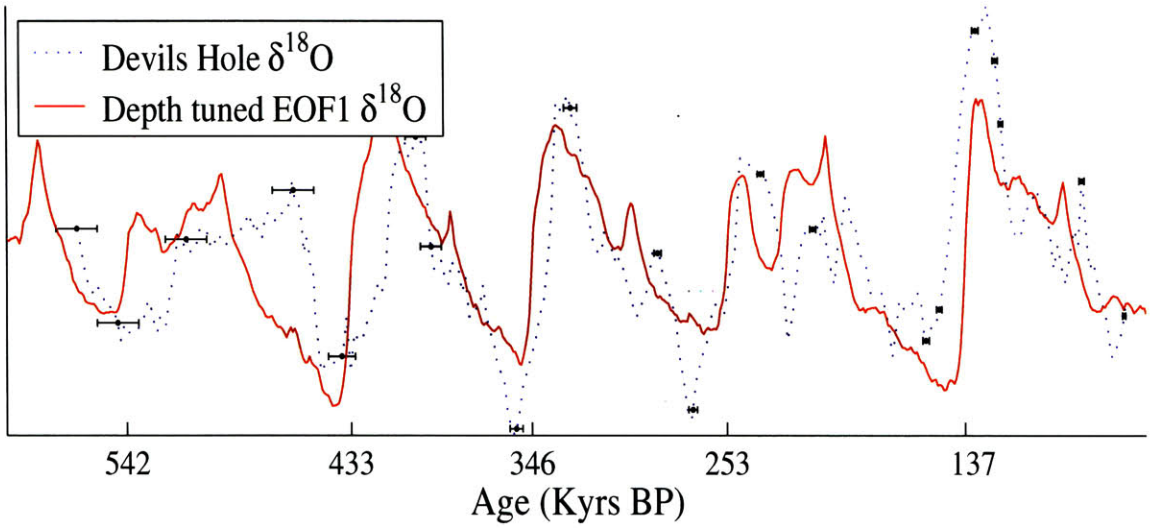

Figure 2-11: The Devils Hole $\delta^{18}O$ record inverted and plotted against the 1st EOF from the $E^{(17)}$ age-model. Both records are normalized, but since they are anti-correlated the y-axis of the Devils Hole record is reversed to facilitate comparisons. The horizontal black lines indicates one standard deviation uncertainties in the radiometric ages [see *Ludwig* et al, 1992].

SST patterns along the California margin rather than marine $\delta^{18}O$. Devils Hole $\delta^{18}O$ may also respond to local air temperature, local ground-water temperature, marine source water composition, and wind speed at the source region.

To the degree that Devils Hole $\delta^{18}O$ maintains a constant temporal lag relative to marine $\delta^{18}O$, accurate accumulation rates may be derived.

$$\bar{S} = \frac{\triangle t}{\triangle d} \tag{2.4}$$

Using the XCM routine, each of the 26 marine $\delta^{18}O$ were matched to Devils Hole using 127 ACPs. Such a large number of ACPs are used to attain a Nyquist frequency of 1/10KY in the ensuing spectral analysis. A mean squared cross-correlation of 0.81 was achieved and results are shown in Figure 2-12. The normalized mean accumulation rate of the ensemble of records was calculated as

$$\bar{S}(t) = \sum_{r=1}^{26} \frac{g_j}{\bar{S}_j} S_j(t) \tag{2.5}$$

where g_j is a weighting to account for cores with two isotopic records and $\bar{S}_j$ is the mean accumulation rate in core j. Figure 2-13 shows $\bar{S}(t)$ plotted against Devils Hole

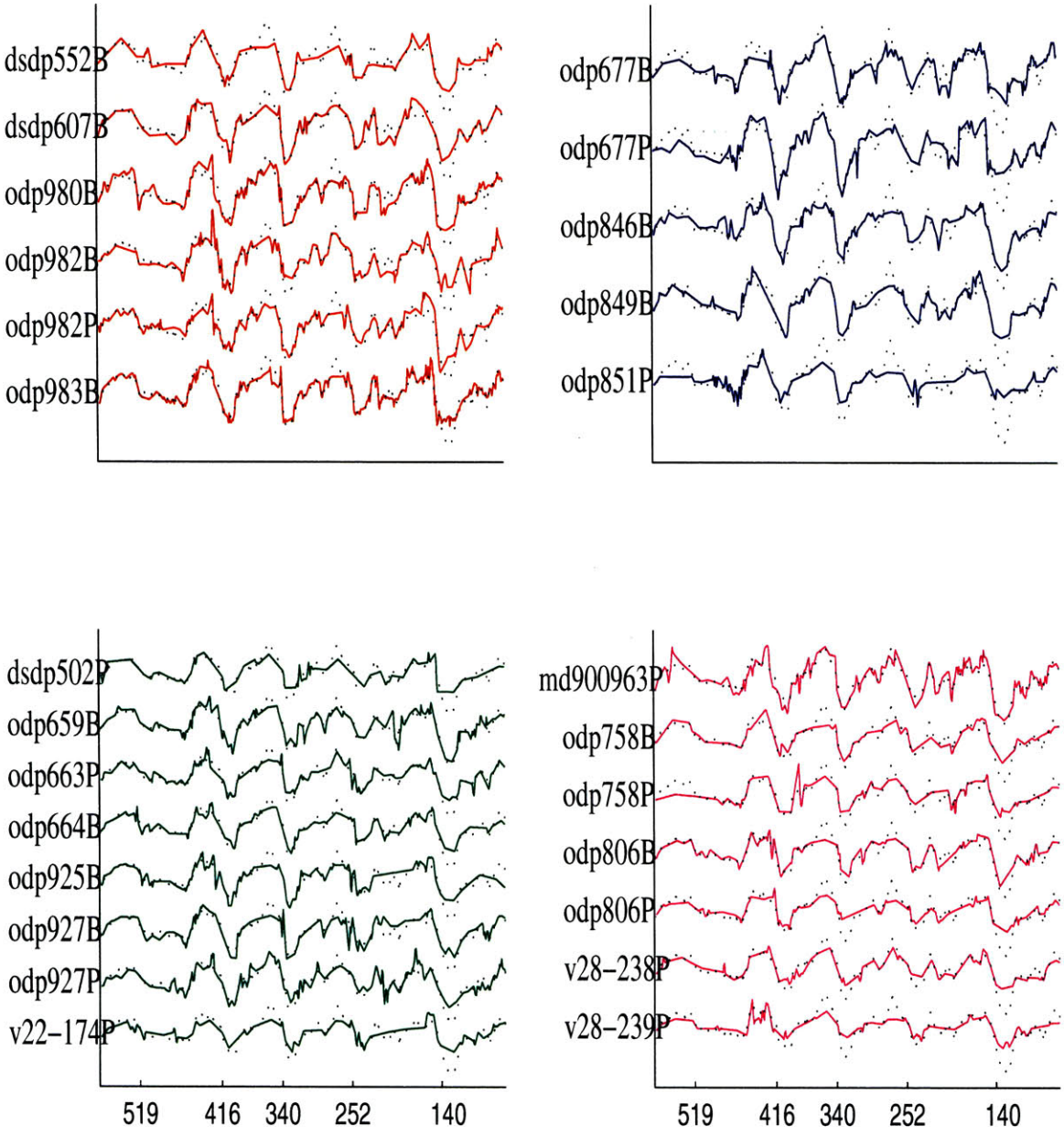

Figure 2-12: The ensemble of 26 marine $\delta^{18}O$ records each matched to the inverted Devils Hole $\delta^{18}O$ record. The ages plotted on the x-axis are the dates of the termination-like events from Devils Hole.

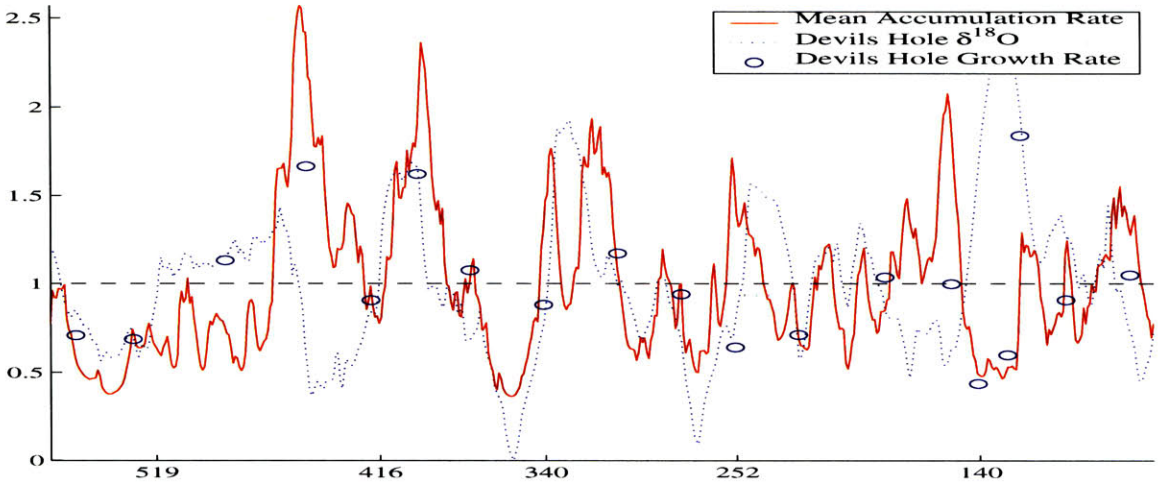

Figure 2-13: The estimated mean accumulation rate ratio, $\bar{S}_t$, for the ensemble of marine $\delta^{18}O$ records plotted against the Devils Hole $\delta^{18}O$ record.

$\delta^{18}O$. $\bar{S}(t)$ has a mean of one with variation from the mean representing percent change in mean ensemble accumulation rates. The coherence between $\bar{S}(t)$ and Devils Hole $\delta^{18}O$ is indistinguishable from noise, and there is no coherence above the 80% confidence level at frequencies below 1/15KY. In the sense that accumulation rates are a climatic variable and many climate proxies are linearly related, the absence of coherence is somewhat surprising. The PSD of $\bar{S}(t)$ (shown in Figure 2-14) is well approximated by the power law relationship from Eq 2.3. That both estimates of $\bar{S}(t)$ and S' have similar power law relationships indicates Eq 2.3 accurately represents the PSD of accumulation rates and the associated auto-correlation pattern.

The absence of a dominant periodic component in $\bar{S}(t)$ reduces the likelihood of harmonic FM in the difference between true age and the depth-tuned age-models. This becomes important in Chapter 3 because a periodic modulation in the errors of an age-model would generate a series of side-lobes for any spectral peak as indicated by Eq. 1.4 and the discussion thereof[5].

[5]It should noted *Mix* et al [1995] infer a generally red noise spectrum in accumulation rates which peaks at 1/100KY when an orbitally tuned age-model is applied to ODP846. These low frequency variation in accumulation rate seem to be continuous over the 1.8Ma span of the record but are incoherent with $\delta^{18}O$. Three issues which should later be addressed are: (1) by imposing a constant phase lag with the forcing, orbital tuning may de-modulate a truly frequency modulated climatic response, (2) a 100KY variation in accumulation rates may generate the 1/100KY combination tones with obliquity (discussed in Chapter 3), and (3) is there a pattern of accumulation rates which orbital tuning generally imposes in both sediment and ice-cores.

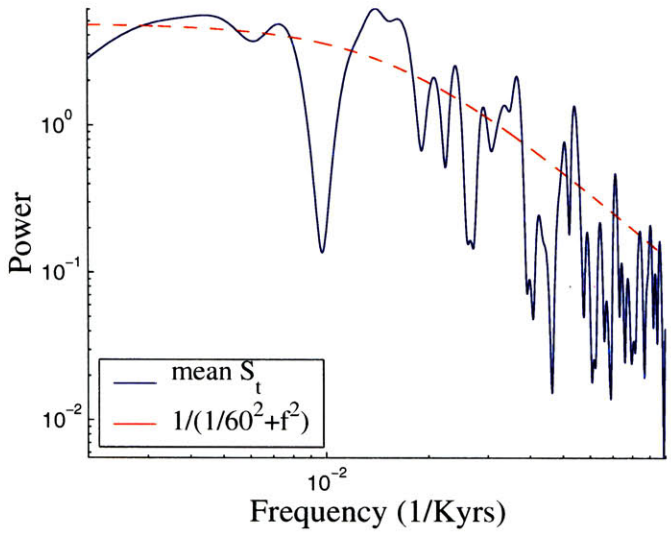

Figure 2-14: The PSD of the mean accumulation ratio and the power law fit from Eq 2.3

2.5 Spatial Correlation of Sediment Accumulation

Empirical orthogonal functions (EOFs) are used to estimate the degree of spatial correlation amongst the sediment accumulation rates at each core site. The calculation was performed using both the record and event tuned age-models over a range of ACPs, $R^{(7,15,31,63,127)}$ and $E^{(9,17)}$. The $R^{(15)}$ and $E^{(17)}$ levels of age control and higher (more ACPs) produce similar results. The maxim adopted here is to utilize the simplest age-model possible. Since the event tuned records yields S for synchronous periods across all records, and thus does not require interpolation, the $E^{(17)}$ age-model is adopted. A matrix of normalized accumulation rate anomalies is calculated as,

$$\begin{aligned}
\bar{S}_j &= \frac{d^{(17)}_{j,17} - d^{(17)}_{j,1}}{t^{(17)}_{17} - t^{(17)}_{1}} \qquad j = \{1, 2...26\} \\
S'_{j,k} &= \frac{d^{(17)}_{j,k+1} - d^{(17)}_{j,k}}{t^{(17)}_{k+1} - t^{(17)}_{k}} - \bar{S}_j \qquad k = \{1, 2...16\} \\
M_{j,k} &= \sqrt{J_{j,k}} = \frac{S'_{j,k}}{\bar{S}_j}
\end{aligned}$$

Where each matrix entry, $M_{j,k}$, is for record j and time interval $t^{(17)}_k$ to $t^{(17)}_{k+1}$. The EOFs of $M_{j,k}$ are used to estimate the degree of spatial correlation in variations of S through

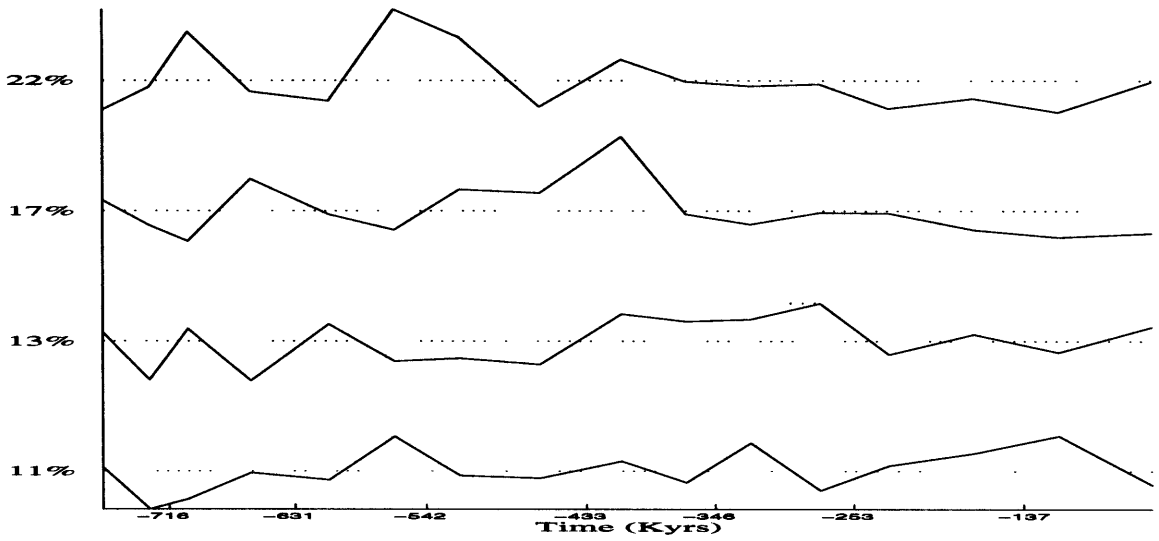

Figure 2-15: EOFs 1-4 (top to bottom) from an array of 26 normalized sediment accumulation rate records. The percentages listed to the left indicates the variance explained by each EOF. The times listed correspond to the $E^{(9)}$ ages of terminations eight through two.

time. Figure 2-9 shows that the first nine of the 26-EOFs explain more than 90% of the variance. This high degree of spatial correlation indicates roughly nine degrees of freedom in the age-depth relationships. Figure 2-10 shows a histogram of $S'/\bar{S}$ values inferred from the $E^{(17)}$ timescale. This distribution is approximately Gaussian with mean of 1 and a standard deviation of 0.17. Assuming nine independent age-depth relationship, averaging the 22 age-depth relationships gives a reduction in age error of approximately $1/\sqrt{9} = 1/3$.

Because depth-tuning calculates the age of each event as a function of mean accumulation rates, $\bar{S}$, regional anomalies in accumulation, S', appear as anti-correlations in the EOF spatial patterns. Estimates are normalized as $S'/\bar{S}$ to prevent unduly weighting the EOF analysis towards record with high accumulation rates. Figure 2-15 shows the four largest EOFs plotted against time. A positive value of the EOF indicates a pattern of anomalously high S at the indicated time. Figures 2-16 through 2-18 show maps indicating the spatial weighting of EOFs 1-3. For example, the positive value of EOF 2 (Figure 2-15) at 430KY BP maps to an anomalously high accumulation rate in the N. Atlantic (Figure 2-17)[6].

[6]This EOF technique could be more fully explored by analyzing core composition characteristics

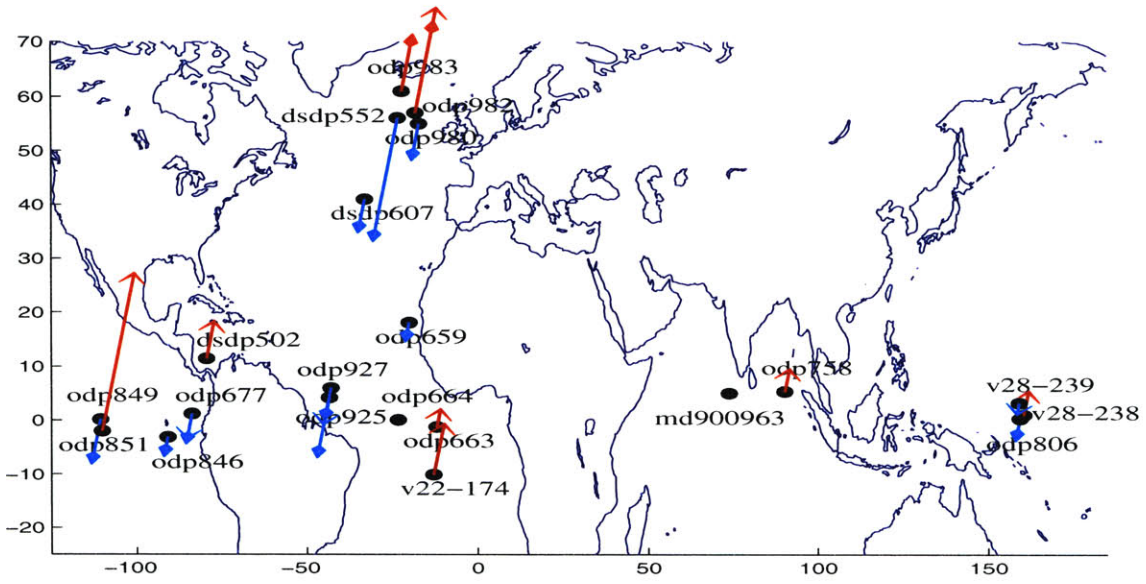

Figure 2-16: A map indicating the distribution of EOF-1. Arrow lengths are proportional to the standard deviation explained in a given record. Upward facing arrows indicate a positive contribution while downward arrows are negative. Slender arrowheads are from planktonic species and thick arrowheads are benthic. The chief features of EOF-1 are high SARs during terminations eight, six, and five. The strongest manifestations of this EOF are found in the two most shallow Atlantic cores and the deepest E. Pacific core.

EOF-1 displays an anti-correlation between shallow and deep cores in the Atlantic and Pacific. This anti-correlation may give a clue about dissolution cycles between the two ocean basins. The anti-correlations are strongest around terminations eight, six, and five. EOF-2 shows a strong anti-correlation between the North Atlantic cores and the rest of the records during termination five. Elevated North Atlantic accumulation rates may be associated with the collapse of a very large ice sheets as indicated by the $\delta^{18}O$ records. Perhaps this gives insight into why stage eleven appears to have such a long duration: a very large influx of sediment will have the effect of stretching time in a linear age-depth model. EOF-3 indicates that the North Atlantic, Indian, and western Pacific are anti-correlated with the eastern Pacific and mid-Atlantic regions between terminations five and three.

(e.g. carbonate content, porosity, and grain size).

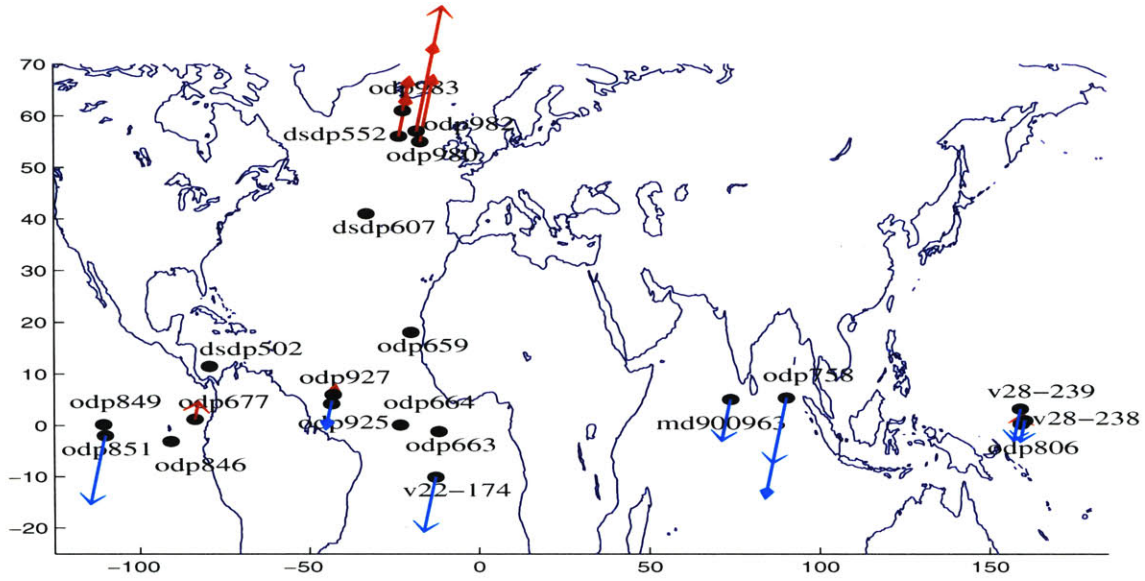

Figure 2-17: The primary feature of EOF2 is a relatively high SAR during Termination five centered in the N. Atlantic.

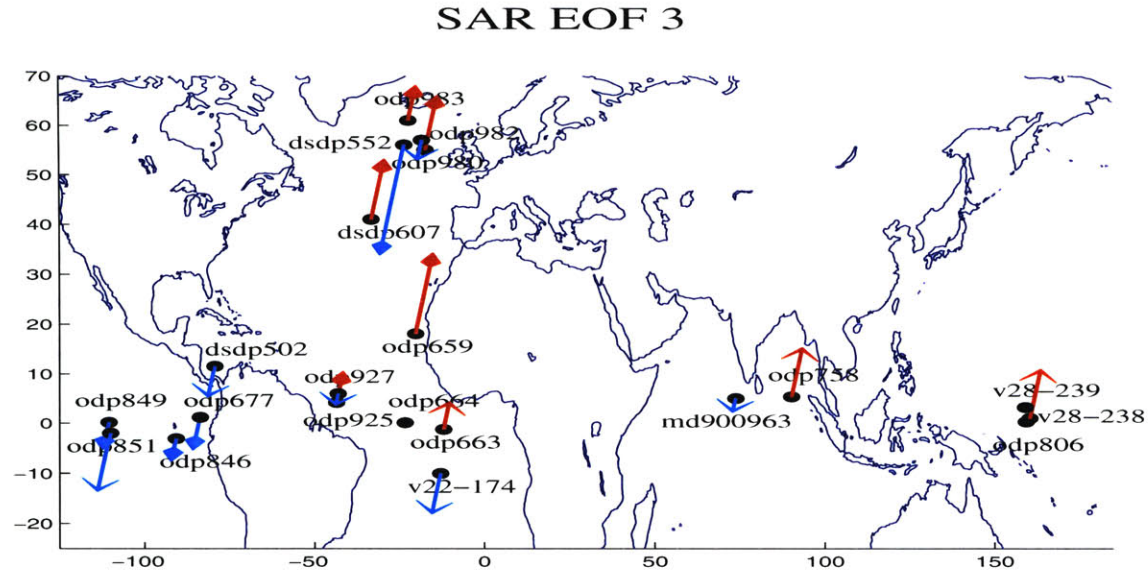

Figure 2-18: The primary features of EOF3 are elevated SARs between terminations five and three centered in the N. Atlantic, Indian, and E. equatorial Pacific oceans.

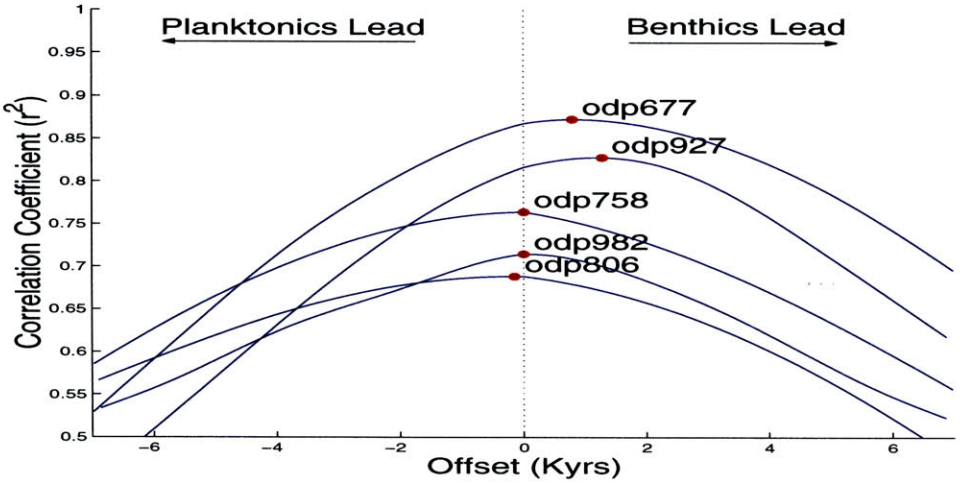

Figure 2-19: The cross-correlation relationship between benthic and planktonic $\delta^{18}O$ measurements where available in the same core. A positive lag indicates the benthic species leads the planktonic.

2.6 Age-Model Uncertainties

2.6.1 Synchroneity of Events

Both the event and record depth-tuning methods assume synchroneity between isotopic events in separate $\delta^{18}O$ records. This assumption is violated in at least two ways. (1) The ocean mixing times for the $\delta^{18}O$ signal can range out to 1000 years and longer [see *Wunsch*, 2002 radiocarbon paper]. Pinning $\delta^{18}O$ events to the same age de-blurs this effect. (2) $\delta^{18}O$ has changed in response to both ice-volume and temperature variations [e.g. *Schrag* et al, 1996]. If variations in temperature are not synchronous with ice-volume [e.g. *Herbert* et al, 2001], $\delta^{18}O$ records with different sensitivities to these variations will not be simultaneous.

An estimate of the age error incurred by time lags between isotopic events is afforded by benthic and planktonic species measured in the same core. Figure 2-19 shows the lagged cross-correlation between benthic and planktonic $\delta^{18}O$ measurements for the five cores where both measurements are available. All lagged correlations were calculated in the depth domain and then converted to equivalent time lags, using the $E^{(2)}$ age-model, to facilitate comparison. Here the benthics lead planktonics at two sites by approximately 1KY and are indistinguishable from simultaneous at the other three sites. It seems systematic physical lags between measurement

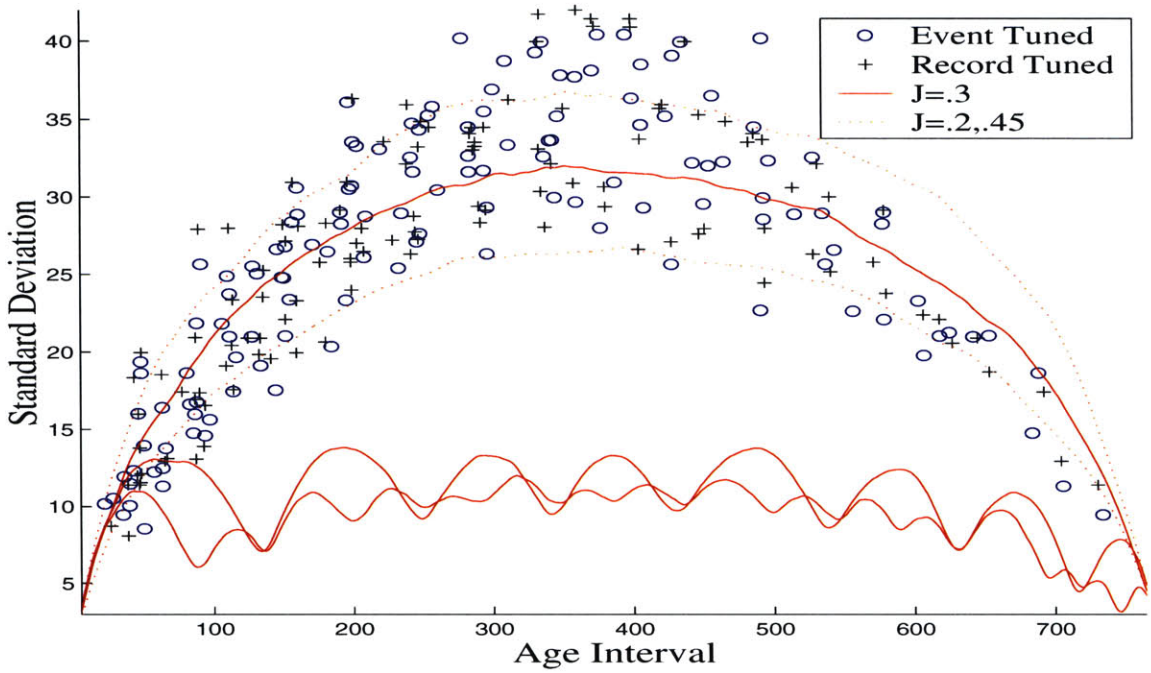

Figure 2-20: With only the ages of termination one and the BM constrained, a Brownian bridge in age error growth results. The observed standard deviations of age intervals for both the event correlation (crosses) and record correlation procedures (circles) are plotted along with the Monte Carlo estimate. The least squares best fit between observed and expected standard deviation is given with a jitter of 0.3 (top line) with upper and lower bounds of 0.2 and 0.45 (dashed lines). The estimated uncertainty for the $E^{(9)}$ (middle solid) and $E^{(17)}$ (bottom solid) age-models are also shown.

are overshadowed by the error inherent to correlating together noisy records (σ_{rms} approximately 6KY) [see Figure 2-8].

2.6.2 Uncertainties Due to Jitter

The largest source of uncertainty in the depth-tuned age-models is that sediment accumulation rates are not constant. A method to estimate these uncertainties is as follows. (1) Calculate the standard deviation in age intervals between simultaneous isotopic events in the ensemble of $\delta^{18}O$ records. (2) Constrain multiple realizations of the stochastic sediment accumulation model to an $E^{(2)}$ like age-model and calculate the simulated standard deviation in age intervals between isotopic events. (3) Adjust the jitter of the accumulation model such that the observed and simulated standard

deviation in age intervals agree in a least squares sense. (4) Use this estimate of the jitter to simulate age-depth relationship which are constrained with $E^{(9)}$ and $E^{(17)}$ like age-models. (5) The standard deviation between multiple realizations of the simulated constrained age-models provides uncertainty estimates for the depth-tuned age-models.

The variance in time intervals between pairs of isotopic events, k and m, are estimated using $E^{(2)}$ and the 17 events listed in section 2.2.2,

$$\sigma_{k,m} = \frac{1}{25}\sum_{j=1}^{26}\left|\{E_j^{(2)}(d_{j,m}^{(17)}) - E_j^{(2)}(d_{j,k}^{(17)})\} - \{t_m^{(17)} - t_k^{(17)}\}\right| \quad k = \{1, 2...16\}$$
$$m = \{k+1, k+2...17\}, \quad m > k$$

where the $E_j^{(2)}$ terms give the age interval for record j, the $t^{(17)}$ terms give the mean age interval, and the vertical bars indicate the absolute value. By plotting $\sigma_{k,m}$ for all combinations of k and m against $(t_m^{(17)} - t_k^{(17)})$ a profile referred to as a Brownian bridge (explained below) is observed (ref. Figure 2-20).

To estimate the jitter corresponding to the observed variance in age intervals, note the random walk age-model introduced as Eq 1.1,

$$t'_{n+1} = t'_n + \triangle t + \triangle t\frac{S'}{\bar{S}}$$

Here a unit time step in true time $\triangle t$ is corrupted by the ratio of S' to $\bar{S}$. By fixing the ages of the B-M boundary and termination one, the random walk in age error is constrained to begin and end at zero. Assuming S' to be Gaussian white noise, we can define a standard Brownian process $B_n = t'_n - n\triangle t$ whose variance is expected to grow linearly with time as $J = \mathrm{var}(S')/\bar{S}^2$. Following *Bhattacharya* and *Waymire* [Eq 12.1, 1990], the introduction of a second age constraint at the B-M reversal can be expressed as

$$B_n^* = B_n - \frac{n}{N}B_N$$

where N is the total number of time steps. B_n^* represents a *Brownian bridge* or *tied-down Brownian motion* and vanishes at the end points of the age-model, $B_n = 0$ when $n = 0, N$. The expected value of the Brownian bridge is $< B_n^* >= 0$ and its variance is

$$< (B_n^*)^2 >= Jn\triangle t(1 - \frac{n}{N}) \qquad n = 0, 1, 2...N \tag{2.6}$$

The maxima in expected variance occurs when $n = N/2$ giving

$$< (B_n^*)^2 >= \frac{J}{4} N \triangle t \tag{2.7}$$

where $N\triangle t$ is the elapsed time between the pair of fixed ages.

In order to accurately estimate the expected error in the depth-tuned age-models, however, the auto-correlation of accumulation rates implied by Eq 2.3 must be accounted for. The auto-correlation violates the assumption of white noise used to derive Eq 2.6, and a stochastic sediment accumulation model is used to estimate the jitter which would produce $\sigma_{k,m}$. Synthetic age-depth profiles are generated as described by Eq 2.3. To account for errors in locating end-point event depths a standard deviation of two KY for termination one and four KY for the B-M are included. This is less than average expected correlation error of five to nine KY since both termination one and the B-M reversal (or stage 19.1) are well resolved in the $\delta^{18}O$ records. A least squares best fit of the accumulation model to the observed $\sigma_{k,m}$ is achieved for $J = 0.3$ with upper and lower bounds of 0.45 and 0.2. For comparison purposes this estimate was also made using the record tuned age-model, $R^{(63)}$, and both results are shown in Figure 2-20 as $\sigma_{k,m}$ plotted against $(t_m^{(17)} - t_k^{(17)})$.

To estimate the errors in the $E^{(9)}$ and $E^{(17)}$ age-models, 26 synthetic age-depth relationship are first generated. Nine or seventeen *events* are identified in each record which are simultaneous to within plus or minus two KY. This gives nine or seventeen age control points (ACPs) which are distributed at the end-points (assigned at 10.6KY BP for termination one and 780KY BP for the B-M reversal) and at either 100KY or 50KY intervals between. From here the development of the respective age-models proceeds as outlined in section 2.2.2 with one important caveat. Only nine of the $E^{(2)}$ age estimates for each event are averaged corresponding to nine degrees of freedom in the age-depth relationships (see section 2.5). The ensemble of 26 synthetic records then provides as many estimates of time vs. depth. By calculating the standard deviation of the synthetic depth-tuned age from true age over each record, j,

$$\sigma^{(9,17)}(t) = \left(\frac{1}{25} \sum_{j=1}^{26} \left(E_j^{(9,17)}(t) - t \right)^2 \right)^{\frac{1}{2}}$$

a Brownian bridge like profile is generated. 1000 realization of the $\sigma^{(9)}(t)$ and $\sigma^{(17)}(t)$ were generated and the mean profiles are plotted in Figure 2-20. The $E^{(17)}$ age-model uncertainty is estimated to be, on average, 8.5KY, and the $E^{(9)}$ is 10KY.

Both $\sigma^{(9)}(t)$ and $\sigma^{(17)}(t)$ have as many local minimas as ACPs with small Brownian bridges between. It is important to note that increasing the number of ACPs will reduce growth of the small Brownian bridges, but only incorporating additional independent age-depth relationships will decrease the uncertainty inherent to the ACPs themselves. Since $\sigma^{(17)}(t)$ is dominated by ACP uncertainty, additional ACPs will not significantly decrease the uncertainty. This insensitivy to additional ACPs is also evident in Figure 2-8(c) where the contour intervals of age uncertainty are nearly parallel to the axis indicating the number of ACPs.

2.6.3 Systematic Errors

Systematic errors in depth-tuned ages could result from long-term variation in global mean accumulation rates, systematic sediment disturbances during core recovery, or compaction of sediments as they are buried [*Raymo*, 1997] . Correlation of the $\delta^{18}O$ records with Devils Hole did not indicate the presence of long-term accumulation rate variations, but $\delta^{87}Sr$ variations [*Farrell* et al, 1995] indicate river fluxes may have slightly decreased in the last 500KY. This would make depth-tuned ages systematically too young. Second, sediment extension could occur when cores are placed horizontally on deck. Since the upper portions of the core are typically more loosely compacted, these extensions could act to systematically bias records toward older ages. This error is mitigated by using termination one as the youngest ACP as opposed to the first available measurement. *Raymo* [1997] goes further and uses a radiometric constraint on the age of termination two. This radiometric constraint, compared with *Raymo*'s linear age-depth estimate, makes termination two relatively younger and leads to the inference of systematic core extension between termination one and two. In section 2.7.2 the radiometric constraints on termination two are discussed and interpreted as being consistent with the $E^{(9,17)}$ estimates. Thus, fixing the age of termination two would not change the results presented here. Finally, *Curry* et al [1995] show sediment compaction typically increases down-core, which would bias depth-tuning towards older ages. Because core logging data is available for many of the cores used in this study, the effects of compaction on age can be estimated and corrected for.

It seems previous accounts of the effects of compaction on linear age-depth relationships have been qualitative [e.g. *Hayes* 1976, *Williams* 1988, and *Raymo* 1997]. Here an age correction function is developed and applied to the $E^{(2,9,17)}$ age-models.

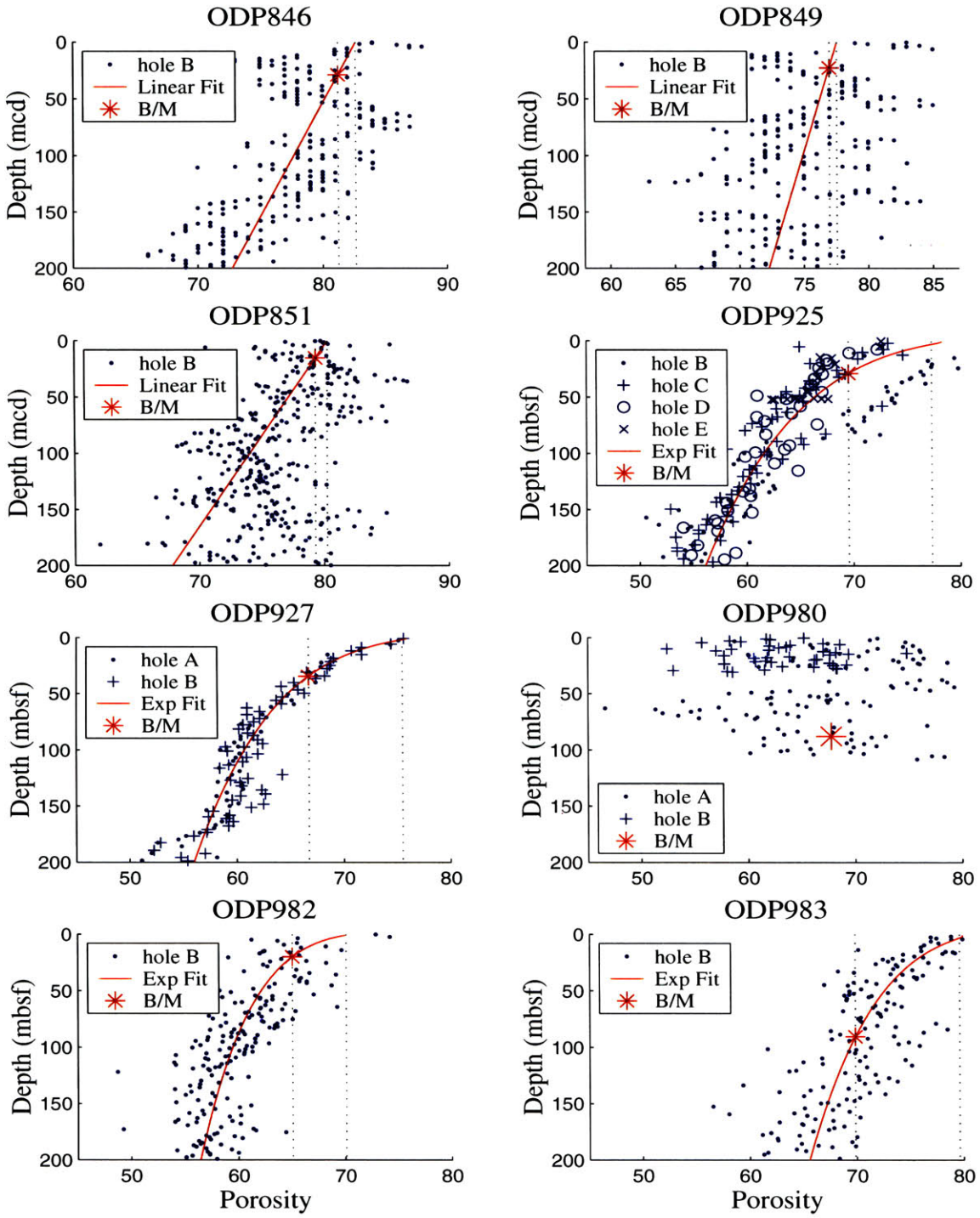

Figure 2-21: Changing porosity with depth in ODP cores from the E. Equatorial Pacific, Ceara Rise, and N. Atlantic. A simple curve was fit to each porosity profile, except for ODP980 which showed no distinct pattern. The star indicates the depth of the B-M magnetic reversal at each site and the vertical dotted lines indicate the change in porosity between Termination one and the B-M.

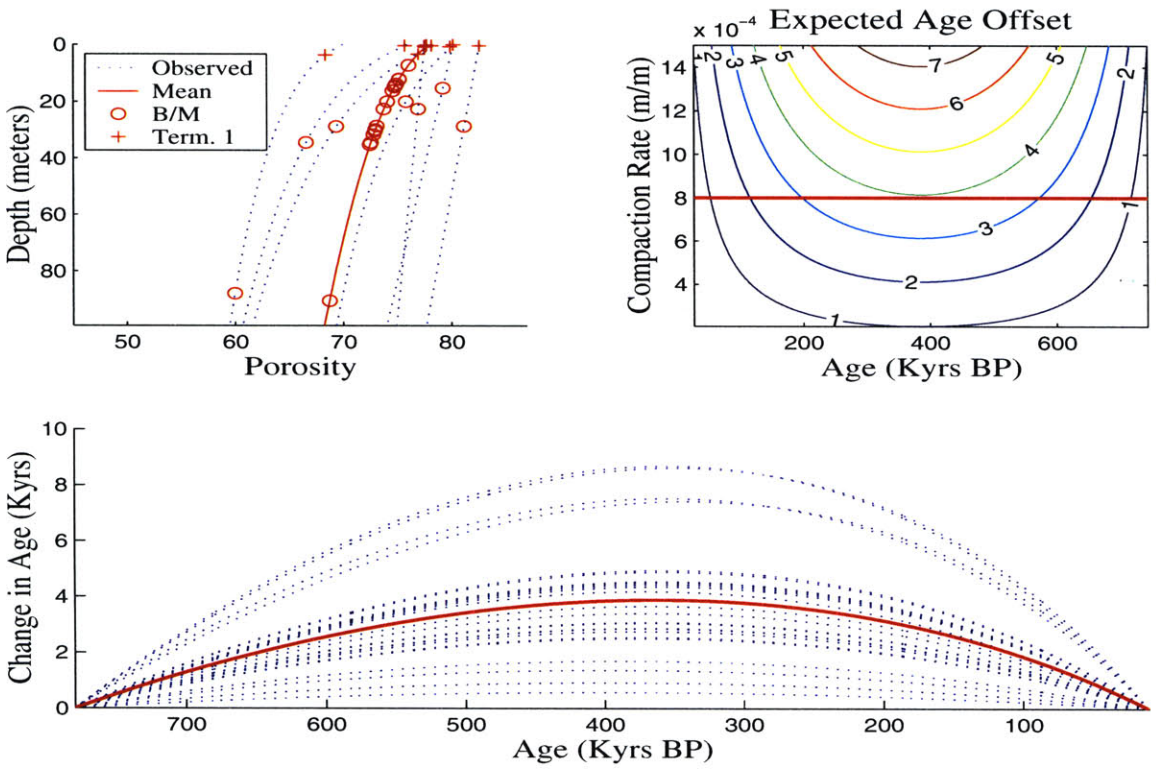

Figure 2-22: The estimated changes in porosity with depth (top left). This compaction leads to older apparent ages (in KY) as estimated by Eq 2.14 for a linear compaction rate, c, and a B-M depth of 50 meters (top right). The estimated age offset in each core (dotted) along with the weighted mean (solid) indicates mean ages appear from zero at the end points to nearly four KY older at 360KY BP. This degree of offset corresponds to a linear compaction rate of 8×10^{-4} (solid line top right).

Athy [1930] showed an increasing load on porous sediment results in compaction. Compaction results from a decrease in porosity (the fraction of sediment volume occupied by water) as pore water drains from the sediment matrix. Porosity is measured as

$$P = 1 - \frac{\rho_{bulk}}{\rho_{real}} \tag{2.8}$$

ρ_{bulk} is the dry mass divided by the volume of both the dry and wet mass; ρ_{real} is the mean density of the sediment grains. Given a functional relationship between depth and porosity, it is possible to estimate compaction's effect on a linear age-model. Take $h = 0$ and $t = 0$, as the height and date of the B-M magnetic reversal. Sediment

accumulates at a rate S so that

$$h = \int_0^t S(t)dt \tag{2.9}$$

and without compaction the final height would be, $h_f = \bar{S}t_f$. With compaction the height of the sediment column at any time is

$$h' = h - \int_0^h \triangle P(h_f - h)dh \tag{2.10}$$

where $\triangle P$ is the change in porosity resulting from the pressure of the overlying sediment at depth, $d = h_f - h$. Using the apparent mean accumulation rates to calculate age will introduce an age offset

$$\delta t = t - t' = \frac{t_f}{h_f}h - \frac{t_f}{h'_f}h' \tag{2.11}$$

For a linear compaction rate, c, one has $\triangle P = c(h_f - h)$ which yields

$$h' = h - ch_f h + \frac{c}{2}h^2 \tag{2.12}$$

$$\delta t = \frac{t_f}{h_f}h - \frac{t_f}{h_f - ch_f^2 + \frac{c}{2}h_f^2}(h - ch_f h + \frac{c}{2}h^2) \tag{2.13}$$

substituting $h = th_f/t_f$ and rearranging yields

$$\delta t = t\left(1 - \frac{1 - ch_f + \frac{ch_f}{2t_f}t}{1 - ch_f + \frac{ch_f}{2}}\right) \tag{2.14}$$

Age offsets increase with higher compaction rates and greater depth intervals per unit time interval, i.e. higher accumulation rates.

Figure 2-21 shows the depth porosity profiles for eight ODP cores located in the eastern equatorial Pacific [ODP846, 849 and 851 from Leg 138 ODP Initial Reports CD-ROM], Ceara Rise [ODP925 and 927 from Leg 154 Log and Core Data CD-ROM, Borehole Research Group, LDO], and the N. Atlantic regions [ODP980 982 and 983 from Leg 162 Log and Core Data CD-ROM, Borehole Research Group, LDO]. The first group shows a general trend of decreasing porosity with depth superimposed on a large degree of scatter. The scatter is probably largely due to variations in the composition of sediment and is implicitly accounted for in the jitter estimates. In this section it is the systematic trends which are investigated. To characterize the systematic changes in porosity a line was fit to these data points. The second group

from the Ceara Rise shows a distinct exponential decrease in porosity with depth. A second order exponential gives a good fit to these profiles, and two of the three cores from the N. Atlantic. All curves were fit over a depth range extending from 400 meters below sea floor to the core top. ODP980 from the N. Atlantic was alone in showing no trend, and was not included in estimates of mean porosity changes.

The curve fitted change in porosity, $\triangle P(d)$, is plotted as a function of depth in Figure 2-22 along with marks indicating the depth of termination one and the B-M magnetic reversal. The mean of these porosity curves was applied to cores for which porosity measurements were not available. The porosity curves indicate a range of mean compaction rates from $c = 2 \times 10^{-4}$ to 1.4×10^{-3} with a mean of 8×10^{-4}. The solution to equation 2.14 for this range in compaction, a B-M depth of 50 meters, and time extending from 780 to eleven KY BP, is contoured in Figure 2-22. A finite difference approximation of the actual porosity curves (bottom Figure 2-22) applied for each record shows the same behavior for δt as equation 2.14, except the exponential change in porosity shifts the location of maximum age offset towards slightly younger values. Table 2.3 lists the finite difference compaction correction at each termination for each $\delta^{18}O$ record. These corrections for compaction are applied to all subsequent invocations of the depth-tuned age-model. All corrections make $\delta^{18}O$ events relatively younger and range from zero at the endpoints to four KY at 350KY BP.

Another potential source of errors are artifacts associated with the core recovery process. Gaps between core segments or inaccurate measurements of depth below sea floor could introduce a bias. In an attempt to identify such potential sources of error, correlations in accumulation rate and core recovery length were searched for, and comparisons between the ODP and DSDP sites were made. However, no such systematic biases were identified.

2.7 Comparing the Orbital and Depth-tuned Age-models

Figure 28 shows the discrepancy between the depth-tuned ($E^{(17)}$ and $R^{(63)}$) and orbitally-tuned (O^{23}, i.e. using 23 ACPs) age-models for the benthic $\delta^{18}O$ from ODP677 [*Shackleton* et al, 1990]. With the mid-point of termination one and the B-M fixed to the same age, the O^{23} terminations average eight KY younger than the $E^{(17)}$ and $R^{(63)}$ termination ages. There are large positive and negative age ex-

site	termination 2	3	4	5	6	7	8
DSDP552B	1.6	2.6	2.8	2.8	2.5	2.0	1.0
DSDP607B	2.9	3.9	4.5	4.4	3.9	3.0	1.3
ODP980B	4.6	7.1	7.3	6.3	4.9	3.3	1.2
ODP982B	1.9	3.1	3.8	4.2	3.4	2.5	1.0
ODP982P	1.6	2.5	3.1	3.4	2.8	2.1	0.8
ODP983B	4.4	6.6	7.5	7.3	6.2	4.1	1.7
ODP677B	3.1	4.1	4.4	4.3	3.5	2.7	1.4
ODP677P	3.0	4.1	4.4	4.3	3.5	2.7	1.3
ODP846B	0.8	1.2	1.3	1.3	1.1	0.9	0.5
ODP849B	0.3	0.5	0.6	0.6	0.5	0.3	0.2
ODP851P	0.5	0.7	0.8	0.9	0.9	0.6	0.2
DSPD502P	1.4	2.5	2.8	2.8	2.5	1.8	1.0
ODP659B	2.2	3.3	3.7	3.4	2.7	1.6	1.1
ODP663P	2.8	4.1	4.5	4.3	3.5	2.6	1.2
ODP664B	2.6	3.9	4.3	4.2	3.5	2.7	1.5
ODP925B	5.6	8.1	8.7	8.2	6.2	4.3	2.1
ODP927B	5.8	8.4	8.6	8.1	6.3	4.6	2.3
ODP927P	7.5	4.6	4.9	4.6	3.6	2.7	1.4
B22-174P	1.9	2.6	2.7	2.7	2.5	1.7	0.8
MD900963P	3.7	4.8	4.9	4.6	3.5	2.1	0.9
ODP758B	1.8	2.5	2.5	2.3	1.9	1.3	0.7
ODP758P	1.8	2.4	2.5	2.3	1.9	1.3	0.6
ODP806B	1.6	2.7	3.0	3.1	2.7	1.9	1.0
ODP806P	1.7	2.7	3.0	3.0	2.5	1.7	0.6
V28-238P	1.5	2.4	2.5	2.3	1.9	1.2	0.7
V28-239P	0.9	1.5	1.7	1.7	1.5	1.1	0.5
mean	2.6	3.6	3.9	3.7	3.1	2.2	1.0

Table 2.3: The age corrections in KY applied to each core. All age corrections produce a relatively younger age-model, and while the corrections are continuous functions of depth, they are listed here only for terminations two through eight.

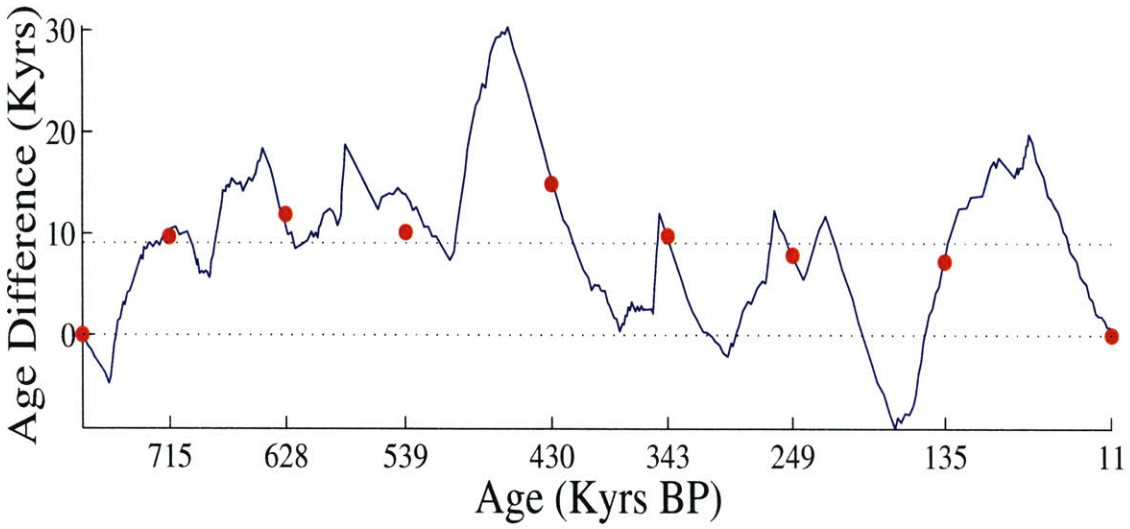

Figure 2-23: The difference between *Shackleton* et al's [1990] orbitally tuned age-model for ODP677 and the depth-tuned age-model. Results from the event tuned age-model, $E^{(9)}$ (dots), and the record tuned age-model, $R^{(63)}$ (solid line), are nearly identical. The depth-tuned age-model indicates the $\delta^{18}O$ record is on average nine KY older than the orbitally-tuned age-model, and that terminations are on average eight KY older.

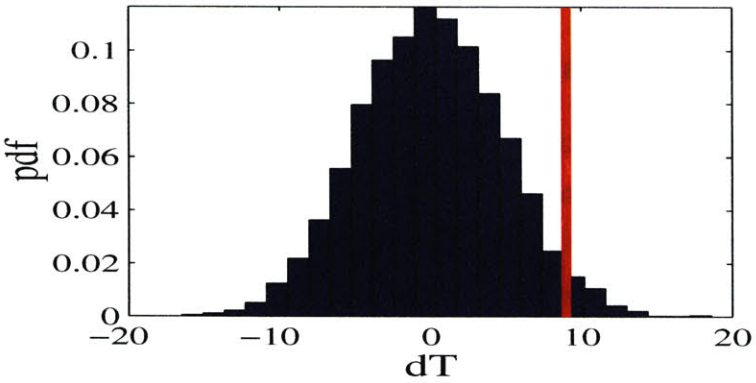

Figure 2-24: The estimated probability density function of mean age deviations. The distribution is very close to Gaussian. The mean observed age deviation between the depth-tuned and orbitally-tuned records (nine KY) is two standard deviations away from the expected value of zero.

cursions between each pair of terminations. The lack of apparent structure in these excursions indicates either large variability in mean accumulation rates independent of the glacial state, or that orbitally-tuned age-models arbitrarily stretch and squeeze time between the terminations.

The time average mean of the difference in age between $R^{(63)}$ and O^{23} is nine KY. The mean deviation from true time for the Brownian bridge process can be expressed as,

$$\bar{dt} = \frac{1}{N-1}\sum_{n=0}^{N}(t'_n - t_n)$$

By running the accumulation rate model 10,000 times, a histogram of mean age deviation is generated and shown in Figure 2-24. The histogram is nearly Gaussian with a standard deviation of 4.5KY; thus indicating that a nine KY mean offset of t' from t would represent a two standard deviation event in terms of random sediment accumulation rate variations. It is possible this significant discrepancy in age-models is due to an unfortunate pattern of sediment accumulation rate variations or to coring artifacts. However, this offset could also result from inaccuracies in the orbital age-model, or some combination of errors between the two age-models. To this end, the origins of the ODP677 age-model are discussed. While this walk down the history of age-models may seem tedious, the story loops back on itself with a relevant and ironic twist.

2.7.1 Orbital-tuning of ODP677

Shackleton et al [1990] orbitally-tuned the ODP677 $\delta^{18}O$ to *Imbrie and Imbrie*'s [1980] ice volume model using the originally estimated parameters. *Imbrie and Imbrie* estimated these parameters using the *Hays* et al. [1976] orbital "TUNE-UP" age-model for the RC11-120 and V28-238 cores. The TUNE-UP model was based on an observed 9 ± 3KY lag of $\delta^{18}O$ relative to obliquity using the 70 to 300KY BP portion of the "ELBOW" age-model [again *Hays* et al, 1976]. This portion of the ELBOW age-model was based on three ACPs: termination two (then radiometrically dated at $127 \pm 6KY$), the stage 5/6 boundary (251KY BP), and the stage 11/12 boundary (440KY BP) with linear accumulation rates between. These last two ACPs were taken from *Shackleton and Opdyke*'s [1972] age-model for core V28-238 , where the age-model was based on constant accumulation rates between the core top and the

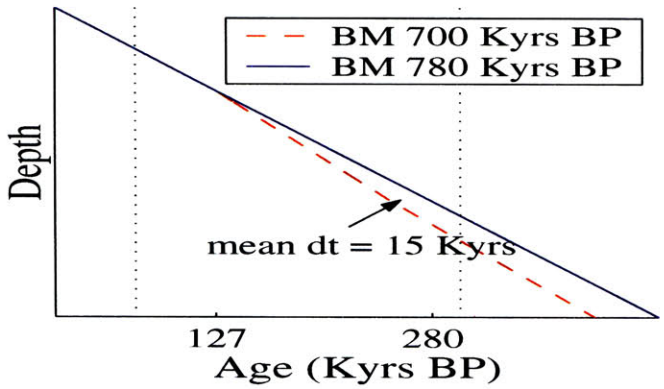

Figure 2-25: A depiction of how an incorrect BM magnetic reversal gives the wrong age-depth relationship under the assumption of constant accumulation rates. With the age at termination two constrained at 127KY BP, but different ages for the stage 5/6 (251 to 276KY BP) and stage 11/12 boundaries (440 to 490KY BP), the average discrepancy in age between 70 and 300KY BP (dotted vertical lines) is 15KY.

B-M reversal estimated to be 700KY old. But an age of 700KY for the B-M is 10% younger than *Shackleton* et al [1990] estimated from ODP677.

The currently accepted age of the B-M is 780KY BP which would change the estimated age of stage 5/6 from 251 to 276 and stage 11/12 from 440 to 490KY BP. Figure 2-25 shows how the average age of the 70 to 300KY BP portion of the ELBOW age model would now increase by fifteen KY. This would fundamentally change the *Hayes* et al estimate of orbital control by making the $\delta^{18}O$ apparently lead obliquity by six KY. The point is that *Shackleton* et al's [1990] success in predicting a more accurate B-M date via orbital-tuning undermines the evidence for a nine KY phase lag of $\delta^{18}O$ behind obliquity.

2.7.2 Radiometric Dates

Table 2.4 shows the depth-tuned, orbitally-tuned, and radiometric constraints on the ages for terminations two through eight. All ages are reported with one standard deviation error estimates. The depth-tuned ages and error estimates were discussed in the previous sections. The orbitally-tuned EOF-1 is from all available orbitally-tuned chronologies including and post-dating ODP677 (see records marked with a "T" in Table 2.1) using $E^{(17)}$. The one standard deviation uncertainties indicates the level of disagreement amongst termination ages within the set of orbitally-tuned

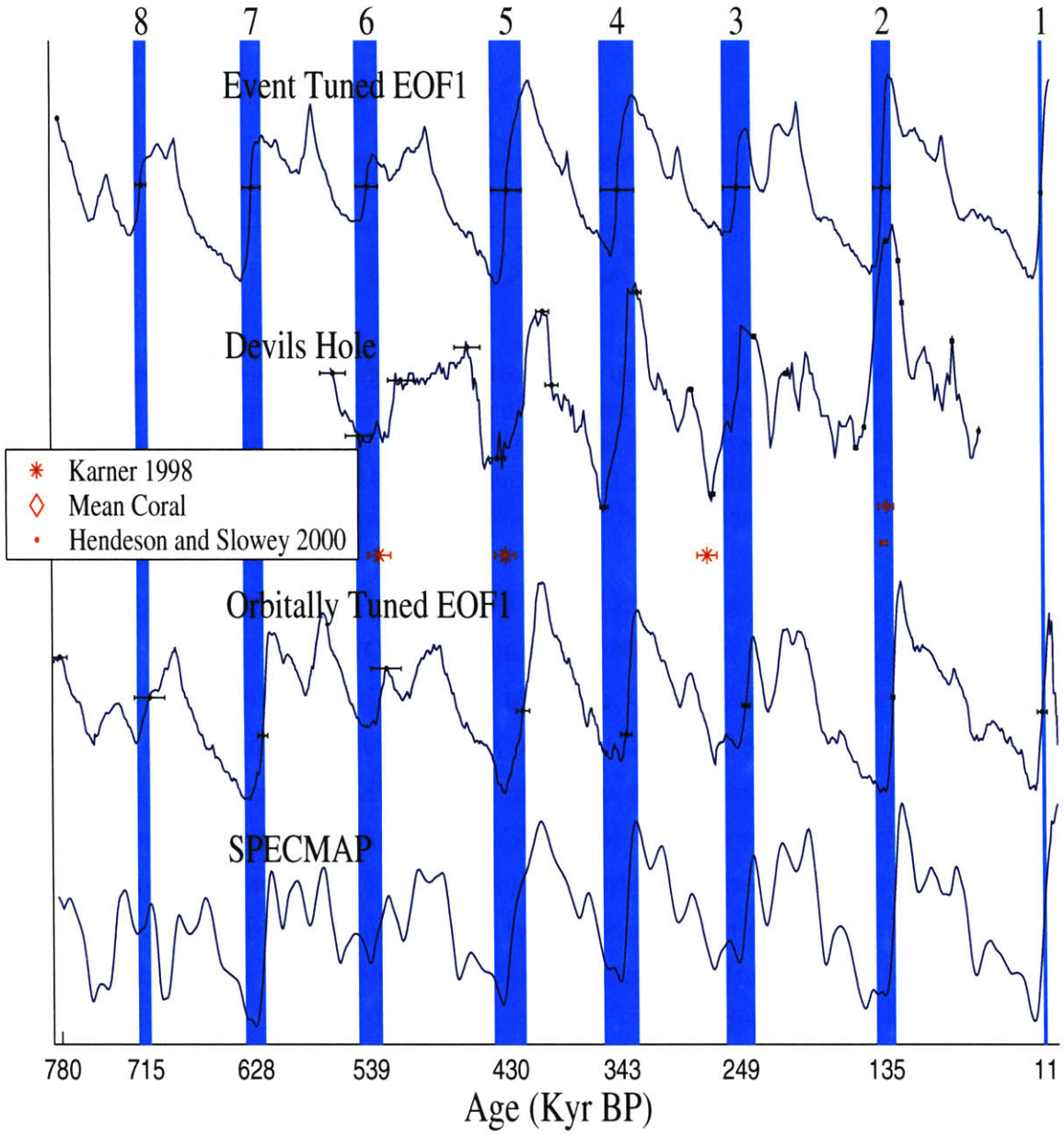

Figure 2-26: EOF-1 from the $E^{(17)}$ age-model (top), the Devils Hole record (inverted relative EOF-1), various radiometric estimates of terminations (see text), the EOF-1 of the ensemble of records for which orbitally-tuned age models are available, and the SPECMAP stack [*Imbrie*, 1984]. Numbers at top indicate each termination. All error bars (horizontal lines) are one standard deviation uncertainties, and the shaded columns correspond to the uncertainties in the $E^{(17)}$ EOF-1. Note the consistently younger termination ages in the orbitally-tuned records.

Termination Number	2	3	4	5	6	7	8
Depth-tuned							
event tuned, $E^{(9)}$	135±7	249±10	343±10	430±10	539±9	628±7	715±5
record tuned, $R^{(63)}$	135±7	249±11	342±13	431±12	543±10	626±7	716±4
Orbitally-tuned							
orbitally-tuned EOF-1	128±2	244±3	338±4	419±5	525±12	622±4	710±12
ODP677 (benthic), 1990	129	243	335	417	531	620	709
SPECMAP, 1984	129±5	245±5	338±5	426±5	530±5	620±5	692±5
Radiometric Dates							
Karner and *Marra*, 1998		274±8		432±8	530±9		
Devils Hole, 1990	140±2	253±2	340±4	417±6	519±10		
Henderson and *Slowey*, 2000	135±3						
Stirling et al, 2001 Hend. Is.			>334±2			>642±18	
Galewsky et al, 1996 Huon Pn.			<348±5				

Corals (T2)	location	type	youngest	mean	oldest
Gallup ^{231}Pa, 2002	Barbados	Acropora palmata	104±1	124±1	136±1
^{230}Th, 2002	Barbados	Acropora palmata	105±1	126±1	136±1
Esat et al, 1999	Huon Pn.	Faviidae (mostly Porites)	106±1	121±1	137±1
submerged	Aladdin's Cave	Faviidae (mostly Porites)	108±1	130±1	134±1
Stirling et al, 1998	W. Australia	Faviidae	116±1	124±1	128±1
drill corals	W. Australia	Faviidea (one Porites)			125,131,135±1
Bard et al, 1990	Barbados	Acropora palmata	101±1	117±1	125±1
Edwards et al, 1987	Barbados	Acropora palmata	122±1		125±1
same paper	Vanuatu	O. crispa and Porites	125±1		130±1
Dodge et al, 1983	Haiti	Acropora palmata	126±6	130±6	132±6
Chappell , 1974	Huon Pn.	Tridacna gigas (giant clam)	116±4	127±3	140±5
Bloom et al, 1974	Huon Pn.	Favi, Hydnophora, Porites	107±3		142±8
Broecker et al, 1968	Barbados	Acropora palmata	111±3	122±2	128±3
mean age			111	124	134

Table 2.4: The depth and orbitally-tuned termination age estimates compared with the available radiometric constraints (top). Coral based radiometric estimates for the age of termination two are listed separately (bottom).

cores. No error estimates are available for ODP677, but the SPECMAP errors were estimated by *Imbrie* et al [1984] to have a constant uncertainty of five KY.

The $^{40}Ar/^{39}Ar$ radiometric dates of *Karner* and *Marra* [1996] are from volcanic horizons interbedded with the sediments of the Tiber and Fosso Galeria River valleys near Rome. A history of the river aggradation is correlated with the deep sea $\delta^{18}O$ record which allows for an estimate of the age of terminations three, five and six. Devils Hole [*Winograd* et al, 1990] is a mass-spectrometric uranium-series dated piece of vein calcite from an aquifer in Nevada. $\delta^{18}O$ measurements show termination like events, though there is a likely offset between changes in sea level and changes in local $\delta^{18}O$ [see *Imbrie* et al, 1993 and *Herbert* et al, 2001]. Nonetheless, the excellent correspondence of features between Devils Hole and the deep sea $\delta^{18}O$ record indicates Devils Hole provides insight into the timing of events which are intimately related to changes in ice volume. *Henderson* and *Slowey* [2000] dated sediment from the Bahamas using a uranium-thorium isochron technique. The advantages of this technique are that the dates can be tied to $\delta^{18}O$ variations in the same sediment after a small correction for sediment mixing. Coral dates for the interglacials following terminations four and seven are included from Henderson Island off of W. Australia [*Stirling* et al, 2001]. Also included is a coral date for the glacial period preceding termination four [*Gallewsky* et al, 1996].

The coral dates listed in Table 2.4 are from Barbados, Haiti, the Huon Peninsula in New Guinea, Australia, and Vanatua (formerly The New Hebrides). Most of the corals grew after the penultimate deglaciation when sea level was near its maximum elevation. Islands with high uplift rates (Barbados, Haiti, and the Huon Peninsula in New Guinea.) may have risen at rates comparable to sea level increase near the end of the penultimate deglaciation, which allows for coral ages corresponding to sealevels within roughly 20% of maximum height [e.g. *Gallup*, 2002]. Other potentially older dates come from submerged corals at Huon Peninsula in Aladdin's Cave [*Esat* et al, 1993], and drill corals from W. Australia [*Stirling* et al, 1998, *Zhu* et al, 1993, and *Whyroll* 1993]. Table 2.4 includes the youngest, mean, and oldest coral dates judged reliable by each cited author. Mean ages are omitted when only two or three radiometric dates are available. *Gallup*'s [2002] ^{231}Pa and ^{230}Th dates for the same collection of samples are reported in separate rows. Because the drill corals probably correspond to older portions of the last interglacial, the youngest, mean, and oldest dates are all reported under the oldest column. Only dates ranging between 100

and 150KY BP are included as other dates almost certainly do not correspond to the interval encompassing termination two. All errors are reported in units of one standard deviation and, when reported by the original reference, the errors include uncertainties in the decay constants.

In all cases the corals are assumed to have grown after the deglaciation and thus give a younger bound on the age of termination two. A discrepancy in interpretation can arise if the mean or the oldest coral age is used to constrain termination two. According to the depth-tuned and orbitally-tuned chronologies, the midpoint of termination two occurs five ($E^{(17)}$) and six KY (SPECMAP) prior to stage 5.5 (the $\delta^{18}O$ maxima directly following termination two). If the mean coral age (approximately 124 KY BP) is used to estimate the age of stage 5.5, termination two receives an age of 130 KY BP and accords with the orbitally tuned age estimates. However, it is possible the mean coral ages erroneously include corals from stages 5.3 or 5.1 (the next two youngest $\delta^{18}O$ maxima) or are weighted toward the younger portions of stage 5.5. If instead the oldest reliably dated corals are used to constrain the age of termination two, a mean age of 134 KY BP is calculated which corresponds to the depth tuned age-model. The difficulty with this constraint is that diagenetic alteration of the corals can bias Uranium series dating of corals toward artificially old ages. Culling the oldest ages from numerous records may produce an artificially old age estimate well outside the bounds otherwise indicated by the small reported radiometric age uncertainties.

Termination Two The depth-tuned age of termination two (T2) (135 ± 7KY BP from $E^{(9,17)}$) is one standard deviation older than the mean orbitally-tuned age (128 ± 2KY BP from orbital EOF-1). The ambiguity in using the mean or older coral dates was discussed above. However, there is some strong evidence that the age of termination two is older than the orbital estimates. *Henderson and Slowey*'s direct bulk sediment date yields a date of 135 ± 3 KY BP for termination two and obviates discussion of coral termination age offsets. This age estimate is two standard deviations older than the orbital date and coincides with the depth-tuned date. Another notable study is *Gallup* [2000] wherein both ^{231}Pa and ^{230}Th Acropora palmata coral dates constrain termination two to occur before 136 ± 1KY BP. Considering northern hemisphere summer insolation peaks at 126KY BP, Milankovitch theory seems inconsistent with the available radiometric constraints on termination two. Finally the Devils Hole record indicates dramatic $\delta^{18}O$ isotopic changes beginning as early as

140 ± 2KY BP. Under the weakest possible assumption, Devils Hole is interpreted as a local climate change record and indicates that Milankovitch type processes cannot fully account for all long term climate changes. Using a stronger assumption, Devils Hole indicates the earth began warming well prior to increases in insolation at 65 North and contradicts the Milankovitch theory.

Terminations Three and Four Both depth-tuned ages ($249 \pm 11, 343 \pm 13$) are five KY older than the orbital counterparts ($244 \pm 3, 338 \pm 4$). Devils Hole leads the depth-tuned ages by four KY for T3 and lags by three KY for T4 ($253 \pm 2, 340 \pm 4$), but is older than both orbital ages. *Karner* and *Marra* [1998] indicate a significantly older date for T3 at 274 ± 8. The coral bounds on the maximum and minimum dates for T4 do not strongly discriminate between the orbital and depth-tuned age. If the mean age of the corals (341KY BP) is used as an estimate for the age of T4, the date is somewhat closer to the depth-tuned estimate. In all, the available radiometric dates for T3 and T4 are more consistent with the depth-tuned ages.

Terminations Five and Six There are large eleven and fourteen KY leads of the depth-tuned ages ($430 \pm 12, 539 \pm 9$) over the orbital ages ($419 \pm 5, 525 \pm 12$). The orbitally-tuned age-models are largely predicated upon the same set of assumptions so the standard deviation in the ages of orbital EOF-1 are an indication of the ability to consistently apply those assumption. T6 is poorly developed and the uncertainty of 12KY results from difficulty in consistently matching a precessional cycle to the T6 features. For T5 *Karner and Marra*'s date (438 ± 8) coincides with the depth-tuned age while their T6 date (530 ± 9) is within one standard deviation of both the depth and orbitally-tuned ages. The Devils Hole record has dates ($417 \pm 6, 519 \pm 10$) which are slightly younger than the orbital times. The large uncertainties in both orbital and depth tuned ages makes it difficult to make an inference regarding these terminations.

Terminations Seven and Eight Depth-tuned ages ($628 \pm 7, 715 \pm 4$) maintain a five KY lead over the orbital ages ($633 \pm 4, 710 \pm 12$). The proximity of the B-M reversal decreases the error associated with the depth-tuned ages and makes the lead relationship more credible. Only one radiometrically dated coral is available [*Stirling* et al, 2001] which has a large error associated with it (642 ± 18). This estimate marginally lends support for an older T7 age. Also, the error in the SPECMAP B-M

age (approximately 50KY too young) is evident in that its T8 age is 18KY younger than the other orbitally-tuned estimates.

The radiometric dates associated with the terminations offer good support in favor of the depth-tuned age model. The nine KY lag of the orbital ages behind the depth-tuned ages can be traced back to an assumption regarding the phasing of the earth's response to obliquity[7]. In the absence of evidence for such a phase lag, and with the support of the available radiometric dates, it is concluded that the depth-tuned age-models provide a more accurate timescale of glaciation.

All of the age-models developed in Chapter 2 are devoid of any orbital assumptions, are based upon at least twice as many age-depth relationships as any previous study (*Raymo* [1997] used 11) and, unlike any previous linear age-depth model, are corrected for the effects of compaction. Thus, these depth-tuned age-models offer a uniquely clear vantage point from which to evaluate the orbital theory of climate change. Since the $E^{(17)}$ age-model seems to offer the best combination of accuracy and simplicity, it will be relied upon for all subsequent analysis.

[7]Other assumptions about precessional or insolation lags are tantamount to this obliquity assumption.

Chapter 3

Non-Linear Responses to Orbital Forcing.

The paucity of 100KY energy in insolation variations [see *Berger and Loutre*, 1991] necessitates a non-linearity in any model which seeks to associate the glacial cycle over the last 700KY with insolation variations [*Imbrie*, 1993]. The distinct asymmetry in the rates of glacial accumulation and melting indicates a further non-linearity in the climate system. *Imbrie and Imbrie* [1990] account for this non-linear behavior by postulating a climate model which demodulates the low frequency precession envelope by prescribing a rapid melt rate relative to accumulation. For the parameters estimated by *Imbrie and Imbrie*, the cycle of glaciation is controlled by the magnitude of N. Hemisphere summer insolation and thus falls under the aegis of Milankovitch theory.

There are a number of features of the observed paleo-climatic record, to include non-Milankovitch spectral peaks, which Milankovitch theory does not account for (for a review see *Elkibbi and Rial*, [2001]). *Nobes* et al [1991] apply a suite of spectral analysis procedures to the physical property data at ODP sites 699, 701, and 704 using linear age-depth relationships and find evidence for the presence of a variety of Milankovitch combination tones and harmonics. Using a wavelet analysis *Bolton and Maasch* [1995] report the presence of variations with a 75KY period in the orbitally tuned $\delta^{18}O$ records from ODP sites 677 and 806. *Mix* et al [1995] find evidence of a 1/30KY cycle in the $\delta^{13}C$ and $\delta^{18}O$ time series from ODP 846 using a tuned age-model. Analyzing the Vostok ice-core (between 0 and 160KY BP), *Yiou* et al [1991] note some spectral energy concentrated at frequencies of 1/60 and 1/30KY in both

the temperature proxy and CO_2 time series. Here the spectral analysis of Vostok is extended to the full length of the ice-core (400KY), which serves to strengthen the inferred existence of spectral peaks which are not linearly related to Milankovitch forcing.

Notwithstanding the isolated reports of non-Milankovitch spectral peaks, orbital-tuning typically seeks to maximize the variance in the Milankovitch spectral bands (i.e. obliquity and precession). As an example, in generating an orbital age-model for DSDP607, *Ruddiman* et al [1989] note excessive power at the 1/70, 1/54, and 1/30KY bands. They state the age-model was thus adjusted to re-distribute the "anomalous" energy into the Milankovitch bands. It seems the use of orbitally tuned age-models in formulating design criteria and in evaluating low order climate models promotes the self-selection of Milankovitch behavior [e.g. *Berger* 1978, *Lindzen* 1986, *Imbrie and Imbrie* 1990, *Imbrie* 1993, *Liu* 1998, and *Paillard* 1998] The influence of age-models on the orbital interpretation of the paleo record is further demonstrated by re-tuning *Imbrie and Imbrie*'s ice-volume model using a non-orbital age-model. A number of simple climate model studies explicitly evaluate linear age-depth $\delta^{18}O$ behavior [e.g. *Rial* 1999, *Muller and MacDonald* 2000, and *Wunsch* 2002], but only use a single age-depth relationship and thus have an expected age uncertainty of roughly 30KY (see Chapter 2). While this degree of uncertainty is sufficient to allow some analysis of low frequency variations (roughly less than 1/70KY), it is not expected to adequately resolve higher frequency variations.

Here the $E^{(17)}$ age-model, with an expected uncertainty of 10KY and devoid of all orbital assumptions, is used to evaluate 26 $\delta^{18}O$ records extending from the present to the B-M magnetic reversal (780KY BP). Spectral and bi-coherence analysis of the $\delta^{18}O$ records indicates a strong non-linear climatic response to orbital forcing. This same non-linear spectral relationship is found in the Vostok temperature and CO_2 proxies. The clues drawn from this analysis of the $\delta^{18}O$ record are incorporated into a simple obliquity based threshold model of glaciation which reproduces the observed timing, amplitude, and non-linear features of the $\delta^{18}O$ record. The ability of this simple obliquity model to capture the timing and character of glaciation indicates the physical plausibility of both the $E^{(17)}$ depth-tuned age-model and the observed non-linear climatic response to orbital forcing.

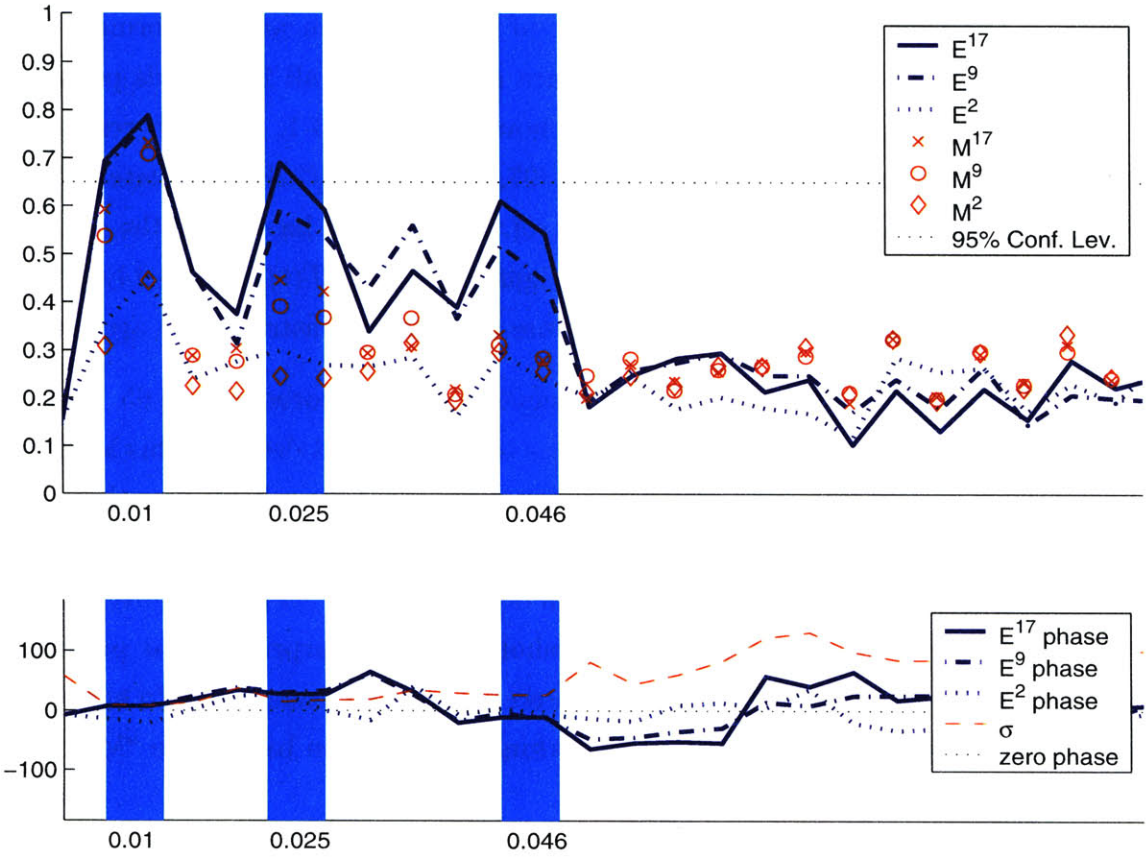

Figure 3-1: The mean coherence (top) and phase (bottom) of the 26 records pinned to $E^{(2,9,17)}$. A Monte Carlo jitter simulation using known signals (marks $M^{(2,9,17)}$) accompanies each coherence estimate. The horizontal black line (top) indicates the 95% confidence level, and (bottom) the zero phase line. The dashed line (bottom) indicates the standard deviation of the 26 separate coherence estimates; note how within the orbital bands the discrepancy in phasing is small.

3.1 Depth-tuned $\delta^{18}O$ Record

3.1.1 Spectral Description

A coherency estimate of the 26 $\delta^{18}O$ records is made with a test signal composed of

$$T(t) = \sin(\frac{2\pi t}{95} - \phi) + \theta(t) + p(t) \tag{3.1}$$

θ is obliquity and p is precession as calculated by *Berger and Loutre* [1992] . The sinusoidal term represents the quasi-100KY type energy where 1/95KY is the highest frequency of the eccentricity triplet which has a phase of $\phi = 47^o$. The origin of the

100KY band is uncertain (see section 3.3.2), and an eccentricity-like harmonic is only used as a reference curve. Each component of $T(t)$ is zero mean and normalized to unit standard deviation. The mean coherence and phase of all 26 records pinned to the $E^{(2,9,17)}$ age-models (see Chapter 2) is shown in Figure 3-1. The coherence with the test signal in each of the test bands (1/97, 1/41, and 1/22KY indicated by the shaded bars) increases with greater age control. This did not have to be the case. An increased coherency indicates that both a signal similar to $T(t)$ is probably present and that increasing the number of ACPs more accurately constrains the age-model.

The 95% confidence level for this coherency estimation procedure is 0.65. Averaging multiple independent coherence estimates together would decrease this level, but the event tuning process and large covariance of the $\delta^{18}O$ records renders these estimates largely dependent. *Moore* and *Thomson* [1991] show that higher frequencies are more susceptible to the effects of age-model errors, thus while obliquity and the 100KY band cross the 95% confidence threshold, it is not surprising that precession does not. It is unknown whether this low precessional coherence is due to age-model jitter or to substantial incoherent energy within the precession band. The "M" marks on Figure 3-1 are discussed in section 3.1.1.

The relative phase estimate between $\delta^{18}O$ and T(t) is shown on the bottom of Figure 3-1. A positive phase indicates $\delta^{18}O$ lags behind T(t), and the standard deviation between the multiple coherency estimates for $E^{(17)}$ is indicated by the dashed curve. The standard deviation in phase estimates is small for the frequencies with high coherence, but grows away from these bands. This indicates that the event tuning procedure pinned T(t) like signals in the $\delta^{18}O$ records to a common age-model. In so much as the earth responds linearly to a T(t) like forcing, a constant phase is expected. A trend toward greater phase delay is observed with increasing frequency, but this observations needs to be qualified. If a non-linearity is responsible for the 100KY cycle, depending on the non-linearity employed, any phase between $\delta^{18}O$ and the 100KY band is attainable. The phase of precession used here [following *Berger* and *Loutre*, 1992] is usually defined as the angle between perihelion and the spring equinox. This definition makes the $\delta^{18}O$ records lead precession by 10^o or about 0.5KY. By changing the definition of precession's phase, the relative phasing of the $\delta^{18}O$ response would correspondingly change. Only obliquity has a strictly definable phase, and thus phase relationship, with $\delta^{18}O$. For the $E^{(2,9,17)}$ age-models the mean phase lag with respect to the obliquity band is 28 ± 2^o or a time lag of three KY.

As previously noted, the obliquity lag with the orbitally-tuned age-models is approximately nine KY, giving a six KY discrepancy between orbital and depth-tuning lags. That the discrepancy in termination dates is eight KY and not six KY is another example of how adjustments to an age-model strongly modify the spectra and phase of a record.

Figure 3-2 shows the mean power density spectrum (PSD) of each $\delta^{18}O$ record using $E^{(2,9,17)}$. Paralleling the increase in coherence, the energy in the 100KY, obliquity, and precession bands each increase with greater age control. The 95% confidence interval is shown as a thick vertical bar in the upper right of the plot. For $E^{(17)}$ the 1/100, 1/41, and another peak at 1/70KY (discussed later) all exceed the 95% confidence level. Again, higher frequencies are expected to be more susceptible to jitter, and it is difficult to discern the variance truly concentrated within the precession band. The percent variance accounted for by each spectral peak is also indicated in Figure 3-2. At frequencies above the orbital bands the spectrum falls off with a -2 power law relationship, and the majority of the variance is accounted for by the low frequency component of the record (less than 1/70KY). Later, the time derivative of ice-volume is investigated which de-emphasizes the low frequency content of the spectrum.

3.1.2 Estimating the True Spectra

A conundrum exists in estimating the energy within the orbital bands of the $\delta^{18}O$ spectrum. A depth-tuned age-model is jittered, which tends to diminish energy in spectral peaks, while an orbitally-tuned age-model tends to maximize the energy within the orbital bands. Another complication is that errors in the age-model smear spectral energy across all frequencies (e.g. some energy residing in the precession band truly belongs within the obliquity band), thus the distribution of energy at each component needs to be estimated simultaneously. A technique which seeks an unbiased estimate of the $\delta^{18}O$ energy truly related to orbital variations is presented here, and is termed *de-jittering.*

The true $\delta^{18}O$ spectrum is defined as the mean $\delta^{18}O$ spectrum of the 26 records included in this study using a perfect age-model. Effects due to bioturbation are neglected. It is assumed that the true spectrum can be generated from a linear combination

$$S(t) = \sqrt{v_1}H_{95}(t) + \sqrt{v_2}\theta(t) + \sqrt{v_3}p(t) + \sqrt{v_4}N \tag{3.2}$$

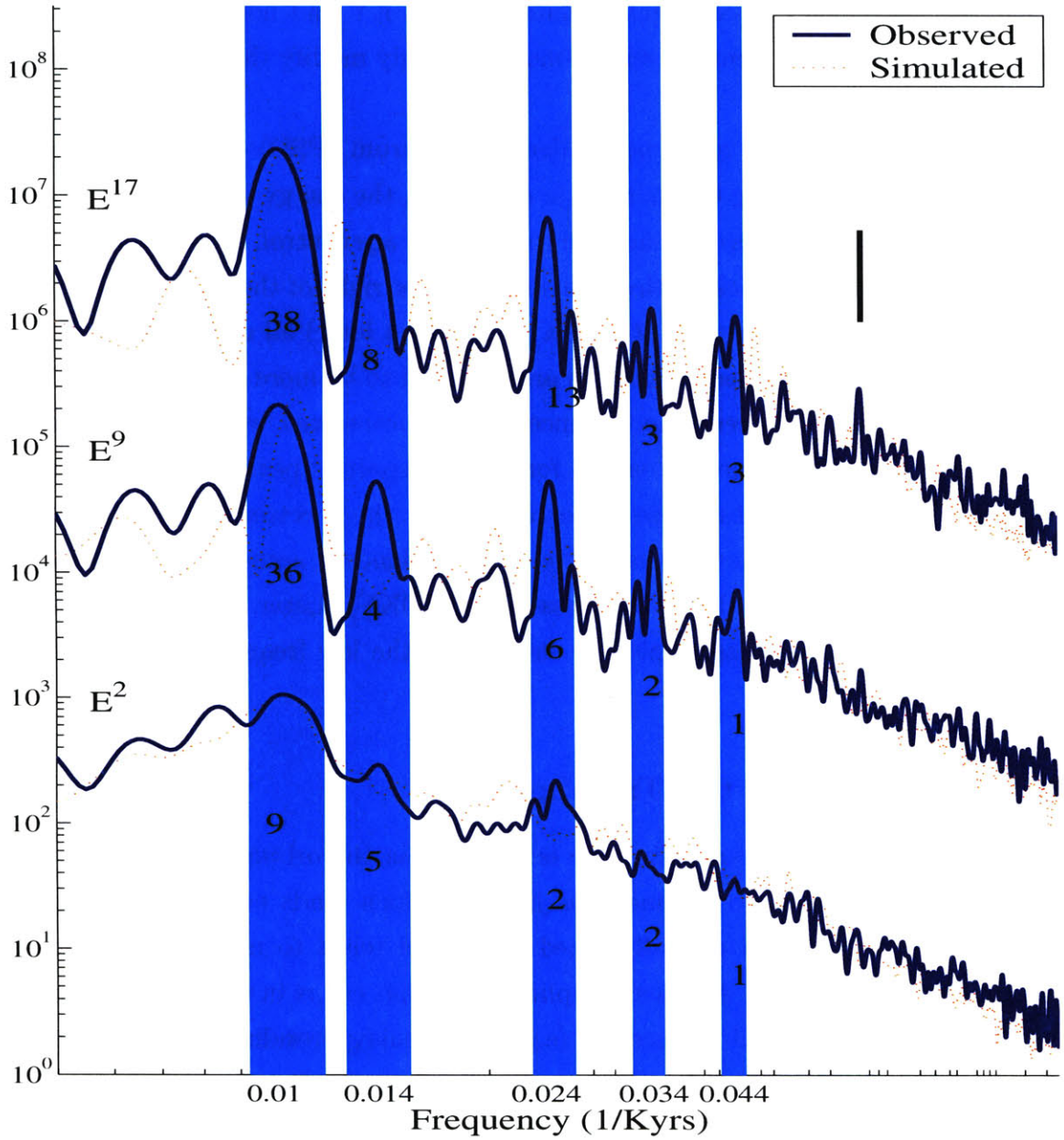

Figure 3-2: The mean expected and observed $\delta^{18}O$ power densities for the $E^{(2,9,17)}$ timescales. The numbers within the shaded bands indicate the mean percent variance explained by that spectral feature. The shaded bands are centered from left to right on 1/100, 1/70, 1/41 (obliquity), 1/27, and 1/22KY (precession). For $E^{(17)}$ the 1/100, 1/70, and 1/41 spectral peaks are above the 95% confidence level. The y-axis units are arbitrary and records are separated by two orders of magnitude.

composed of a 1/95KY harmonic, obliquity, precession, and red noise defined by Eq 2.2; all of which are normalized to zero-mean and unit variance. The v_n terms indicate the percent variance attributed to each component, and the sum of v_n is one. By jittering $S(t)$ in the manner estimated for $\delta^{18}O$ records ($J = .3$), a signal S(t') is generated whose spectral energy distribution may be compared to the observed $\delta^{18}O$ records. The metric used to compare the spectra is

$$r = \frac{\sum_f |\hat{S}||\hat{D}|}{\sqrt{\sum_f |\hat{S}|^2}\sqrt{\sum_t |\hat{D}|^2}} \tag{3.3}$$

where $|\hat{S}|$ is the mean absolute value of the Fourier transform of 26 realization of S(t'), and $|\hat{D}|$ is the mean absolute value of the Fourier transform of the $\delta^{18}O$ records. The absolute values of the Fourier transforms are employed to set all frequencies to zero phase. The r metric then measures the cross-correlation between the mean periodograms of S and $\delta^{18}O$.

$S(t')$ is generated with t' corresponding to three levels of age control: unconstrained between the end points ($E^{(2)}$), pinned at nine ACPs, and pinned at 17 ACPs ($E^{(17)}$); each with an uncertainty as shown in Figure 2-20. The r^2 metric between S(t') and $\delta^{18}O$ is calculated for each of these three age control levels, and the mean value ($\bar{r}^2$) is used to evaluate the success of the v_n distribution of variance. A simulated annealing method is used to find v_n which maximizes $\bar{r}^2$. Because the $\bar{r}^2$ value depends not only on v_n but also the nuances of the jitter and the red noise in each realization of $S(t')$, this process is repeated 50 times and the mean value of v_n is reported along with the standard deviation of the ensemble of estimates

$$\begin{aligned} \text{95KY } v_1 &= 40 \pm 11\% \\ \text{precession } v_2 &= 10 \pm 6\% \\ \text{obliquity } v_3 &= 13 \pm 7\% \\ \text{red noise } v_4 &= 37 \pm 11\% \end{aligned}$$

The large standard deviation in the estimates of v reflects the strong influence jitter exerts on the periodogram of $S(t')$. If each estimate of the variance is considered independent and a Gaussian distribution is assumed, the standard deviation of the mean would decrease by a factor of 7. A mean PSD of 26 S(t') realizations with this partition of variance is shown in Figure 3-2 (dotted line) for jitter corresponding

to each of the three event age-models. Most of the major features of the spectrum are reproduced to include a -2 power law at frequencies greater than 1/40KY and emerging spectral peaks at the 100KY, obliquity, and precessional bands. Two other spectral peaks located at 1/70 and 1/27KY, however, are not reproduced. This is not surprising considering S(t) is a linear combination of functions with negligible energy in these bands. None the less the peak at 1/70KY in the $\delta^{18}O$ records is above the 95% confidence, casting some suspicion on the adequacy of S(t) and thus the Milankovitch theory.

The mean coherency between S(t) and T(t) from Eq 3.1 is also shown in Figure 3-1. As in the coherence estimate with the $\delta^{18}O$, the coherence in the low frequency 1/100KY band is strong for the simulated $E^{(9,17)}$ age control and decreases with the higher frequency obliquity and precessional bands. Outside of the these bands, coherency is uniformly low. The simulated obliquity and precession coherencies are smaller than the $\delta^{18}O$ coherencies by about 0.1. This deviation is about one standard deviation for the variations in simulated coherency. That both obliquity and precession are underestimated could indicate inadequacies in the jitter simulation or inadequacies in the representation of S(t).

3.1.3 The Time Rate of Change

The time rate of change of $\delta^{18}O$ may be a more useful physical parameter from which to deduce the physical characteristics of climate. To extract the most representative $\delta^{18}O$ variations, the leading EOF is calculated of the 26 $\delta^{18}O$ records pinned to the $E^{(17)}$ age-model (EOF-1). The PSD of the discrete derivative of EOF-1, $\triangle$EOF-1, is shown in Figure 3-4, and is equivalent to multiplying the PSD of EOF-1 by f^2. The background noise in the interval between 1/110 and 1/20KY is now a white spectrum while outside of this region the energy falls off rapidly. Figure 3-2 shows a minus two power law for the mean $\delta^{18}O$ PSD at frequencies above 1/40KY, and thus taking the derivative would produce white noise at the higher frequencies. The spectrum of $\triangle$EOF-1 falls away above the 1/40KY frequencies because there is little co-variance between the $\delta^{18}O$ records at high frequencies. Like the spectrum of the coherent $\delta^{18}O$ energy (see section 2.3.1), EOF-1 has a steeper power law relationship at high frequencies (approximately -4).

The spectral peaks at 1/100, 1/70, 1/41, 1/29, and 1/23KY are all above the 95% significance level (the peaks in EOF-1 are equally significant as the signal to noise

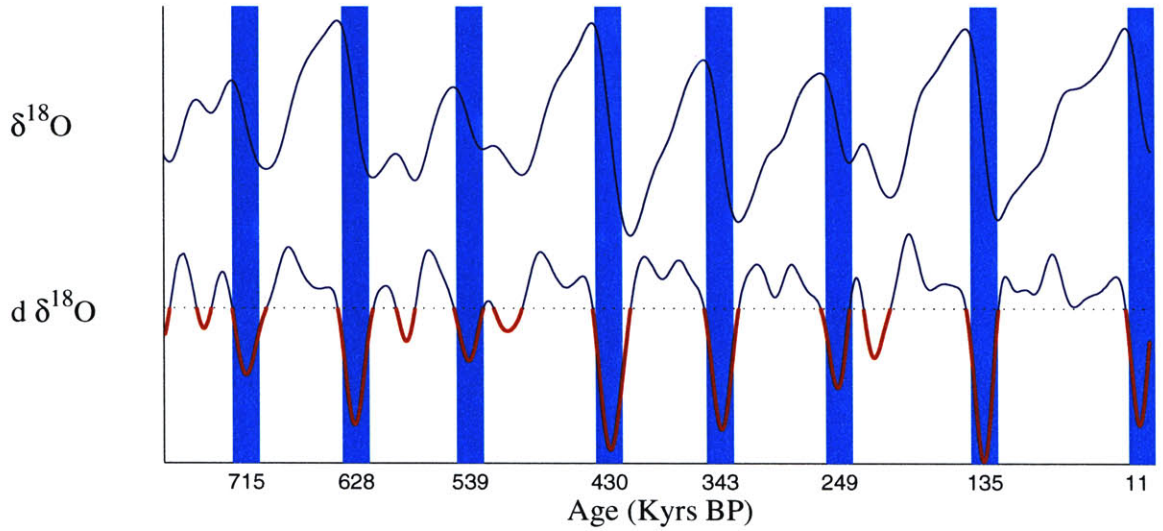

Figure 3-3: The smoothed EOF-1 signal plotted such that ice volume increases upward (top), and the derivative of the smoothed EOF-1 (bottom). The horizontal dotted line indicates zero rate of change in EOF-1. Note that melting events (below the dotted line) have a large amplitude and brief duration relative to the accumulation periods. Shaded columns correspond to the terminations.

ratio within each frequency band is not altered by taking the derivative). Apparently, taking the 1st EOF of the ensemble of $\delta^{18}O$ records enhances the energy within a subset of spectral bands. Indeed, the peaks above the 95% significance level now account for 60% of the observed variance in $\triangle$EOF-1 (note the obliquity band dominates) and 75% of the variance in EOF-1. The spectral peaks at 1/29 and 1/70KY may be manifestations of those previously alluded to by *Bolton and Maasch* [1995], *Mix* et al [1995], and *Yiou* et al [1991] (see the introduction to this chapter).

Figure 3-3 shows $\triangle$EOF-1 in the time domain after smoothing by convolution with a 25KY Hanning window. Assuming EOF-1 approximates a global ice volume record, the changes in ice volume can be approximated as cycling through three states of accumulation (large positive excursions), steady (small derivative), and melting (large negative excursions). The cycling through these states can be thought of as the time derivative of the four modes identified by *Imbrie* et al [1993] which are preglacial, glacial, deglacial, and interglacial. Each of the glacial events estimated to have an approximately 80KY interval have double humps in accumulation while the longer 120KY cycles have three humps, which corresponds to the duration of the same number of quantized obliquity cycles. In keeping with the saw tooth nature of $\delta^{18}O$,

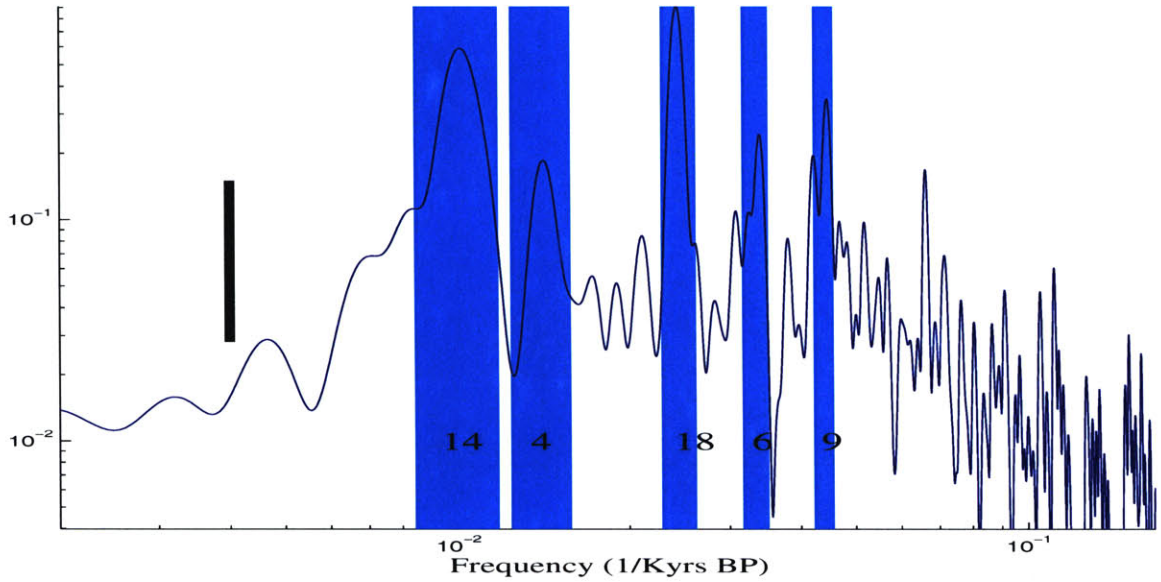

Figure 3-4: The PSD of the derivative of the un-smoothed EOF-1. The 1/100, 1/70, 1/41, 1/29, and 1/22KY frequency bands (shaded columns) each have peaks above the 95% confidence level (indicated by the thick vertical bar). Together these peaks account for more than 60% of the variance in the time rate of change of EOF-1. Note the spectral energy falls away outside of the orbital bands.

the melting state has a larger amplitude and shorter duration than the accumulation phase. While the duration of melting is roughly constant at 10KY there are large variation in the rate of melting between individual events. In section 3.3 the behavior of EOF-1 is reproduced with a simple glacial model.

3.2 Non-linear Coupling of Obliquity and the quasi-100KY Band

3.2.1 Bi-linear Coupling

A simple relationship between the significant PSD peaks of EOF-1 is

$$f(n) = \frac{1}{41} + \frac{n}{100} \qquad n = \{-1, 0, 1, 2\} \tag{3.4}$$

The appearance of 1/100KY combination tones with the obliquity frequency suggests that variations in obliquity may be non-linearly associated with driving these other frequencies.

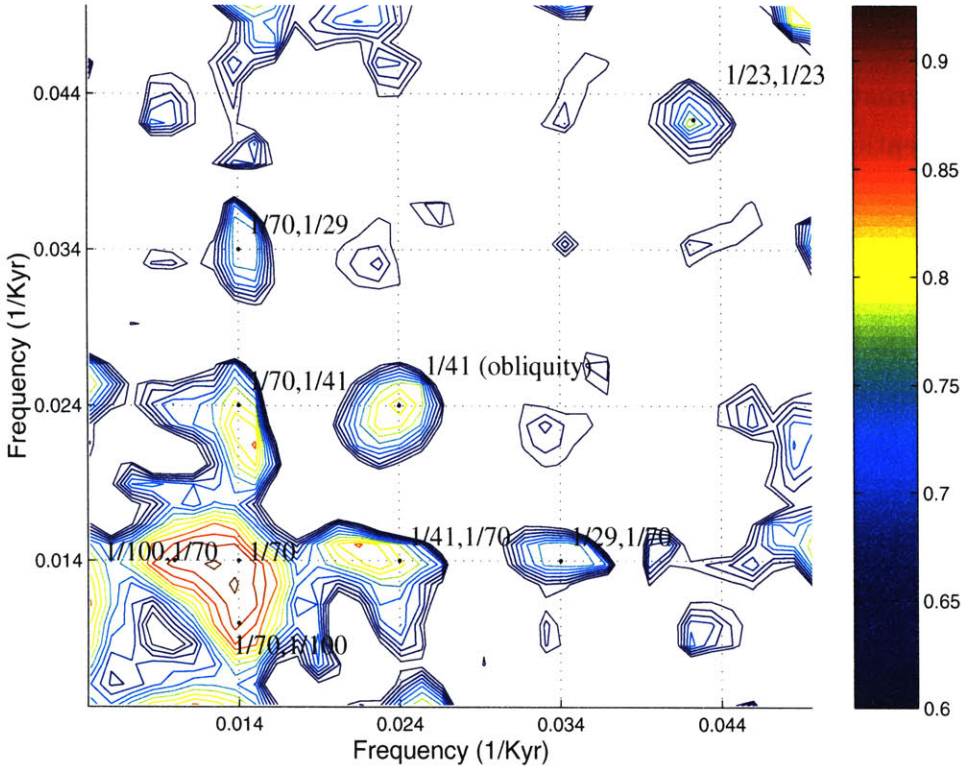

Figure 3-5: The auto-bicoherence of EOF-1 from the $E^{(17)}$ age model. The figure is plotted in frequency vs. frequency and is symmetric about the diagonal. The tick marks are located at $f = f_{obliquity} + n/100$, $n = \{-1, 0, 1, 2\}$, and the frequency pairs of interesting peaks in bicoherency are indicated on the plot. Only bicoherencies greater than 0.6 are contoured.

A bispectral test for second order non-linearities was presented by *Hasselmann* et al [1963]. Estimation of auto-bicoherence is an adaption of the bispectral method to test for coherent phase relationships produced by quadratic coupling of harmonics. The 95% confidence level for this test in the presence of red noise is 0.9 for $f_k = f_l$ and 0.8 for $f_k \neq f_l$ where f_k and f_l represent the two frequency axis. An explanation of the auto-bicoherence technique as implemented here is included in Appendix B. Figure 3-5 shows the auto-bicoherence of EOF-1 using the $E^{(17)}$ age-model. Significant bicoherencies exist at period couplets of $\{70, 70\}$, $\{70, 100\}$, and $\{70, 41\}$. Coherence maxima below the 95% confidence level appear at periods $\{41, 41\}$ and $\{29, 70\}$. It is interesting to note that obliquity is bicoherent with itself indicating the variance observed in the precession band could be due to an over-tone of obliquity ($1/41 + /141 = 1/20.5$). At every combination of the frequencies represented by f(n) there

exists some bicoherent feature above the .6 level. This strongly indicates that the spectral peaks at $f(n)$ are non-linearly coupled.

An alternative presentation of the relationship between the spectral peaks in EOF - 1 calls attention to the precession band

$$f(n) = \frac{1}{23} + \frac{n}{100} \qquad\qquad n = \{-3, -2, -1, 0\}$$

But since the obliquity band has substantially more energy, seems to be quantized in the accumulation intervals of $\triangle$EOF-1, and is strongly auto-bicoherent, the focus will remain on Eq 3.4.

3.2.2 Non-linearities in the Vostok Spectra

The Vostok ice-core records atmospheric trace gas and ice composition variations in Antarctica over the last 400KY [*Petit* et al, 1999]. *Yiou* et al [1991] note the presence of combination Milankovitch tones in the temperature proxy (derived from a linear relationship between δD and $\delta^{18}O_{atm}$) and CO_2 records, though at the time Vostok measurements only extended to 160KY BP. Figure 3-6 shows the temperature proxy and CO_2 PSDs from the longer 400KY Vostok record by Petit et al [1999] using their GT4 age-model. GT4 was minimally orbitally-tuned by fitting a glaciological age-depth model to the orbital ages of marine isotopic stages 5.4 (110KY BP) and stage 11.2.4 (390KY BP). The two orbital ACPs preclude GT4 from yielding an independent estimate of the timing of climatic events. However, the duration of these events is only mildly orbitally constrained and, since spectra are (linear) time-shift invariant [see *Bracewell*, 2000], it is interesting to compare the spectral estimate of the Vostok proxies against the $E^{(17)}$ EOF-1 PSD.

Significant spectral peaks are apparent in both time-series at the $f(n)$ frequencies where the relationship seems to extend to a higher frequency, giving $n = \{-1, 0, 1, 2, 3\}$. The distribution of variance is similar between CO_2, temperature, and EOF-1 in that the 1/100KY peak dominates, obliquity follows, and the combination tones are the weakest. For each PSD, the 1/100KY and $f(n)$ bands account for approximately 60% of the total variance. That two independently derived age-models applied to diverse climate proxies both indicate the presence of combination tones between obliquity and the 1/100KY band lends credence to the climatic significance of Eq 3.4.

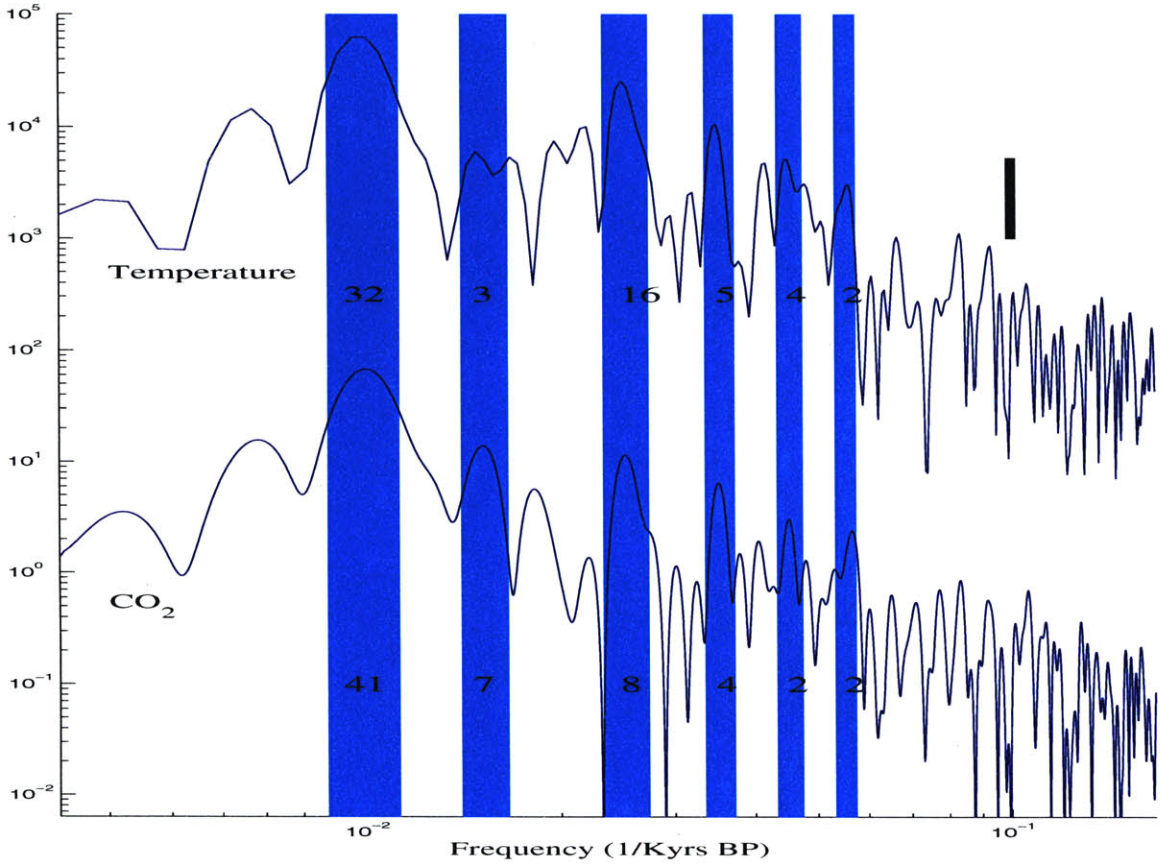

Figure 3-6: The power density spectra of the temperature proxy and CO_2 time series from Vostok over the last 400KY. The shaded bands are at 1/100KY and $f(n) = 1/41 + n/100$ for $n = \{-1, 0, 1, 2, 3\}$. Note the similarity with the PSD of $E^{(17)}$ in Figure 3-2. The 95% confidence interval is indicated by the thick vertical bar, and records are off-set by three orders of magnitude.

3.3 Speculation on the quasi-100KY Glacial Cycle

3.3.1 Re-tuning *Imbrie* and *Imbrie*'s Ice-Volume Model

It is interesting to reverse engineer ODP677's tuning process as it demonstrates how strongly an age-model influences the apparent physical relationship between orbital change and the earth's climatic response. ODP677 was tuned to *Imbrie* and *Imbrie*'s [1980] ice volume model which is a non-linear set of equations with four adjustable parameters. The insolation forcing function has two-adjustable parameters

$$q = \theta + \alpha e \sin(w - \phi) \tag{3.5}$$

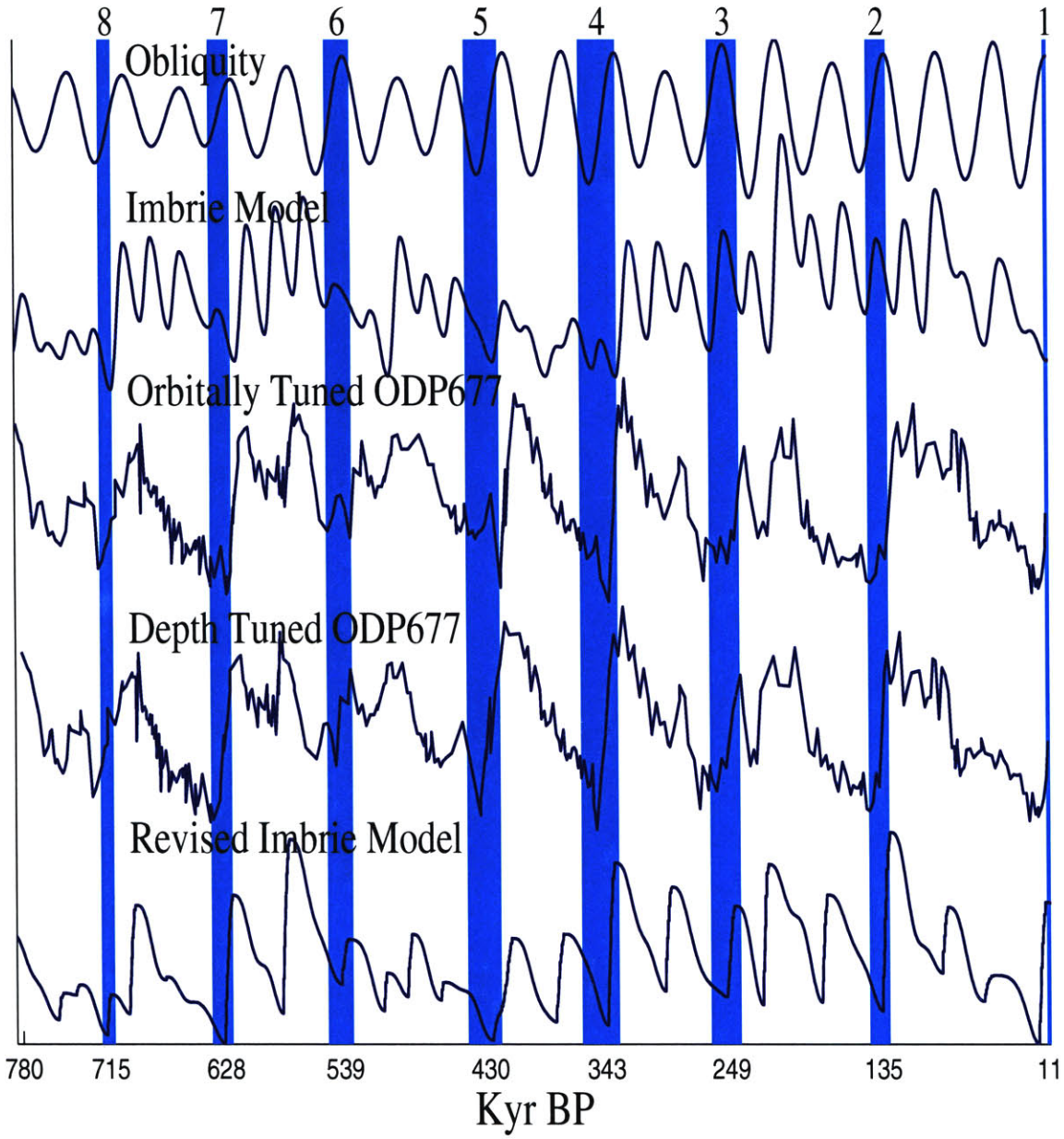

Figure 3-7: The normalized obliquity parameter is plotted above the output of *Imbrie and Imbrie*'s ice volume model using the original 1980 parameter estimates. Note the nine KY phase lag of the model behind obliquity. *Shackleton* et al tuned ODP677 to this model ($r^2 = 0.24$), again imposing the nine KY phase lag behind obliquity. Tuning *Imbrie*'s ice volume model to the depth-tuned ODP677 record ($r^2 = 0.28$) increases the role of obliquity forcing and decreases the melting time-constant. The vertical shaded bars are the $E^{(9)}$ termination ages plus and minus one standard deviation, and at top are the termination numbers.

The parameter α adjusts the relative ratio of obliquity (θ) to precession ($e\sin\{w-\phi\}$) and is linked to latitude [small α corresponds to high latitude]. The phase angle, ϕ, controls the phase of precession and is linked to the season of the the insolation curve. Both obliquity and precession are normalized to zero mean and unit standard deviation. This forcing function, q, yields a close approximation to the pattern of insolation variations for any latitude and season, but the magnitude is arbitrary. Next, q is applied to a non-linear ice volume model with two more adjustable parameters

$$\frac{dy}{dt} = \begin{cases} \frac{1+b}{T_m}(q-y) & \text{if } q \geq y \\ \frac{1-b}{T_m}(q-y) & \text{if } q < y \end{cases} \tag{3.6}$$

Since y is negatively proportional to ice volume, $(1+b)/T_m$ scales the rate of ablation and $(1-b)/T_m$ scales the rate of accumulation. T_m is the mean time constant of the system and b is a nonlinearity coefficient, $(0 \leq b \leq 1)$. The model was tuned to *Hays* et al's [1976] orbitally-tuned RC11-120 and V28-238 cores over the period extending from the present to 150KY BP. The model parameters were estimated as $T_m = 17$KY, $b = .6$, $\alpha = -2$, and $\phi = \bar{w}\frac{\text{cycles}}{\text{KY}}2\text{KY}$ where $\bar{w}$ is the mean frequency of the precession parameter. The output of this model over the last 790KY along with the orbitally-tuned version of the benthic $\delta^{18}O$ from ODP677 is shown in Figure 3-7. The model is forced only at the obliquity (1/41KY) and precessional frequencies (1/23, 1/22, and 1/19KY), but the model's non-linearities extract the eccentricity frequencies which precession is modulated by (1/404, 1/124, and 1/95KY). Eccentricity is dominated by its 1/404KY component which reaches a minimum around stage eleven (about 450KY BP). While the model serves to enhance the 1/100KY variability, there is still a marked absence of variability around stage 11. The squared cross-correlation between *Imbrie* and *Imbrie*'s ice volume model and the ODP677 $\delta^{18}O$ benthic and planktonic records is 0.24 and 0.23 respectively. 23 age control points were used in orbitally tuning ODP677 to this model between termination one and the BM magnetic reversal.

In re-tuning *Imbrie*'s model to the $R^{(63)}$ depth-tuned version of benthic $\delta^{18}O$ ODP677, a simulated annealing [see *Press* et al, 1999] approach is used which seeks to maximize the squared cross-correlation. The search domain spans all possibilities for the four parameters, and regardless of initial values, uniformly converges on a solution which is quite different from *Imbrie and Imbrie*'s original parameterization

		Original	Revised
Precession/Obliquity ratio	α	-2	-1
Seasonality (KY)	ϕ	2	1
Mean time constant (KY)	T_m	17	.05
Non-linearity coefficient	b	.6	.999

For the insolation forcing function, the obliquity and precession components comes to share an equal portion of the variance which approximates the June insolation forcing at 90^oN and 50^oS. Alternatively, an appropriately weighted yearly average would generate an equal obliquity and precession component in the insolation forcing at any latitude between 90^oN and 50^oS. Any single insolation curve, however, is almost certainly an over-simplification. Instead, it might be better to work with the coefficients of the various spherical harmonics associated with changes in insolation forcing (this work is left for a later time, but see *Munk and Cartwright*, [1966] for an analogous tidal implementation).

The seasonality of the precession remains that of summer (ϕ = 12KY would be northern hemisphere winter), but the ice volume model is pushed into a very rapid melting parameterization. The time constant associated with melting changes from $T_m/(1+b) = 10.6KY$ to 0.025KY and for accumulation $T_m/(1-b) = 42.5KY$ goes to 50KY. In this state accumulation has a characteristic response time slower than any of the forcing frequencies which generates a relatively smooth response. Ablation happens with nearly no phase delay and is highly susceptible to large excursions in the forcing function.

The maximum squared cross-correlation achieved by adjusting the two insolation and two response time parameters is 0.28, and these results are plotted in Figure 3-7. Note 0.28 is higher than the squared cross-correlation achieved between *Imbrie*'s original estimate for the model and the $\delta^{18}O$ from ODP677 which was tuned to the model. If the adjustable ACPs in orbital tuning are considered degrees of freedom, a slightly better match is achieved here with far fewer degrees of freedom (4 as opposed to 23).

3.3.2 Simple Models of the quasi-100KY Cycle

Figure 3-8 shows the leading EOF of the $E^{(17)}$ age model (EOF-1) along with the obliquity and precession band EOFs. These latter two EOFs were constructed by

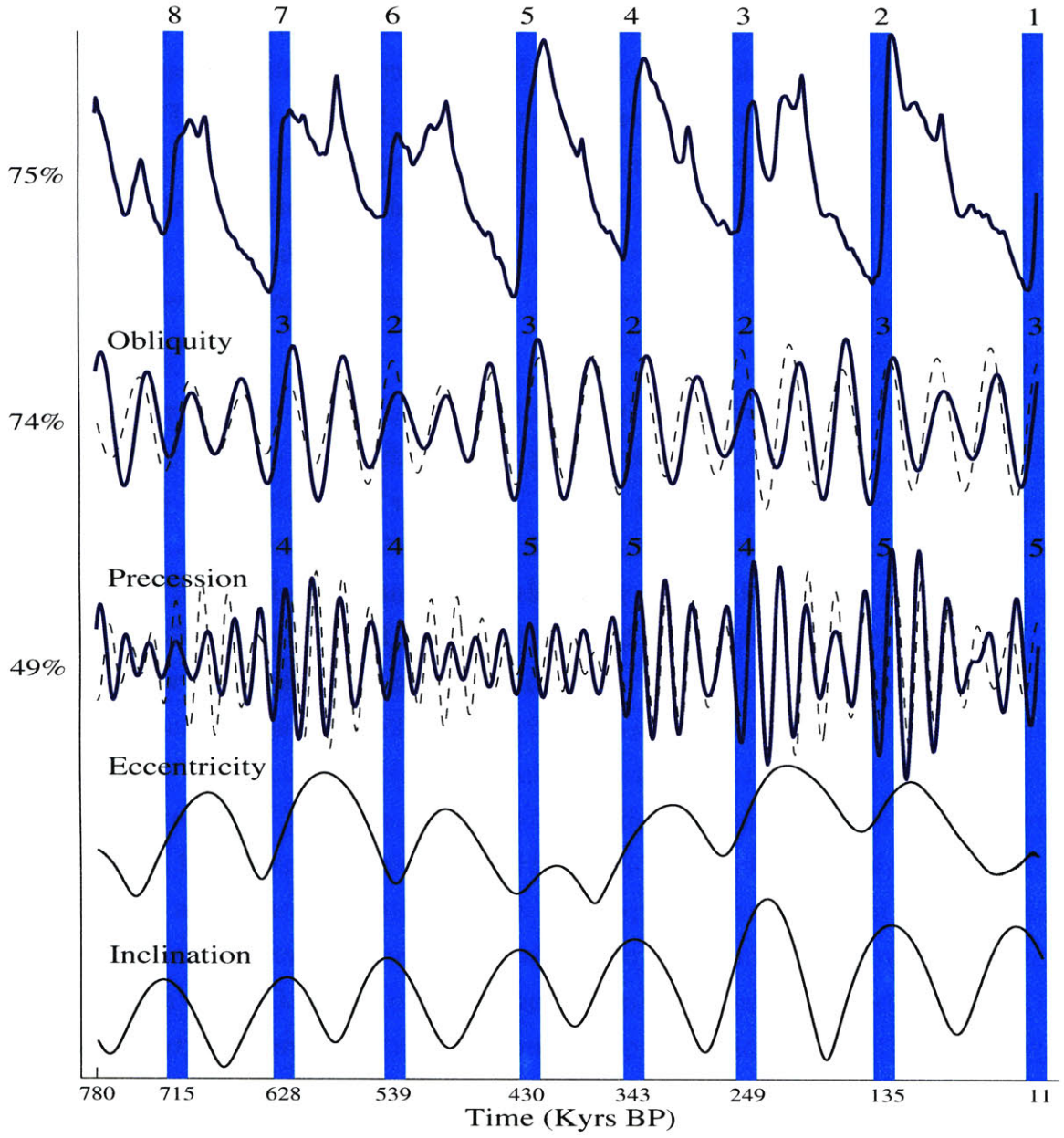

Figure 3-8: The leading EOF from the $E^{(17)}$ age model (top), pass band filtered at obliquity (middle), and pass band filtered at precession (bottom). The filtered records (solid lines) are plotted against the orbital parameters (dashed lines). The frequency modulation (FM) of obliquity, the amplitude modulation (AM) of precession, and the Inclination of the earth relative to the invariant plane are also shown. The shaded bands indicate terminations and the numbers are the cycles of precession or obliquity which have elapsed since the last termination.

first narrow pass-band filtering each $\delta^{18}O$ record and then calculating the EOF of the filtered signal. EOF-1 of the $\delta^{18}O$ records explains 75% of the total variance, the obliquity band EOF-1 explains 74%, and the precession band EOF-1 explains 49%. The filtered EOFs are plotted on top of their respective orbital parameters [*Berger* and *Loutre*, 1992]. There is a good correspondence between the EOFs and orbital parameters in both phase and amplitude, while a frequency match is assured due to the filtering process. Considering there are no orbital assumptions in the age-model, the agreement is quite strong. As already indicated in the phase plot of Figure 3-1, the $\delta^{18}O$ obliquity band lags the obliquity parameter by a few KY, while the $\delta^{18}O$ precession band shows a slight lead.

EOF-1 is clearly dominated by terminations occurring roughly every 100KY. Shaded bands indicate the corresponding ages within the obliquity, precession, eccentricity, and orbital inclination curves. A number of simple models exists which attempt to link these orbital variations with the quasi-100KY oscillation. Most models are related to the Milankovitch hypothesis that summer insolation in the N. hemisphere controls the growth of icesheets. Along these lines, *Berger* [1978] proposed a linear combination of precession (which only appears in the insolation forcing if the climatic response is seasonally sensitive, *Rubincam*, 1994), obliquity, and eccentricity (which is a weak term in insolation variations, *Imbrie* et al, 1993). A non-linear combination of precession and obliquity forcing was proposed by *Imbrie and Imbrie* [1990] as previously explained. *Paillard* [1998] introduced a quantized ice age model which transitions between three possible climate states depending on high latitude insolation thresholds. In many ways this a mathematical realizations of *Raymo*'s [1997] suggestion that glacial cycles are quantized into units of four or five precession cycles. *Rial* [1999] proposes a frequency modulated climate response to eccentricity, while *Liu* [1998] propose the 100KY cycle is due to frequency modulation in insolation as calculated by *Rubincam* [1994]. *Muller* and *MacDonald* [1997] have suggested an alternative to the Milankovitch hypothesis in which variations in the inclination of the earth's orbital plane relative to the invariant plane of the solar system drive the 100KY climatic oscillations. Non-orbital theories for the quasi-100KY cycle include internal oscillations of the climate system [e.g. *Maasch* and *Saltzman*, 1990], and quasi-periodic stochastic climate variations [e.g. *Wunsch*, 2002].

Roe and *Allen* [1999] use a regression analysis to compare these various models (not including *Liu* 1998, *Rial* 1999, or *Wunsch* 2002), and conclude there is no objec-

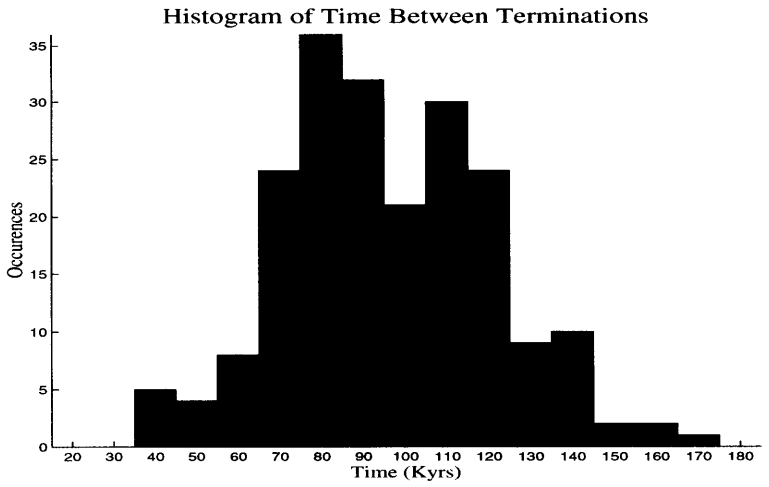

Figure 3-9: Histogram of the elapsed time between glacial cycles inferred from the $E^{(2)}$ time scale.

tive evidence in favor of any particular model. *Muller* and *MacDonald*'s arguments relying on the spectral similarity between orbital inclination and the low frequency (less than 1/95KY) $\delta^{18}O$ components are discounted on the basis of relatively short time series (about 900KY) and the non-sinusoidal nature of the glacial inter-glacial variations. A further obstacle in differentiating between these hypothesis, not mentioned by *Roe* and *Allen*, is the uncertainty in the timing of the glacial cycles. Indeed, it seems the $\delta^{18}O$ age-model used in the regression will heavily influence the results.

Each of the orbital parameters appealed to in the various orbital models above are shown in Figure 3-8 in relation to the $E^{(17)}$ EOF-1. Because the age-model of EOF-1 is unbiased towards any orbital assumptions and is accurate to within $\pm 10KY$, it offers a good basis from which to infer a relationship between low frequency $\delta^{18}O$ variations and the orbital parameters. Within the uncertainty of the age-model both precession and obliquity have a consistent phase at each termination event, while eccentricity and inclination do not. Considering the evidence of non-linear coupling between obliquity and the 1/100KY band, a constant phase relationship between $\delta^{18}O$ terminations and obliquity further indicates the possibility of a simple relationship between the two.

3.3.3 Threshold Model of Glaciation

The obliquity parameter seems to undergo a transition from a local minima to maxima during each termination event. Because the mean frequency of obliquity is roughly half that of precession, the observation that obliquity maintains a consistent phasing is more robust in the presence of age-model jitter. Figure 3-9 shows a histogram of termination repeat times for the 26 $\delta^{18}O$ records according to the $E^{(2)}$ age-model. Two repeat time clusters around 80 and 115KY are evident. Similar to *Raymo*'s suggestion that terminations occur after four or five quantized precessional cycles, it seems reasonable that glacial cycles could be quantized into two or three obliquity cycles. *Ridgwell*, *Watson*, and *Raymo* [1999] reject the notion of quantized obliquity cycles because of the substantial spectral power which emerges in side-bands, most notably the 1/70KY peak which, as discussed, is observed here to be above the 95% confidence level.

In the frequency domain a simple model should reproduce the observed spectral, coherence, and bicoherence signatures. In the time domain the variable glacial cycle duration and amplitude should be reproduced. To this end a simple ice volume model is postulated as

$$V_t' = at \qquad \textit{while } V_t \leq \theta_t \tag{3.7}$$

$$V_t' = 0$$

$$c = \int_{t_o}^{t_f} (V_t - \theta_t)dt \qquad \textit{while } V_t > \theta_t \tag{3.8}$$

$$V_t' = -cmt \qquad \textit{while } t \leq (t_f + 10) \tag{3.9}$$

This model implicitly assumes the earth's basic state over the last 800KY was to increase icevolume (V_t) at a rate a. V_t increases until a time variable obliquity threshold (θ_t) is surpassed. Once the threshold is initially crossed (t_o), ice volume remains constant until the threshold is again crossed (t_f). The time integrated amplitude of V_t's excursion above θ_t sets a collapse potential, c. Melting ensues for 10KY at a rate proportional to the collapse potential, cm. This feature of the model links the amplitude of an interglacial event to the amplitude of the preceding glacial event, a pattern which is clearly discernible in the $\delta^{18}O$ records. After melting stops an interglacial period could be specified, but this only marginally improves the results of the model, and in the interest of simplicity, accumulation is immediately re-initiated.

There are three adjustable parameters to this model which are the initial ice volume (V_o), the accumulation rate (a), and the melting rate (m). Variations in the

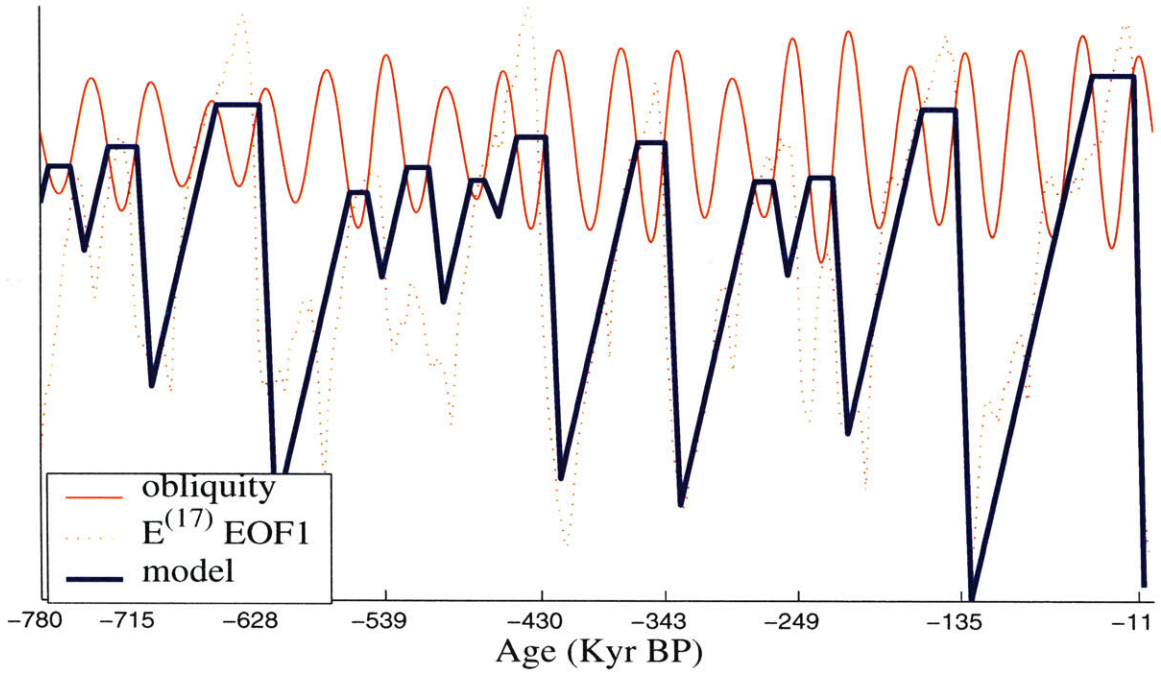

Figure 3-10: An obliquity threshold ice volume model. The plot is oriented such that both obliquity and ice volume increase upward.

mean value and amplitude of the obliquity threshold (θ_t) can equivalently be expressed as changes in V_o,a, and m. To estimate the best values for the adjustable parameters a simulated annealing method which maximizes the cross-correlation between EOF-1 and the model is used with a zero mean and unit standard deviation obliquity threshold. The model achieves a maximum squared cross-correlation of 0.62 for $V_o = -1.1$, $a = .11$, and $m = .03$ where the mean calculated collapse potential is $\bar{c} = 20$. The threshold nature of this model makes it sensitive to small changes in the parameters. Figure 3-10 shows these results plotted along with EOF-1 and the threshold function. As indicated by the high cross-correlation, there is an excellent correspondence between EOF-1 and the model in the timing and amplitude of the glacial cycles. The quasi-periodicity due to growth collapse cycles is the deterministic analog of *Wunsch*'s [2002] stochastic threshold model.

A PSD and coherence estimate of the model with T(t) from Eq 3.1 are shown in Figure 3-11. Concentration of energy into the bands centered around $f(n)$ and 1/100KY is reproduced in the same proportion as shown in Figure 3-1. While there is no 1/100KY or 1/22KY (precession) forcing, the model generates spectral peaks

at each band. The 1/100KY energy is due to a time-constant implicit to the choice of accumulation rate and threshold boundary, and the precession band energy arises as both an overtone of obliquity (2/41) and the second combination tone of obliquity and the 1/95KY variations (1/41+2/95). The coherence estimate is similar to the ensemble of $\delta^{18}O$ records in Figure 3-1 in the 1/95KY and obliquity bands. It is a notable feature of this model that while deglaciations only occur every two or three obliquity cycles and there is no direct 100KY forcing, the model is coherent with a 1/95KY harmonic above the 95% confidence level. There is no observed coherence in the precession band. Considering the high precessional coherence with the $\delta^{18}O$ record and the similarity between precession and the narrow band-passed $\delta^{18}O$ record (ref. Figure 3-8), it seems likely that there is some linear climatic response to precessional forcing. However, the major features of the $\delta^{18}O$ record, it seems, can be reproduced without including precessional forcing. The auto-bicoherence from the model also compares favorably with EOF-1. Quadratic phase coupling between the $f(0,1)$ (1/41, 1/70KY) frequencies are very strong. Strong bicoherencies also exist between frequencies couplets slightly higher than those predicted by $f(-1,-2)$. No phase coupling is observed with the 1/100KY frequency.

The fidelity with which this model reproduces the observed time dependent and spectral nature of the $\delta^{18}O$ record over the last 800KY, using only 3 adjustable parameters, indicates both the model and the $E^{(17)}$ age-model may contain some physical merit. The observed switch from a 41KY to 100KY cycle in the $\delta^{18}O$ record about 800KY ago [e.g. *Ruddiman* et al, 1986] can be simply addressed by decreasing the melting rate. That obliquity continues to be the primary driving factor, rather than giving way to precession or orbital inclination, provides a simpler framework from which to explain this switch in behavior. Further physical justification of the model might be derived by relating ice accumulation rates to latitudinal insolation gradients. It seems plausible that obliquity variations coupled with icesheet-albedo feedbacks could have a strong influence on the rate of ice volume change. The arguments in support of a significant non-linear response to obliquity forcing can be summarized as follows:

- Re-tuning *Imbrie* and *Imbrie*'s ice volume model to a non-orbitally derived $\delta^{18}O$ age-model increases the obliquity contribution and decreases the melt time-constant to a threshold like behavior.

- The elapsed time between terminations is indicative of a bi-modal system switch-

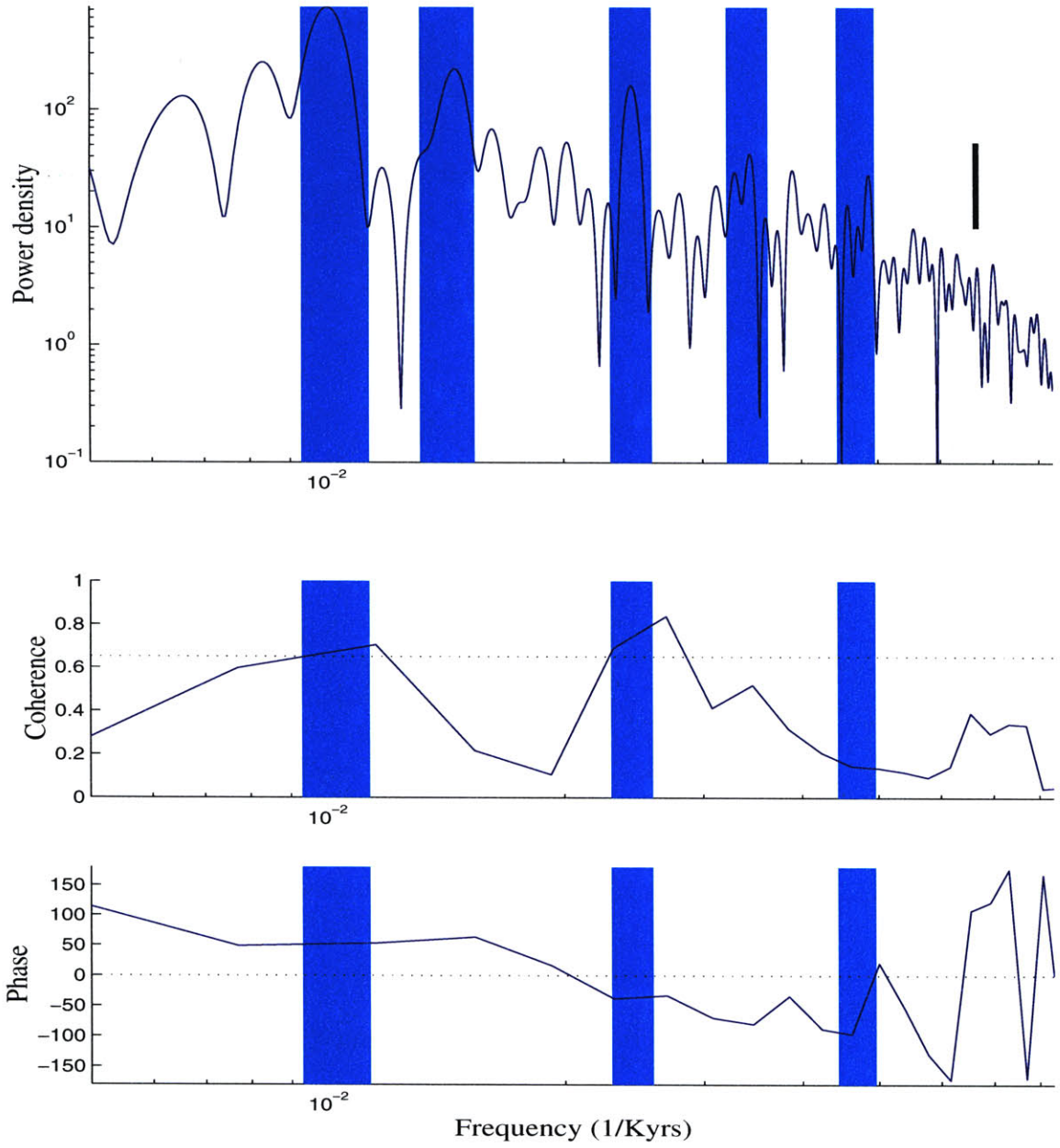

Figure 3-11: The PSD of the obliquity model (top, log log axis) with the 95% confidence interval indicated by the vertical bar. The coherence (middle, linear log) and phase (bottom, linear log) of the model realization with T(t) [ref. Eq 3.1] are also shown. Shaded bands for the PSD are 1/100KY and $f(n)$= 1/70, 1/41, 1/29, and 1/22KY.

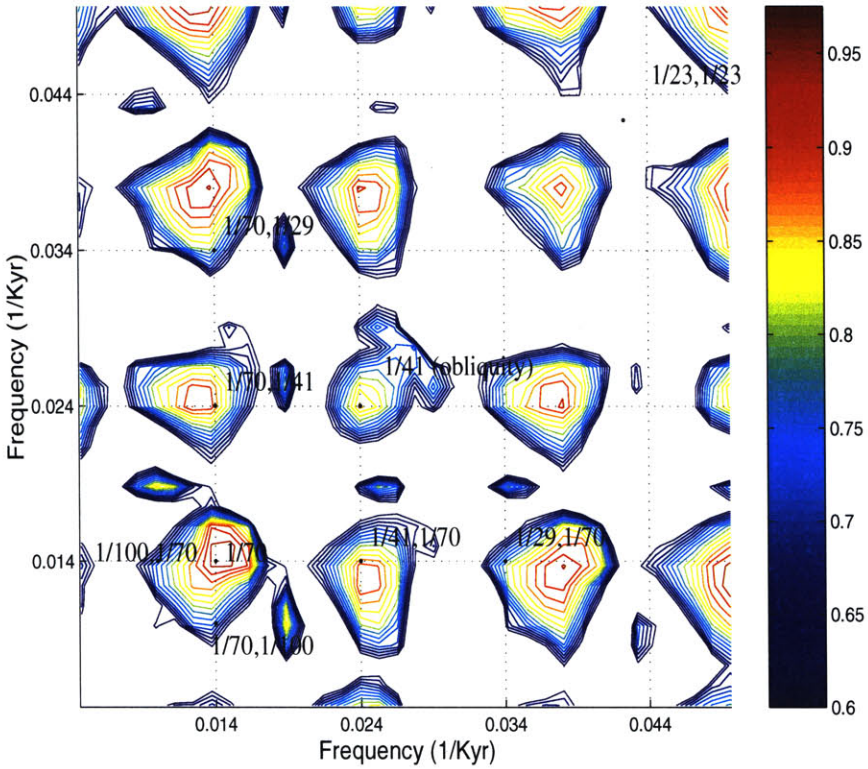

Figure 3-12: The auto-bicoherence of the obliquity threshold ice volume model. These results compare favorably with the results for EOF-1 shown in Figure 3-5

ing between roughly 80 and 120KY, or two and three obliquity cycles.

- The mean spectra of $\delta^{18}O$ has peaks at 1/100KY and

$$f(n) = f_{\text{obliquity}} + \frac{n}{100KY} \qquad n = \{-1, 0, 1, 2\}$$

which account for greater than 60% of the variance in the $\delta^{18}O$ records. For EOF-1, each of these five peaks are above the 95% confidence level with the obliquity band accounting for the largest fraction of energy (20%).

- The PSD of the temperature proxy and CO_2 records from Vostok have spectral peaks at 1/100KY and $f(n)$ for $n = \{-1, 0, 1, 2, 3\}$ which also account for greater than 60% of the total variance.

- There is a strong auto-bicoherence pattern coincident with the spectral peaks given by f(n) and at 1/100KY. This indicates a non-linear phase coupling between obliquity and the majority of the variance in the $\delta^{18}O$ record.

- A simple obliquity based threshold model with three degrees of freedom attains a squared cross-correlation of 0.63 with EOF-1, has a similar coherence relationship with the orbital parameters, and reproduces spectral peaks and bicoherencies at f(n).

Conclusion

The age-model assigned to paleo-climatic records strongly influences the inferences drawn about past climatic behavior. Variations in the rate of sediment accumulation causes jitter in linear age-depth models, so that a simple linear age-depth relationship is often not sufficiently accurate to yield meaningful results. The currently favored method to correct for jitter is orbital-tuning, but it is shown that the accuracy of orbitally-tuned age-models cannot be verified, and Monte Carlo simulations of orbital-tuning indicate little skill in improving the age-models of $\delta^{18}O$ like records. In particular, and contrary to a number of assertions, orbital tuning is shown to build-in eccentricity like amplitude modulation in the precession band independent of the age-model accuracy. Also, and perhaps most importantly, the orbital-tuning process tends to preclude the manifestation of non-Milankovitch behavior.

An alternative to orbital-tuning is *depth-tuning* which estimates age using mean sediment accumulation rates. In this study an unprecedented 26 isotopic records are correlated together, each of which extends through the B-M reversal. Two forms of depth-tuning are implemented: (1) visually identifying and matching together isotopic event and (2) using XCM to maximize the cross-correlation between $\delta^{18}O$ records. The methods yield age-models within two KY of one another, and after correcting for the effects of sediment compaction, depth-tuned isotopic events are on average nine KY older than their orbitally-tuned counter-parts (the terminations are on average eight KY older). A stochastic model of sediment accumulation variability is developed and indicates the depth-tuned age-models have an average expected uncertainty of 8.5KY for any given event, and that a two standard deviation discrepancy exists between the orbital and depth-tuned age-models. Independent radiometric constraints on the age of terminations, particularly termination two, support depth-tuned over orbitally-tuned age estimates.

The depth-tuned age-models developed in chapter two are devoid of any orbital assumptions, are based upon at least twice as many age-depth relationships as any previous study and, unlike any previous linear age-depth model, are corrected for the effects of compaction; and thus offer a unique vantage point from which to evaluate the orbital theory of climate change. Spectral analysis of the $\delta^{18}O$ record (using the $E^{(17)}$ age-model) indicates significant spectral peaks at the 1/100 KY under and

overtones of the obliquity band,

$$f(n) = f_{\text{obliquity}} + n/100 \quad n = \{-1, 0, 1, 2\}$$

A similar arrangement of spectral peaks is observed in the temperature proxy and CO_2 records from Vostok. Furthermore there is a significant auto-bicoherence between each $f(n)$ frequency all of which strongly indicates a non-linear climatic response to obliquity forcing which is coupled to the quasi-1/100KY oscillation.

Re-tuning *Imbrie and Imbrie*'s [1980] ice-volume model using the depth-tuned age-model indicates the existence of a stronger response to obliquity variations and a much more rapid glacial melt response than originally estimated. A simple obliquity based threshold model of glaciation is developed and shown to reproduce the observed timing, amplitude, rapid melt response, and non-linear features of the $\delta^{18}O$ record. The ability of this model to reproduce the character of the glacial records indicates the physical plausibility of both the depth-tuned age-model and the inference of a non-linear climatic response to obliquity forcing.

This thesis lays the groundwork for further research in at least four different directions. First, more $\delta^{18}O$ records, given they become available, could be incorporated into the depth-tuning process. Second, the depth-tuned chronology was only applied to the $\delta^{18}O$ records from each core site, but a wealth of further information is available within each core. In particular, a $\delta^{13}C$ record is available for virtually every $\delta^{18}O$ record discussed here. Analysis of these complimentary records might be used to estimate the spatial and temporal relationships of multiple components of the climate system in a manner similar to *Imbrie* et al [1993]. Third, both the depth-tuned and Devils Hole chronologies were used in estimating temporal and spatial sediment accumulation rate variability. Incorporating information concerning the sediment composition would help distinguish between variation in terrigenous discharge and variations in oceanic productivity. Both terrigenous discharge and oceanic productivity proxy variations could be useful in constraining global climate change patterns. Finally, the apparent non-linear response to obliquity forcing motivated the development of a simple climate model. It seems, however, that numerous models based on a wide range of assumptions can reproduce significant elements of the observed climatic record. A comparison of the assumptions and explanatory ability of these various simple models, with attention to generalizing the behavior of each model, could lead to a better understanding of long term climate change.

Appendix A

The XCM Tuning Algorithm

The XCM routine adjusts the timescale of a record, $\psi(t')$, in relation to a target record, $\tau(t)$, to maximize the squared cross-correlation coefficient

$$r^2 = \left(\frac{\sum_t \eta(t' + h(t'))\tau(t)}{\sqrt{\sum_t \eta(t' + \mu(t'))^2}\sqrt{\sum_t \tau(t)^2}} \right)^2$$

where $\mu(t')$ is the time adjustment function. Because time is stretched and squeezed for $\eta(t')$ according to $\mu(t')$, its average value will change. In this algorithm,$\tau\,(t')$ and $\eta(t')$ are discretely sampled at 1-KY intervals and ACPs are assigned to $\eta(t')$ at 5KY intervals. The ACPs are allowed to slide backward and forward in time and the ages between ACPs are linearly interpolated. To prevent unrealistic changes in the implied accumulation rates, the space between neighboring ACPs is restricted to lie between one and 25KY (a maximum stretching or squeezing factor of 5). A simulated annealing optimization method [*Press* et al, 1999] is applied to estimate the arrangement of ACPs which maximizes the cross-correlation. This control-point arrangement provides a piecewise linear approximation to $\mu(t')$. At the end of the optimization, the squared cross-correlation typically increases from near zero to about 0.25.

Most tuning algorithms employ narrow pass-band filtering to isolate the Milankovitch band of interest. A difficulty with this approach is that even slight errors in the the preliminary age-model can smear spectral energy across the entire frequency range. As an example, Figure A-1 shows a signal, $\psi(t)$, composed of equal parts obliquity and precession terms whose age-model is subjected to a mild jittering ($J = 0.1$) resulting in $\psi(t')$. The jitter is applied according to estimates later made for the $\delta^{18}O$ record. In the time domain, $\psi(t)$ and$\psi(t')$ appear similar, but the spectrum

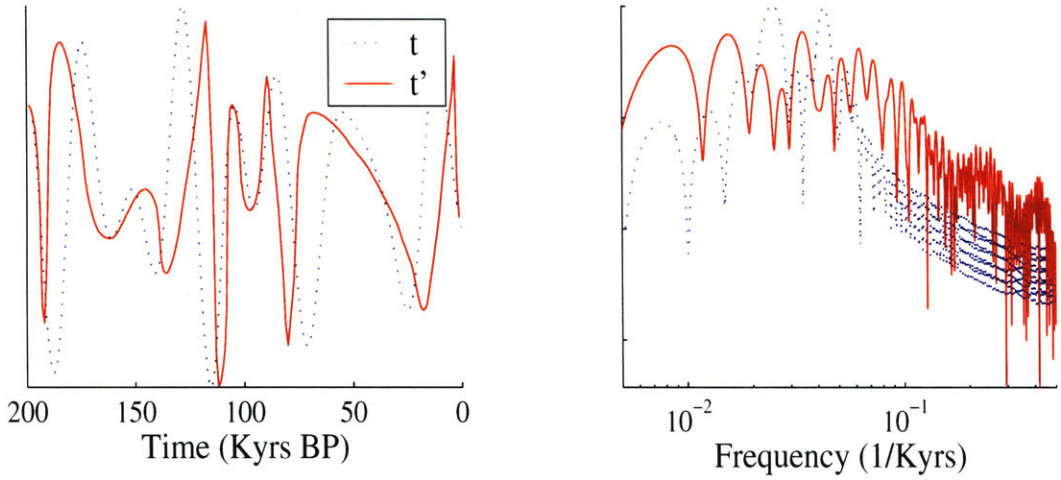

Figure A-1: A signal composed equally of obliquity and precession shown with a true age, t, and jittered age-model, t'. The time series is shown on the left and the PSD on the right. Note how t' smears energy across all frequencies.

of $\psi(t')$ shows a red noise process devoid of spectral peaks. The mistiming results in a form of aliasing of the spectral power, and like all aliasing, no filter can undo it. Note the energy is dispersed across the entire spectrum. A narrow pass-band filter will inevitably exclude significant portions of $\psi(t)$ and thus no pass band filtering is employed in this tuning algorithm. A broadband tuning strategy may undo the effects of jitter, but narrow-band tuning will not.

Appendix B

Auto-bicoherence

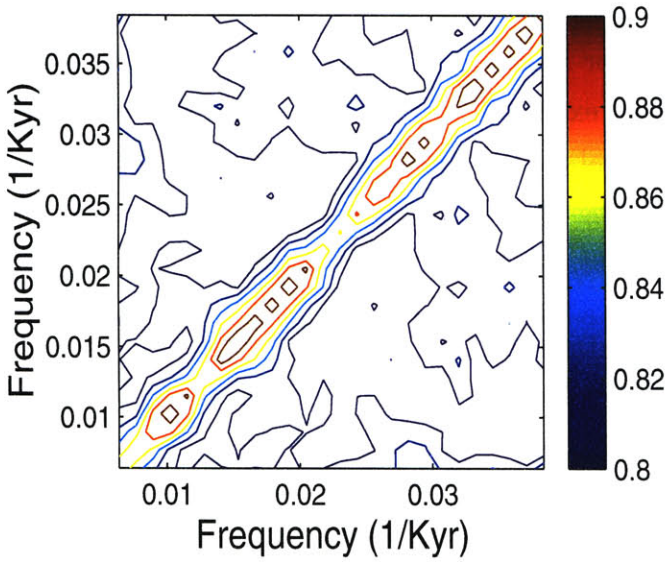

Figure B-1: The 95th percentile level of auto-bicoherence for red noise. Values are .8 for $k \neq l$ and .9 for $k = l$.

A test for quadratic coupling was presented by *Hasselmann* et al [1963] and used to evaluate non-linearities in shallow wave propagation. Essentially when two harmonics are coupled so as to modulated one another a third harmonic with a particular frequency and phase is expected

$$S(t) = e^{2\pi i f_k t + \phi_k} e^{2\pi i f_l t + \phi_l} = e^{2\pi i (f_k + f_l) t + \phi_k + \phi_l}$$

To test for this relationship define the bispectrum as

$$B_{k,l} =< \hat{S}_k \hat{S}_l \hat{S}^*_{k+l} >$$

where $\hat{S}_k$ is the discrete Fourier transform of S(t) at frequency interval k, S^* is the conjugate ($S^*_{k+l} = S_{-k-l}$), and <> indicates the expected value. Unless $\phi_{k+l} = -(\phi_k + \phi_l)$, B(k,l) will be complex. The magnitude of B(k,l) depends on both the magnitude of the complex Fourier coefficients, $|\hat{S}_k||\hat{S}_l||\hat{S}_{k+l}|$, and the coherence of the phase relationship between the coefficients; i.e. for random phasing $< \hat{S}_k \hat{S}_l \hat{S}_{k+l} >= 0$. The bispectrum mixes measures of both phase coherence and magnitude between the triplets of frequencies. To measure the phase coherence alone, define the auto-bicoherence as

$$C_{k,l} = \frac{< \hat{S}_k \hat{S}_l \hat{S}_{k+l} >}{< |\hat{S}_k||\hat{S}_l||\hat{S}_{k+l}| >}$$

where the denominator represents B(k,l) in the case of perfect phase coherence, and $0 \leq C_{k,l} \leq 1$. The expected value of the auto-bicoherence is estimated here by adapting the bispectral routine presented by *Muller* and *MacDonald* [p.293, 2000]. The algorithm consists of subtracting the mean value of S(t), applying a Hanning window, and estimating the auto-bicoherence as

$$C_{k,l} = \frac{|\sum_{k-2}^{k+2} \sum_{l-2}^{l+2} a_{k,l} \hat{S}_k \hat{S}_l \hat{S}_{k+l}|}{\sum_{k-2}^{k+2} \sum_{l-2}^{l+2} a_{k,l} |\hat{S}_k||\hat{S}_l||\hat{S}_{k+l}|}$$

$$a_{k+n,l+m} = \frac{1}{\sqrt{(k-n)^2 + (l-m)^2}} \qquad n, m = -2, -1, 1, 2$$

$$a_{k,l} = 1$$

where $a_{k,l}$ is a weighting coefficient. The results are contour plotted on a frequency vs. frequency axis which is symmetric about the diagonal. Figure B-1 shows the 95th percentile result for 1000 iterations of the auto-bicoherence algorithm run with red noise (ref. Eq 2.2). This Monte Carlo simulation indicates the 95% confidence level to reject the null hypothesis of red noise is 0.8 for $k \neq l$ and 0.9 for $k = l$.

Bibliography

[1] L.F. Athy. Density, porosity and compaction of sedimentary rocks. *AAPG Bull.*, 14:1–24, 1930.

[2] E. Bard, Hamelin B., and R.G. Fairbanks. U-th ages obtained by mass spectrometry in corals from barbados: sea level during the past 130,000 years. *Nature*, 346:241–244, 1990.

[3] F.C. Bassinot, E. Beaufort, L. Vincent, F. Labeyrie, P.J. Rostek, Muller, Quidelleur X., and Y. Lancelot. Coarse fraction fluctuations in pelagic carbonate sediments from the tropical indian ocean: A 1500-kyr record of carbonate dissolution. *Paleocoeanography*, 9:579–599, 1994.

[4] A. Berger. Long-term variations of daily insolation and quaternary climatic changes. *Journal of Atmospheric Sciences*, 35:2362–2367, 1978.

[5] A. Berger and M. F. Loutre. Astronomical solutions for paleoclimate studies over the last 3 million years. *Earth Planet. Sci. Lett.*, 111:369–382, 1992.

[6] A. L. Berger. Astronomical theory of paleoclimates and the last glacial-interglacial cycle. *Quat. Sci. Rev.*, 11:571–581, 1992.

[7] W.H. Berger and E. Jansen. Mid-pleistocene climate shift - the nansen connection. In O.M. Johannessen, R.D. Muench, and J.E. Overland, editors, *The Polar Oceans and Their Role in Shaping the Global Environment*, volume 85, pages 295–311, 1996.

[8] R. N. Bhattacharya and Waymire E. C. *Stochastic Processes with Applications.* John Wiley & Sons, 1990.

[9] T. Bickert, W.B. Curry, and G. Wefer. Late pliocene to holocene (2.6-0 ma) western equatorial atlantic deep water circulation: Inferences from benthic stable

isotopes. In N.J. Shackleton et al, editor, *Proceedings of the Ocean Drilling Program Scietific Results*, volume 154, 1997.

[10] A.L. Bloom. Quaternary sea level fluctuations on a tectonic coast: new dates from the huon peninsula, new guinea. *Quaternary Research*, 4:185–205, 1974.

[11] E.W. Bolton and K.A. Maasch. A wavelet analysis of plio-pleistocene climate indicators: N new view of periodicity evolution. *Geophysical Rsearch Letters*, 22:2753–2756, 1995.

[12] R. Bracewell. *The Fourier Transform and its Applications.* McGraw Hill, 2000.

[13] W. Broecker, D.L. Thurber, J. Goddard, T.L. Ku, R.K. Matthews, and K.J. Mesolella. Milankovitch hypothesis supported by precise dating of coral reefs and deep-sea sediments. *Science*, 159:297–300, 1968.

[14] W.S. Broecker. Terminations. In Berget et al, editor, *Milankovitch and Climate, Part2*, pages 687–698. D. Reidel, 1984.

[15] W. Bruggerman. A minimal cost function method for optimizing the age-depth relationship of deep-sea sediment cores. *Paleoceanography*, 7:467–487, 1992.

[16] J.E.T. Channell, D.A. Hodell, and B. Lehman. Relative geomagnetic paleointensity and $\delta^{18}o$ at odp site 983. *Earth and Planetary Science Letters*, 153:103–118, 1997.

[17] J. Chappell. Geology of coral terraces, huon peninsula, new guinea: a study of quaternary tectonic movements and sea-level changes. *Geological Society of America Bulletin*, 85:553–570, 1974.

[18] J. Chen, J. Farrell, D. Murray, and W Prell. Timescale and paleoceanographic implications of a 3.6 m.y. oxygen isotope record from the northeast indian ocean (odp site 758). *Paleoceanography*, pages 21–47, 1995.

[19] J.L. Cullen and W.B. Curry. Variations in planktonic foraminifer faunas and carbonate preservation at site 927: evidence for changing surface water conditions in the western tropical atlantic ocean during the middle pleistocene. In N.J. Shackleton, W.B. Curry, C. Richter, and T.J. Bralower, editors, *Proceedings of the Ocean Drilling Program Scietific Results*, volume 154, pages 207–228, 1997.

[20] W.B. Curry, N.J. Shackleton, and C. Richter. *Proceedings of the Ocean Drilling Program, Initial Reports*, volume 154. Ocean Drilling Program, College Station TX, 1995.

[21] J.M.A Danby. *Fundamentals of Celestial Mechanics.* Willmann-Bell, 1992.

[22] R.E. Dodge, R.G. Fairbanks, L.K. Benniger, and F. Maurrasse. Pleistocene sea levels from raised coral reefs of haiti. *Science*, 219:1423–1425, 1983.

[23] R.L. Edwards, J.H. Chen, and J.G. Wasserburg. Precise timing of the last interglacial period from mass spectrometric determination fo thorium-230 in corals. *Science*, 236:1547–1553, 1987.

[24] M. Elkibbi and J.A. Rial. An outsider's review of the astronomical theory of the climate: is the eccentricity-driven insolation the main driver of the ice ages? *Earth-Science Reviews*, 56:161–177, 2001.

[25] M.T. Esat, M.T. McCulloch, J. Chappell, B. Pillans, and A. Omura. Rapid fluctuations in sea level recorded at huon peninsula during the penultimate deglaciation. *Science*, 283:197–202, 1999.

[26] W. Feller. *An introduction to probability theory and its applications.* Wiley mathematical statistics series, 1966.

[27] B.P. Flower. Planktonic foraminifers from the subpolar north atlantic and nordic seas: Sites 980-987 and 907. In M.E. Raymo, E. Jansen, P. Blum, and T.D. Herbert, editors, *Proceedings of the ocean Drilling Program*, pages 19–34, 1999.

[28] J. Galewsky, E.A. Silver, C.D. Gallup, R.L. Edwards, and D.C. Potts. Foredeep tecctonics and carbonate platform dynamics in the huon gulf, papua new guinea. *Geology*, 24:819–822, 1996.

[29] Christina D. Gallup, H. Cheng, F. W. Taylor, and R. L. Edwards. Direct determination of the timing of sea level change during termination ii. *Science*, 295:310–314, 2002.

[30] K. Hasselmann, W. Munk, and G. MacDonald. Bispectra of ocean waves. In Rosenblatt, editor, *Proc. Symposium on Time Series Analysis*, pages 125–139. J. Wiley, 1963.

[31] J.D. Hays, J. Imbrie, and N.J. Shackleton. Variations in the earth's orbit: Pacemaker of the ice ages. *Science*, 194:1121–1132, 1976.

[32] G. Henderson and N. SLowey. Evidence from u-th dating against northern hemisphere forcing of the penultimate deglaciation. *Nature*, 404:61–66, 2000.

[33] T.D. Herbert, J.D. Schuffert, D. Andreasen, L. Heusser, M. Lyle, A. Mix, A.C. Ravelo, L.D. Stott, and J.C. Herguera. Collapse of the california current during glacial maximum linked to climate change on land. *Science*, 293:71–76, 2001.

[34] J. Imbrie, A. Berger, E. A. Boyle, S. C. Clemens, A. Duffy, W. R. Howard, G. Kukla, J. Kutzbach, D. G. Martinson, A. McIntyre, A. C. Mix, B. Molfino, J. J. Morley, L. C. Peterson, N. G. Pisias, W. L. Prell, M. E. Raymo, N. J. Shackleton, and J. R. Toggweiler. On the structure and origin of major glaciation cycles .2. the 100,000-year cycle. *Paleoceanography*, 8:699–735, 1993.

[35] J. Imbrie, J.D. Hays, D.G. Martinson, A. McIntyre, A.C. Mix, J.J. Morley, N.G. Pisias, W.L. Prell, and N.J. Shackleton. The orbital theory of pleistocene climate: Support from a revised chronology of the marine delta 18 o record. In A.L. Berger et al., editor, *Milankovitch and Climate, Part 1*, pages 269–305. D. Reidel Publishing Company, 1984.

[36] J. Imbrie, A. C. Mix, and D. G. Martinson. Milankovitch theory viewed from devils hole. *Nature*, 363:531–533, 1993.

[37] John Imbrie and John Z. Imbrie. Modeling the climatic response to orbital variations. *Science*, 207:943–953, 1980.

[38] D.B. Karner and F. Marra. Correlation of fluviodeltaic aggradational sections with glacial climate history: a revision of the plesitocene stratigraphy of rome. *Geological Society of America Bulletin*, 110:748–758, 1999.

[39] D.V. Kent. Orbital tuning of geomagnetic polarity time-scales. *Philosphical Transactions of the Royal SOciety of London Series A*, 357:1995–2007, 1999.

[40] R.S. Lindzen and K. Emanuel. The greenhouse effect. *Manuscript*, 1999.

[41] H.S. Liu. Phase modulation effect of the runbincam insolation variations. *Theor. Appl. Climatol.*, 61:217–229, 1998.

[42] H.S. Liu. Wavelet spectral analysis of the earth's orbital variations and paleoclimatic cycles. *Journal of Atmsopheric Science*, 55:227–236, 1998.

[43] K. Maasch and B. Saltzman. A low-order dynamical model of global climatic variability over the full pleistocene. *J. Geophysical Research*, 95:1955–1963, 1990.

[44] D. G. Martinson, W. Menke, and A. Stoffa. An inverse approach to signal correlation. *Journal of Geophysical Research*, 87:4807–4818, 1982.

[45] M. Milankovitch. *Kanon der Erdbestrahlung und seine Andwendung auf das Eiszeitenproblem.* Royal Serbian Academy, 1941.

[46] A.C. Mix, J. Le, and Shackleton N.J. Benthic foraminifer stable isotope stratigraphy of site 846: 0-1.8 ma. In G. Pisias, N, T.R. Mayer L.A.and Janecek, A. Palmer-Julson, and T.H. van Adel, editors, *Proceedings of the Ocean Drilling Program Scietific Results*, volume 138, pages 839–854, 1995b.

[47] A.C. Mix, N.G. Pisias, W. Rugh, J. Wilson, A. Morey, and T.K. Hagelberg. Benthic foraminifer stable isotope record from site 849 (0-5ma): Local and global climate changes. In G. Pisias, N, T.R. Mayer L.A.and Janecek, A. Palmer-Julson, and T.H. van Adel, editors, *Proceedings of the Ocean Drilling Program Scietific Results*, volume 138, pages 371–412, 1995a.

[48] M. I. Moore and P. J. Thomson. Impact of jittered sampling on conventional spectral estimates. *J. Geophys. Res.-Oceans*, 96:18519–18526, 1991.

[49] R. A. Muller and G. J. MacDonald. Glacial cycles and astronomical forcing. *Science*, 227:215–218, 1997.

[50] C. Munk and D. Cartwright. Tidal spectroscopy and prediction. *Philisophical Transactions of the Royal Society*, 259:534–581, 1966.

[51] B. Neeman. Orbital tuning of paleoclimate records: A reassessment. *Lawrence Berkelely Laboratory Report*, LBNL-39572, 1993.

[52] D.C. Nobes, S.F. Bloomer, J. Mienert, and F. Westall. Milankovitch cycles and nonlinear response in the quaternary record in the atlantic sector of the southern oceans. *Proceedings of the ODP, Scientific Results*, 114, 1991.

[53] Frank W. Olver. *Tables for Bessel functions of moderate or larger orders.* London, H. M. Sationary Off., 1962.

[54] D. Paillard. The timing of pleistocene glaciations from a simple multiple-state climate model. *Nature*, 391:378–391, 1998.

[55] P. Pestiaux and A. Berger. Impacts of deep-sea processes on paleoclimatic spectra. In A.L. Berger et al., editor, *Milankovitch and Climate, Part 1*, pages 493–510. D. Reidel Publishing Company, 1984.

[56] J.R. Petit, J. Jouzel, D. Raynaud, N. Barkov, Banola J., I. Basile, M. Bender, J. Chappellaz, M. Davis, G. Delaygue, M. Delmotte, M. Kotlyakov, M. Legrand, V. Lipenkov, C. Lorius, L. Pepin, C. Ritz, E. Saltzman, and M. Stivenard. Climate and atmospheric history of the past 420,000 years from the vostok ice core, antarctica. *Nature*, 399:429–436, 1999.

[57] N. G. Pisias, D. G. Martinson, T.C. Moore, N. J. Shackleton, W. Prell, J. Hays, and G. Boden. High resolution stratigraphic correlation of benthic oxygen isotopic records spanning the last 300,000 years. *Marine Geology*, 56:119–136, 1984.

[58] W. Prell. Oxygen and carbon isotope stratigraphy for the quaternary of hole 502b: evidence for two modes of isotopic variability. *DSDP initial reports*, 68:455–464, 1982.

[59] W.L. Prell, J. Imbire, D.G. Martinson, J.J. Morley, N.G. Pisias, N.J. Shackleton, and H. Streeter. Graphic correlation of oxygen isotope records: application to the late quaternary. *Paleoceanography*, 1:137–162, 1986.

[60] A.C. Ravelo and Shackleton N.J. Evidence for surface water circulation changes at site 851 in the eastern tropical pacific ocean. In N.G. Pisias, L.A. Mayer, T.R. Janecek, A. Palmer-Julson, and T.H. van Andel, editors, *Proceedings of the ocean Drilling Program*, pages 503–516, 1995.

[61] M. E. Raymo. The timing of major climate terminations. *Paleoceanography*, 12:577–585, 1997.

[62] J.A. Rial. Pacemaking the ice ages by frequency modulation of earth's orbital eccentricity. *Science*, 285:564–568, 1999.

[63] A. J. Ridgwell, A. J. Watson, and M. E. Raymo. Is the spectral signature of the 100 kyr glacial cycle consistent with a milankovitch origin? *Paleoceanography*, 14:437–440, 1999.

[64] G. Roe and M. Allen. A comparison of competing explanations for the 100,000-yr ice age cycle. *Geophysical Research Letters*, 26:2259–2262, 1989.

[65] D.P. Rubincam. Insolation in terms of earth's orbital parameters. *Theoretical Applied Climatology*, 53:257–259, 1994.

[66] W. F. Ruddiman, M. Raymo, and A. McIntyre. Matuyama 41,000-year cycles - north-atlantic ocean and northern-hemisphere ice sheets. *Earth Planet. Sci. Lett.*, 80:117–129, 1986.

[67] W. F. Ruddiman, M.E. Raymo, D.G. Martinson, B.M Clement, and J. Backman. Pleistocene evolution: Northern hemisphere ice sheets and north atlantic ocean. *Paleoceanography*, 4:353–412, 1989.

[68] D.P. Schrag, G. Hampt, and Murray D.W. Pore fluid constraints on the temperature and oxygen isotopic composition of the glacial ocean. *Science*, 272:1930–1932, 1996.

[69] N. J. Shackelton, T. K. Hagelberg, and S. J. Crowhurst. Evaluating the success of astronomical tuning: Pitfalls of using coherence as a criterion for assessing pre-pleistocene timescales. *Paleoceanography*, 10:693–697, 1995.

[70] N. J. Shackelton and M. Hall. Oxygen and carbon isotope stratigraphy of deep-sea drilling project hole 552a: Plio-pleistocene glacial histoy. *DSDP Initial Reports*, 81:599–609, 1984.

[71] N. J. Shackleton, A. Berger, and W. R. Peltier. An alternative astronomical calibration of the lower pleistocene timescale based on odp site 677. *Trans. R. Soc. Edinb.-Earth Sci.*, 81:251–261, 1990.

[72] N. J. Shackleton and J. Imbrie. The $\delta^{18}o$ spectrum of oceanic deep water over a five-decade band. *Climatic Change*, 16:217–230, 1990.

[73] N. J. Shackleton and N. D. Opdyke. Oxygen isotope and palaeomagnetic stratigraphy of equatoria pacific core v28-238: Oxygen isotope temperature and ice volumes on a 10^5 and 10^6 year scale. *Quaternary Research*, 3:39–55, 1972.

[74] N. J. Shackleton and N. D. Opdyke. Oxygen-isotope and paleomagnetic stratigraphy of pacific core v28-239: Late pliocene to latest pleistocene. *Mem Geol. Soc, Am.*, 145:449–464, 1976.

[75] A. Shaw. *Time in Stratigraphy.* McGraw-Hill, 1964.

[76] C.H. Stirling, T.M. Esat, K. Lambeck, and McCulloch M.T. Timing and duration of the last interglacial: evidence for a restricted interval of widespread coral growth. *Earth and Planetary Science Letters*, 160:745–762, 1998.

[77] C.H. Stirling, T.M. Esat, K. Lambeck, McCulloch M.T., Blake S.G., D.C. Lee, and Halliday A.N. Orbital forcing of the marine isotope stage 9 interglacial. *Science*, 291:290–294, 2001.

[78] L. Tauxe, T. Herbert, and N.J. Shackleton. Astronomical calibration of the matuyama brunhes boundary: consequences for magnetic remanence acquisition in marine carbonates and the asian loess sequences. *Earth Planet. Sci. Lett.*, 140:133–146, 1996.

[79] H.R. Thierstein, K.R. Geitzenauer, B. Molfino, and N.J. Shackleton. *Geology*, 5:400–414, 1977.

[80] P. J. Thomson and P. M. Robinson. Estimation of second-order properties from jittered time series. *Ann. Inst. Stat. Math.*, 48:29–48, 1996.

[81] R. Tiedemann, M. Sarnthein, and N. J. Sahckleton. Astronomic timescale for the pliocene atlantic $\delta^{18}o$ and dust flux records of odp site 659. *Paleoceanography*, 9:619–638, 1994.

[82] K.A. Venz, D.A. Hodell, C. Stanton, and D.A. Warnke. A 1.0 myr record of glacial north atlantic intermediate water variability from odp site 982 in the northeast atlantic. *Paleoceanography*, 14:42–52, 1999.

[83] I. Winograd, T. Coplen, J. Landwehr, A. Riggs, K. Ludwig, B. Szabo, P. Kolesar, and K. Revesz. Continuous 500,000-year climate record from vein calcite in devils hole, nevada. *Scince*, 258:255–260, 1992.

[84] C. Wunsch. On sharp spectral lines in the climate record and the millennial peak. *Paleoceanography*, 15:417–424, 2000.

[85] C. Wunsch. The spectral description of climate change including the 100ky energy. *in press*, 2002.

[86] K.-H. Wyroll. An outline of late cenozic palaeoclimatic events in the cape range region. In *Palaeoclimate of Cape Range*, volume 45, pages 39–50. Rec. West. Aust. Mus., 1993.

[87] P. Yiou, C. Genthom, M. Ghil, J. Jouzel, J.M. Barnola, C. Lorius, and Y.N. Korotkevitch. High-frequency paleovariability in climate and co_2 levels from vostok ice core records. *Journal of Geophysical Research*, 96:20,365–20,378, 1991.

[88] Z.R. Zhu, K.-H. Wyrwoll, L.B. Collins, J.H. Chen, G.J. Wasserburg, and Eisenhauer A. High-precision u-series dating of last interglacial events by mass spectrometry: Houtman abrolhos islands, western australia. *Earth and Planetary Science Letters*, 118:281–293, 1993.